
Electronic Thesis and Dissertation Repository

6-23-2015 12:00 AM

Strength Study of Zircon Under High Pressure

Ievgeniia Morozova, *The University of Western Ontario*

Supervisor: Dr. Sean R. Shieh, *The University of Western Ontario*

A thesis submitted in partial fulfillment of the requirements for the Master of Science degree in
Geophysics

© Ievgeniia Morozova 2015

Follow this and additional works at: <https://ir.lib.uwo.ca/etd>



Part of the [Geology Commons](#), [Geophysics and Seismology Commons](#), and the [Mineral Physics Commons](#)

Recommended Citation

Morozova, Ievgeniia, "Strength Study of Zircon Under High Pressure" (2015). *Electronic Thesis and Dissertation Repository*. 2907.
<https://ir.lib.uwo.ca/etd/2907>

This Dissertation/Thesis is brought to you for free and open access by Scholarship@Western. It has been accepted for inclusion in Electronic Thesis and Dissertation Repository by an authorized administrator of Scholarship@Western. For more information, please contact wlsadmin@uwo.ca.

Strength Study of Zircon Under High Pressure

(Thesis format: Monograph)

by

Ievgeniia Morozova

Department of Earth Sciences

Graduate Program in Geophysics

A thesis submitted in partial fulfillment
of the requirements for the degree of
Master of Science

The School of Graduate and Postdoctoral Studies
The University of Western Ontario
London, Ontario, Canada

©Ievgeniia Morozova 2015

ABSTRACT

Zircon (ZrSiO_4) is a strong accessory mineral that can retain U, Th and Hf within its structure. This makes zircon an important material in geochemical and geochronological studies. In addition, the strong thermal shock resistance of zircon allows for dating the formations of melt and impact events and to separate shocked and potentially shocked country rocks. However, the deformation mechanism and microstructure behavior of zircon at high pressure is poorly understood. Therefore, this work aims to study the deformation and texture of zircon in situ at high pressure and room temperature, and also to examine the microstructure of samples recovered from high pressure.

Angle-dispersive X-ray diffraction in a radial geometry using a diamond-anvil cell was performed at beamline X17C, National Synchrotron Light Source (NSLS). Volume data fitted to Birch-Murnaghan equation of state yielded a bulk modulus of 203 ± 13 GPa ($K_0=4$) at hydrostatic conditions, and also shown zircon is a strong but stress sensitive mineral. The differential stress supported by zircon is in the range of 2.5 – 5.5 GPa in this study. Differential stress supported by (200) plane exhibited as the weakest and deformed plastically above 18 GPa. Weak texture in (001) was observed at low pressure and rotated towards to (110) due to the applied stress. Twins with 65° misorientation were observed within the stability field of zircon in recovered sample. Both ‘parent’ and twined zones had residual strain up to 25° .

Keywords: zircon; diamond-anvil cell; X-ray diffraction; synchrotron radiation; differential stress.

ACKNOWLEDGEMENTS

I would like to express my deepest appreciation and sincerest gratitude to my supervisor, Dr. Sean R. Shieh, without whose guidance and persistent help, this dissertation would not be possible. His incredible patience, wisdom, understanding and encouragement throughout the research were of great value.

I would also like to thank Dr. Desmond Moser and members of his research group for lending me the use of their research facility which greatly enhanced the scope of and added an additional dimension to my research. A big thanks to Giancarlo A. Jones for sharing his knowledge about natural zircons and to Ivan Barker for helping with sample preparation, SEM imaging and EBSD mapping.

I would like to express my gratitude to my examination committee, Dr. Desmond Moser, Dr. Dazhi Jiang and Dr. Lyudmila Goncharova, for their time and valuable comments.

I wish to thank my research group for their input and interest in the project, my classmates and friends for critical analysis of my work. Your ideas helped me improve the quality of my research.

Finally, I would like to acknowledge the love and support of my family, who helped keep me going and without whom this research would not have been possible.

TABLE OF CONTENTS

ABSTRACT.....	ii
ACKNOWLEDGEMENTS.....	iii
TABLE OF CONTENTS.....	iv
LIST OF FIGURES.....	vi
LIST OF TABLES.....	x
LIST OF APPENDICES.....	xi
LIST OF ABBREVIATIONS.....	xii
1. INTRODUCTION.....	1
1.1. Zircon and its implication in modern science.....	1
1.2. Structure of zircon.....	2
1.3. Analysis of rheological properties of zircon from previous studies.....	5
1.4. Objectives.....	13
2. INSTRUMENTATION AND EXPERIMENTAL METHOD.....	14
2.1. Diamond-anvil cell.....	14
2.2. Synchrotron radiation.....	17
2.2.1. X17 beamline.....	18
2.2.2. Angle x-ray diffraction.....	19
2.3. Sample preparation.....	21
2.3.1. Diamond alignment.....	21
2.3.2. Boron-epoxy gasket preparation.....	22
2.3.3. Sample loading for diffraction experiment.....	24
2.4. Synchrotron x-ray diffraction experiment.....	27
2.5. EBSD experiment using Scanning Electron Microscope.....	30
2.5.1. SEM sample preparation.....	31
2.6. Data analysis. Instrumentation.....	34
2.6.1. Reitveld refinement and texture analysis.....	34
3. LATTICE STRAIN THEORY.....	36

4. RESULTS AND DISCUSSION.....	39
4.1. Strength of zircon based on lattice strain theory.....	39
4.2. Equation of state.....	55
4.3. Textures. Reitveld analysis.....	57
4.4. Raman spectroscopy.....	61
4.5. EBSD.....	65
4.6. Geological implication.....	71
4.7. Future studies.....	73
5. CONCLUSIONS.....	74
REFERENCES.....	76
APPENDICES.....	88
CURRICULUM VITAE.....	112

LIST OF FIGURES

1. INTRODUCTION

1.1.	Crystal structure of zircon.....	3
1.2.	Crystal structure of reidite.....	4
1.3.	Phase diagram for ZrSiO_4 (Ono <i>et al.</i> 2004).....	6
1.4.	Volume as a function of pressure for ZrSiO_4 scheelite (Scott <i>et al.</i> 2002).....	10
1.5.	Birch-Murnaghan equations of state for zircon and reidite (Ono and Tange 2004).....	10
1.6.	Zircon room-temperature data as a function of pressure (van Westrenen <i>et al.</i> 2004).....	10
1.7.	Plot of unit cell volume with increasing pressure (Dutta 2012).....	10
1.8.	Raman spectra of zircon and reidite (van Westrenen <i>et al.</i> 2004).....	12

2. INSTRUMENTATION AND EXPERIMENTAL METHOD

2.1.	Main parts of the diamond with diamond cut.....	15
2.2.	Boehler diamond cut.....	16
2.3.	Modified brilliant cut.....	16
2.4.	Drukker cut diamond.....	16
2.5.	Drilling the hole using micro-EDM in Be gasket	17
2.6.	Schematic angle-dispersive X-ray diffraction in axial geometry. σ_1 and σ_3 are radial and axial stress, respectfully. 2θ is a diffraction angle.....	19
2.7.	Schematic angle-dispersive X-ray diffraction in radial geometry. σ_1 and σ_3 are radial and axial stress, respectfully. 2θ is a diffraction angle.....	20
2.8.	Instruments used in experiment	21
2.9.	Diamonds are already mounted on the seat using mounting jig: the blue mixture is epoxy which is used to glue the diamonds to the seat.....	22
2.10.	Be gasket with 300μ hole size.....	23
2.11.	Be gasket with the 80μ hole in B-epoxy insert. B-insert size is 500μ	24
2.12.	Zircon silicate powder. A- powder sample and Be gaskets. B- sample in original package.....	25
2.13.	Mini DAC, cylinder (to the left) and piston (to the right) to the bottle with powdered nano gold which was used in the experiment.....	26

2.14.	Gold foil on the top of the diamond's culet of the mini DAC. Dark part was used in the experiment.....	26
2.15.	Be gasket before (a) and after (b) compression. Be-B-epoxy gasket with the hole filled with zircon.	26
2.16.	Photodiode scanning image along vertical direction (m3).....	29
2.17.	Photodiode scanning image along horizontal direction (m2).	29
2.18.	Quenched sample (#3) at 30 GPa before removal from the gasket. Brown color-B-epoxy mixture, zircon sample is white coloured part in the middle of the gasket.....	32
2.19.	Quenched sample (#1) at 20 GPa before removal from the gasket.....	32
2.20.	B-epoxy insert with zircon sample (#3 – left; #1 – right) mounted into epoxy before polishing.....	33
2.21.	Sample #3 (left) and #1 (right) after 3 steps of polishing: 1) polishing with blue sand paper (9microns); 2) with pink sand paper (6 microns); 3) with 0.05 microns grain size Bohler MasterPrep colloidal alumina mixture on VibroMet2.....	33
2.22.	Schematic plot of the Bragg's Law.....	34
3. LATTICE STRAIN THEORY		
3.1.	Geometry for a given ψ angle between the diffracting plane normal \hat{n} and the maximum stress axis S, $d_m(hkl)$ is a measured d-spacing of the Miller indices h, k, and l (Merkel <i>et al.</i> 2002).....	37
4. RESULTS AND DISCUSSION		
4.1.	Representative sliced with 5° XRD pattern in 2D format converted using fi2d software at P=27.7 GPa.....	40
4.2.	Representative diffraction pattern of zircon taken at P=27.7 GPa using ADXD. Bold red line represents maximum stress ($\psi=0^\circ$).....	40
4.3.	Diffraction patterns of zircon taken at different pressures using ADXD.....	42
4.4.	Variation of interplanar d-spacing for (hkl) planes with pressure (from 7 to 30 GPa).....	43
4.5.	Plot of d-spacings over diffraction angle for (101) zircon plane with different pressures.	44

4.6.	Variation of d-spacing as a function of $1-3\cos^2\psi$ for (101) diffraction line of zircon (3 rd dataset) at different pressure.	45
4.7.	Variation of d-spacing as a function of $1-3\cos^2\psi$ for (200) diffraction line of zircon (3 rd dataset) at different pressure.	45
4.8.	Variation of d-spacing as a function of $1-3\cos^2\psi$ for (112) diffraction line of zircon (3 rd dataset) at different pressure.....	46
4.9.	Variation of d-spacing as a function of $1-3\cos^2\psi$ for (312) diffraction line of zircon (3 rd dataset) at different pressure.....	46
4.10.	Differential stress/shear stress over pressure for zircon up to 30 GPa.....	49
4.11.	Differential stress/shear modulus ratio over pressure for different minerals up to 30 GPa.....	50
4.12.	Differential stress over pressure for zircon up to 30 GPa. Polynomial (exponential) fit is applied to each plane.....	52
4.13.	Differential stress over pressure for different minerals up to 30 GPa.....	54
4.14.	Equation of state of zircon at $\psi=0^\circ$, 54.7° and 90°	56
4.15.	Inverse pole figures (IPFs) obtained from Reitveld analysis showing texture development along compression axis at different pressures.....	59
4.16.	SEM image of bulk zircon grained sample. A-1500 times enlarged, B- 3000 times enlarged.....	61
4.17.	SEM picture of quenched sample of zircon powder compressed to 22 GPa in DAC using stainless steel gasket with 100 microns hole.....	62
4.18.	Location of points that were used for mapping of zircon sample using Raman spectroscopy.....	62
4.19.	Raman spectra of zircon. A- spectra collected at different pressures, pressures are shown near each spectra to the right; b- spectra collected at highest pressure (21 GPa) in different regions.....	64
4.20.	Band contrast of 500 EBSD D2 25 keV.....	65
4.21.	Composition of the sample.....	65
4.22.	Band contrast of 300 EBSD D2 25 keV.....	66
4.23.	Composition of the sample. Blue-zircon, red- reidite.....	66
4.24.	Texture development in 500 EBSD2 map 25 keV.....	67

4.25.	500 EBSD map 6 25 keV. Texture development and twinning in a zircon grain (1st sample).....	68
4.26.	Stereographic projections of 500 EBSD 6 25 keV.....	68
4.27.	Pole figures for zircon (top) and reidite (bottom) derived from EBSD technique for a quenched sample #2.....	70

LIST OF TABLES

1.1. Comparison between experimental (zircon), calculated (zircon) and calculated (scheelite) elastic parameters (Chaplot <i>et al.</i> 2006).....	8
1.2. Active Raman Modes of Zircon (Finch <i>et al.</i> 2001).....	11
2.1. Instrumental calibration parameters, NSLS, March 2014.....	28
2.2. Instrumental calibration parameters, NSLS, June 2014.....	28
4.1. Shear modulus and $Q(hkl)$ for each plane at different pressures.....	47
4.2. Texture index of zircon at different pressures. The values were obtained from E-WIMV model of MAUD software with fixed 4-fold geometry.....	60

LIST OF APPENDICES

Appendix A1. Differential stress.....	88
Appendix A2. Texture analysis of zircon powder using Material Analysis Using Diffraction software (MAUD).....	90
Appendix A3. Plots from EBSD.....	106

LIST OF ABBREVIATIONS

Au – gold

Be – beryllium

BeO – beryllium oxide

B-epoxy – boron-epoxy

BKD - backscatter Kikuchi diffraction

CeO₂ – cerium oxide

COD – Crystallography Open Database

DAC – diamond-anvil cell

DI water – distilled water

EBSD – Electron backscatter diffraction

EoS – equation of state

FWHM - peak width at half maxima

g – gram

MAUD – Material Analysis Using Diffraction

MSDS – Material Safety Data Sheet

Ppm – parts per million

SEM – scanning electron microscope

XRD – x-ray diffraction

WC seat – tungsten (wolframite) carbide seats

Zr – zirconium

1. INTRODUCTION

1.1. Zircon and its implications in modern science

Zircon, or zirconium silicate (ZrSiO_4), is a well-known ubiquitous accessory mineral (Chaplot *et al.*, 2006, Finch *et al.*, 2001, van Westrenen *et al.*, 2004). It is a common mineral in many igneous, sedimentary and metamorphic rocks. It can be found in the Earth's crust as well as in other planetary bodies (Pidgeon *et al.*, 2011). Along with its high pressure polymorph, zircon is commonly found in impact structures, such as the upper Eocene impact structures in the Barbados and New Jersey, the El'gygytgyn crater in Siberia and the Chesapeake Bay impact structure in Virginia (Glass *et al.*, 2002, Malone *et al.*, 2010, Wittman *et al.*, 2009) as well as in impact breccias and shock metamorphosed basement rocks (Bohor *et al.*, 2003, Leroux *et al.*, 1999).

Based on its physical properties and chemical composition, zircon is broadly used in the ceramics industry (Scott *et al.*, 2002), as a source of metallic zirconium and zirconium oxide (Nielsen 2000). In addition, zircon is a good alternative for conventional silicon oxide as a dielectric material in metal-semiconductor devices (Dutta and Mandal, 2012). Owing to some characteristic features of zircon, such as chemical stability, high incompressibility (Finch *et al.*, 2003), and ability to accommodate dopant ions (Akhtar 2001), zircon can be used as a material for solid state lasers (Dutta and Mandal, 2012).

Furthermore, due to its ability to retain trace elements, especially U and Th, zircon has become extremely important in geochemical and geochronological studies (Hanchar *et al.*, 1994, Hanchar and Hoskin, 2003, Heaman and Perrish, 1991). Isotopic data obtained from zircon can provide insightful information about the evolution of crust and mantle differentiation (Finch *et al.*, 2001) as well as processes occurring on other planetary bodies (Pidgeon *et al.*, 2011). Used as a well-established tool of age determination, zircon has already become a source of information of the ages for many of Earth's oldest rocks (Bowring *et al.*, 1989, Valley *et al.*, 2014, Wilde *et al.*, 2001) due to its high blocking temperature and resistance to severe physical conditions (Dutta and Mandal, 2012). Moreover, zircon is a good geochemical indicator for oxygen isotopes. Unlike other minerals, zircon does not lose any of the isotopes during metasomatic events (King *et al.*, 1998).

Zircon is one of the popular refractory minerals with low thermal conductivity and a high melting point (Chaplot *et al.*, 2006). This means that, thanks to its good thermal shock resistance it can be used as an indicator of impact deformations. Moreover, due to its accuracy and ability to retain trace elements, it can be used for dating the formation of melt and impact events. Specifically, it can be used to separate shocked and potentially shocked country rocks (Leroux *et al.*, 1999).

Zircon is a very durable and long-living natural mineral, which can retain fissile nuclides for millions of years. Due to this property, it was proposed as a candidate for the geological disposal of hundreds of tons of radioactive plutonium, which is a major issue after dismantling nuclear weapons (Ewing 1997, Luo and Ahuja, 2008). Using such material allows us to dispose of radioactive weapons' plutonium in the environment, even with hydrothermal conditions, without the possibility of leakage or contamination, unlike using borosilicate waste form glass (Luo and Ahuja, 2008).

1.2. Structure of zircon

Zircon is an orthosilicate with a tetragonal structure (Figure 1.1). This mineral has an $I4_1/amd$ space group with lattice parameters $a = 6.607 \text{ \AA}$ and $c = 5.981 \text{ \AA}$. Zircon has the general formula ABO_4 , where Zr^{4+} and Si^{4+} are on the positions of cations with 4-2m symmetry. Oxygen anion stands on site m (Finch and Hanchar, 2014). Moreover, the only refinable atomic sites in the zircon structure are the y and z positions occupied by O ($y = 0.066$, $z = 0.195$) (Finch *et al.*, 2001). In other words, the zircon structure consists of SiO_4 tetrahedra and ZrO_8 dodecahedra that share edges and corners and are parallel to crystallographic axis c (Guscsik *et al.*, 2004).

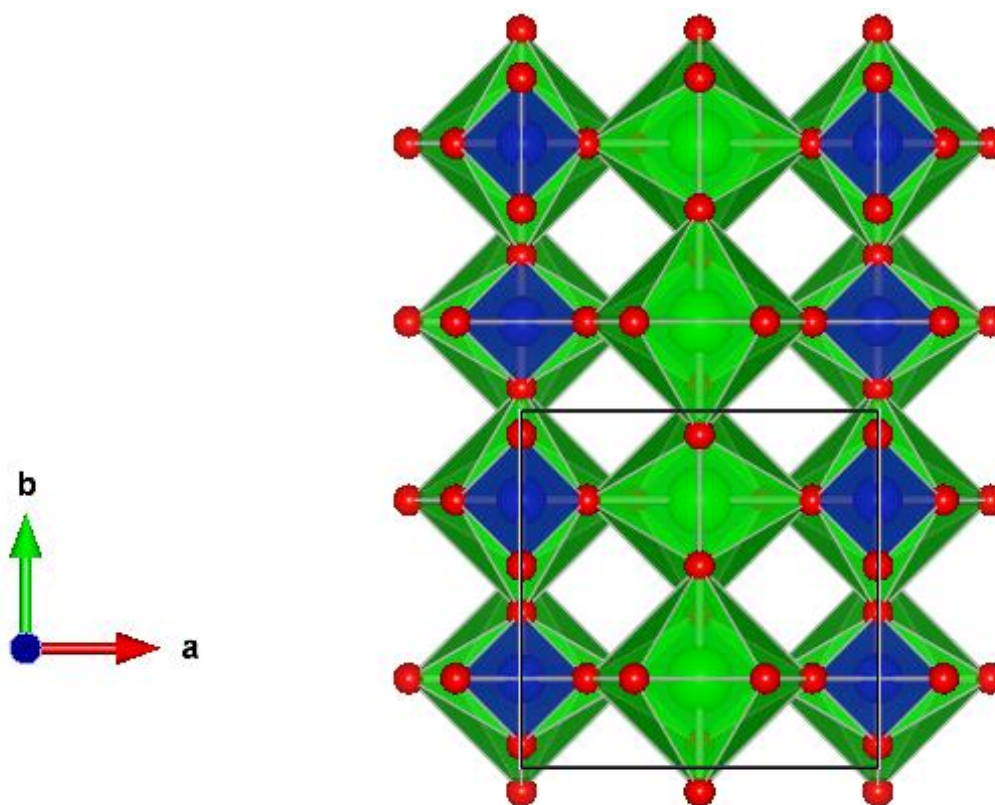


Figure 1.1. Crystal structure of zircon. Red spheres - oxygen, green polygons - Zr, blue polygons – Si.

Under pressure, tetragonal zircon undergoes a first order phase transition to a scheelite-structured phase (space group $I4_1/a$, $a = 4.738 \text{ \AA}$ and $c = 10.51 \text{ \AA}$; $V = 235.85 \text{ \AA}^3$) (Figure 1.2) along with a 9.9% density increase (Reid and Ringwood, 1969, Liu 1979). The high pressure phase of zircon with the scheelite structure reidite was synthesized in laboratory conditions by Reid and Ringwood, and was named in honor of its founder, Alan Reid (Glass *et al.*, 2002). Additionally, reidite has been recently discovered in naturally occurring samples of impact craters (Glass and Liu, 2001).

A recent in situ study of synthetic zircon resulted in the detection of the transition to reidite slightly below 20 GPa (van Westrenen *et al.*, 2004). For naturally shocked sample the proposed transition pressure was slightly below 30 GPa (Kusaba *et al.*, 1985). The transition pressure is sufficiently affected by temperature, as heating leads to lowering of the transition pressure (Gucsik *et al.*, 2004).

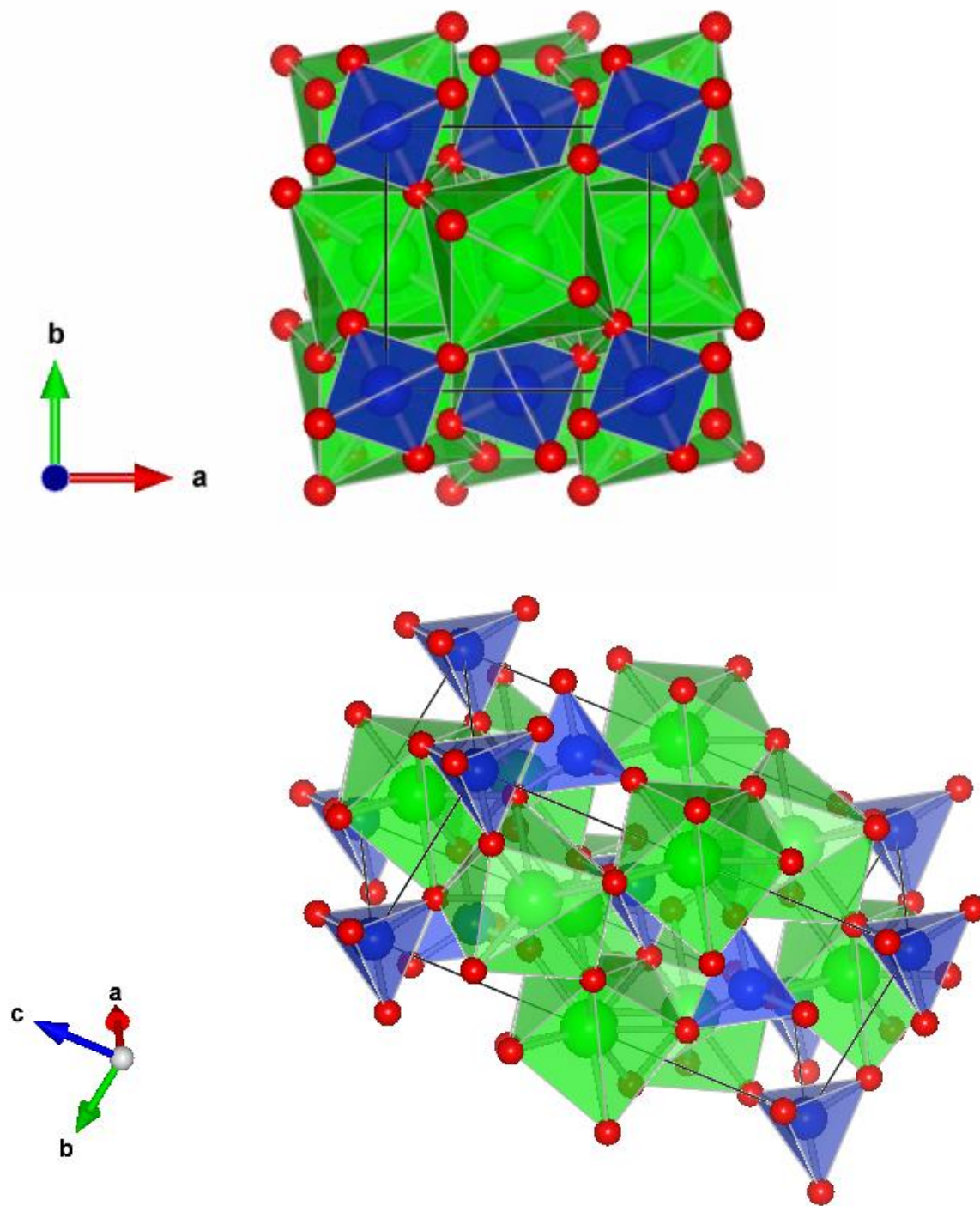


Figure 1.2. Crystal structure of reidite. Red spheres- oxygen, green spheres- Zr, Si.

1.3. Analysis of rheological properties of zircon from previous studies

Phase diagram of zircon

One of the first reliable phase diagrams based on temperature-related phase transitions, was proposed by Curtis and Sowman, who analyzed zircon of high purity (99% pure) using the X-ray diffraction method at ambient pressures (Curtis and Sowman, 1953). As a result, the solid state dissociation of zircon was discovered starting from 1540°C (2800°F) to approximately 1677°C (Curtis and Sowman, 1953). Quite different values were reported by Buttermann and Foster (1967). According to their research, the solid dissociation of zircon can occur in the range of $1676 \pm 7^\circ\text{C}$ to $1687 \pm 4^\circ\text{C}$. Thermal solid state stability research of a zircon was highly improved by Anseau *et al.* (1976). They proposed a phase diagram that could solve the previous $\sim 130^\circ\text{C}$ disagreement on the lower temperature of dissociation. As a result of Anseau's research, the phase diagram proposed by Curtis and Sowman in 1953 was found to be more reliable. Dissociation was detected as low as 1525°C and was relatively small or constant at 1650°C (Anseau *et al.*, 1976).

After discovery of phase transformation from zircon to the scheelite structure, the phase diagram was improved by analysing temperature-pressure dependent phase transition (zircon-reidite). Ono *et al.*, in 2004 (Figure 1.3) reported a phase boundary between zircon and reidite at around $T = 1100\text{--}1900\text{ K}$ and $P\text{ (GPa)} = 8.5 + 0.0017 \cdot (T - 1200\text{ K})$. They also proposed a summarized phase diagram that determined boundaries between zircon, reidite and dissociated oxides (Ono *et al.*, 2004).

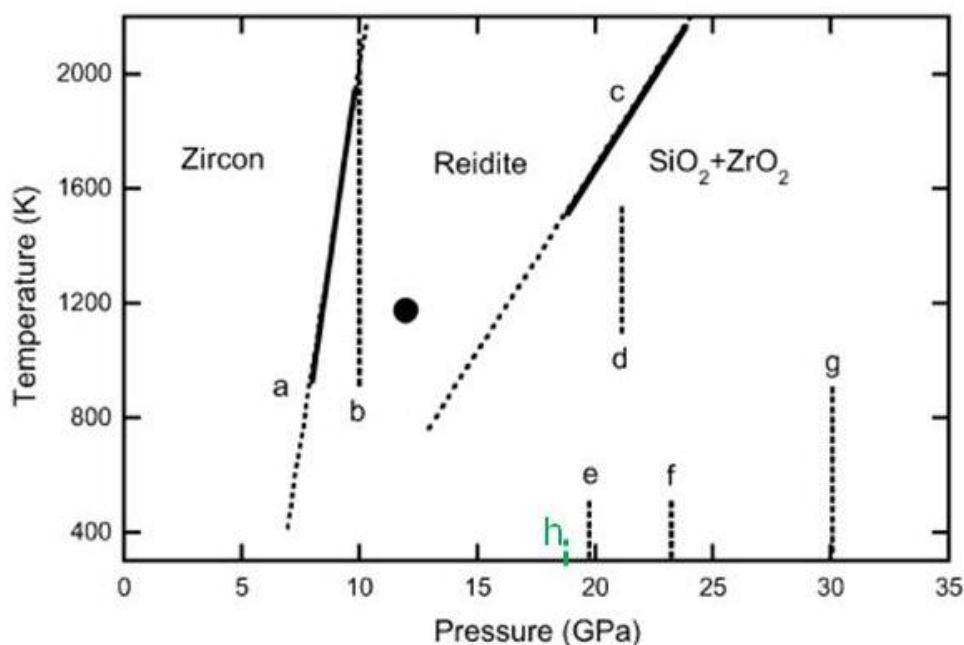


Figure 1.3 Phase diagram for ZrSiO_4 (Ono and Funakoshi, 2004). A,b, zircon-reidite (Ono *et al.*, 2004); c, decomposition of reidite (Tange and Takahashi, 2004); d, decomposition of reidite (Liu 1979); e-zircon-reidite (van Westrenen *et al.*, 2003); f, zircon-reidite (Knittle and Williams, 1993); g, zircon-reidite (Kusaba *et al.*, 1985); h, zircon-reidite (current study); solid circle, reidite (Reid and Ringwood 1969).

Chaplot *et al.* (2006) partially improved the phase diagram based on the free energy calculations in zircon and scheelite phases. They suggested that phase transformation between phases occurs at 10 GPa 1300°C in the zircon stability field (Chaplot *et al.*, 2006).

From the high pressure research conducted at ambient temperatures zircon to reidite transition was detected at above 23 GPa (Knittle and Williams, 1993); later it was improved and reported by van Westrenen *et al.* (2004) (19.6 GPa). This value is almost twice higher than reported for high-pressure – high-temperature experiments. Current study was aimed to detect the phase transformation using nonhydrostatic compression of zircon powder inside the diamond anvil cell. This resulted in observation that zircon transforms to reidite above 18 GPa.

High pressure polymorphs

As has been stated earlier (see chapter 1.1), zircon changes its structure from zircon into scheelite under static compression slightly below 20 GPa, and under shock compression at 30 GPa. Also its high pressure polymorph survives under temperatures up to 1000°C (Bohor *et al.* 1993, Leroux *et al.* 1999).

Reidite, a high pressure polymorph of zircon, after being synthesized in the laboratory by Reid and Ringwood in 1969 (Reid and Ringwood, 1969), was also discovered in the ejecta layer in the Chesapeake Bay impact structure, in Eyreville drill cores (Glass *et al.*, 2001, Malone *et al.*, 2010). Glass and co-workers reported different structure (*scheelite*) for reidite and proposed it to be used as a new tool for calibrating peak shock pressures in impact structures (Glass *et al.*, 2002).

Zircon-reidite phase transition is still under investigation. Above 20 GPa, according to Tange and Takahashi (2002), reidite dissociates into oxides. Ono *et al.* (2004) detected that zircon transforms to reidite at $P=10$ GPa (laser-heated DAC experiment with synchrotron radiation). Tange and Takashi (2002) reported that a stability field of reidite existed between 8 to 20 GPa (shock experiment). Reidite transformation observed by van Westrenen *et al.*, (2004) (ambient temperatures, hydrostatic compression in DAC) was detected at 19.7 GPa, which was 3 GPa lower than the value reported by Knittle and Williams (1993). According to Malone (2010) martensitic zircon-reidite transformation is still not complete at 40 GPa (some relict grains are still present). Though under vacuum zircon starts to decompose to oxides at temperatures as low as 1500°C (Malone 2010).

The most recent discovery related to high pressure phases of zircon was published by Dutta and Mandal (2012). They found that zircon becomes metastable at 7.3 GPa, where it undergoes first-order transition to reidite (scheelite structure, $I4_1/a$), and later it undergoes a second order phase transition to a monoclinic structure (wolframite type, $P2_1/c$) at 75.8 GPa (Dutta and Mandal, 2012).

Elastic parameters

Elastic parameters for both zircon and reidite were reported by Chaplot *et al.*, in 2006. They also proposed bulk modulus for both phases (see Table 1.1).

Table 1.1 Comparison between experimental (zircon), calculated (zircon) and calculated (scheelite) elastic parameters (Chaplot *et al.*, 2006).

Elastic constant	Experiment (Zircon)	Calculated (Zircon)	Experiment (Scheelite)	Calculated (Scheelite)
C_{11}	424.4	432		470
C_{33}	489.6	532		288
C_{44}	113.3	110		74
C_{66}	48.2	39		133
C_{12}	69.2	73		241
C_{13}	150.2	180		255
B	205 (8)	251	392 (9), 301 (12)	303

Bulk modulus has been derived using different techniques and reported by various authors. The values obtained were in the range of 199 GPa (van Westrenen *et al.*, 2004) to 245 GPa (Hazen and Finger 1979) for zircon, and 301 ± 12.5 GPa for scheelite-structured reidite (Scott *et al.*, 2002). Two values for isothermal bulk modulus (227 ± 2 GPa if $K'_0 = 6.5$ and 234 GPa if $K'_0 = 4$) were suggested by Hazen and Finger (1979). A slightly higher value was reported ($K_{0T} = 245$ GPa) by Crocombette and Ghaleb (1999).

Van Westrenen *et al.*, (2004) obtained a bulk modulus $K_{T0} = 199 \pm 1$ GPa that was much lower than ever before proposed, but in good relationship with the one reported by Ono $K_{T0} = 205 \pm 8$ GPa (Ono *et al.*, 2004). The differences in compressibility values were explained by the

impurity of the starting material (content of Hf or other elements). In addition, that impurity of more than 1% could cause a reduction in bulk modulus of up to 10 GPa (van Westrenen *et al.*, 2004)

Tkachenko *et al.* (2007) studied radiation-amorphized zircon under direct compression. According to their results, structural transformation occurred at 4 GPa. The reported bulk modulus was 94 GPa, which is much lower than that of crystalline material. They also reported shear modulus which was 92 ± 5 GPa and 48 ± 4 GPa respectively.

Equation of State

As a result of static compression experiments at pressure of up to 52.5 GPa, Scott *et al.*, (2002) detected that zircon is the most incompressible material with SiO_4 polyhedra. He derived the bulk modulus for scheelite structured materials, and proposed an equation of state for zircon with scheelite structure (Figure 1.4). He used a second order Birch-Murnaghan equation of state to obtain the required fit. The K_{oT} value was obtained from the plot of normalized pressure (F) to Eulerian finite strain (f) (Scott *et al.*, 2002).

Another equation of state was obtained using DAC coupled with YAG (yttrium-aluminum-garnet) laser heating (Ono and Tange, 2004) (Figure 1.5). They heated the sample in order to release deviatoric stress. Diffraction patterns were collected at ambient temperatures. Data was fitted to a 3rd order Birch-Murnaghan equation of state. They obtained two separate equations for zircon and reidite. Van Westrenen also presented an equation of state for zircon at ambient temperatures. He used pure synthetic zircon and He as a pressure medium (Figure 1.6) (van Westrenen *et al.*, 2004). His experiment was also conducted in DAC. He used an angle-dispersive technique.

The latest reported equation of state was in 2012 (Dutta and Mandal, 2012). The authors conducted a high pressure experiment up to 75.8 GPa (Figure 1.7). They separated stable and metastable fields of zircon high pressure phases based on their analysis of elastic constants.

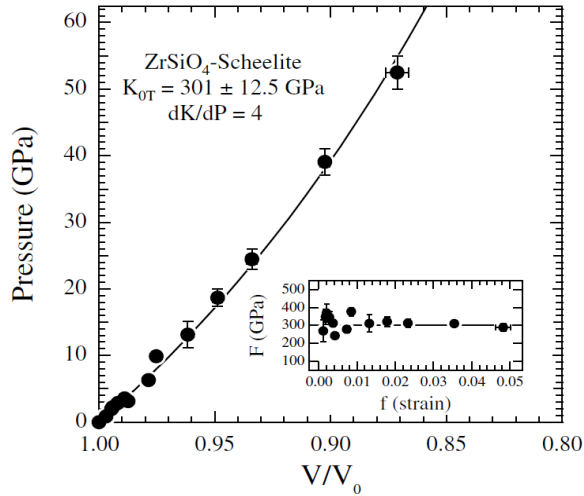


Figure 1.4. Volume as a function of pressure for ZrSiO_4 scheelite. The solid line is the second order fit to the Birch-Murnaghan equation of state. The inset shows data plotted as a normalized pressure (F) vs. Eulerian finite strain (f), from which the value of K_{0T} is obtained. (Scott *et al.*, 2002).

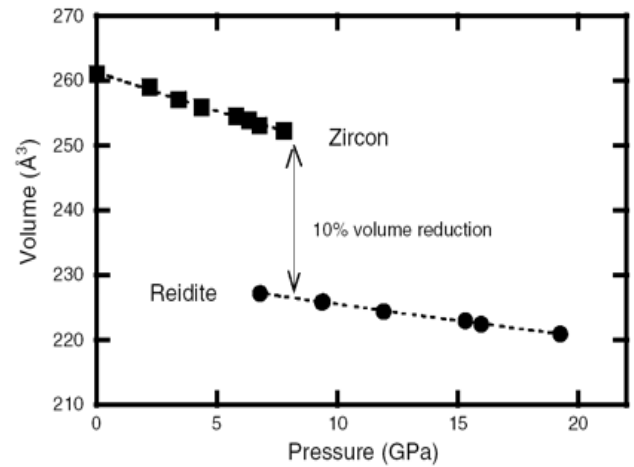


Figure 1.5. Birch-Murnaghan equations of state for zircon and reidite (dashed lines). Symbols are as follows: solid squares, zircon; solid circles, reidite. (Ono and Tange 2004).

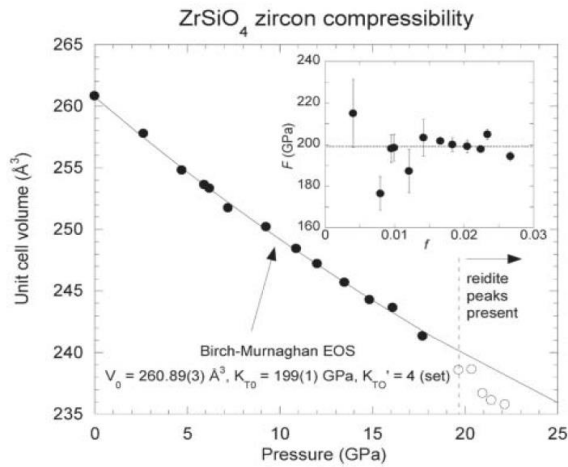


Figure 1.6. Zircon room-temperature data as a function of pressure. K_{0T} is fixed at 4. Line- best fit to a Birch-Murnaghan equation of state. Solid symbols- zircon data, open symbols- reidite+zircon data. Insert- normalized pressure F - Eulerian strain f . (Van Westrenen *et al.*, 2004).

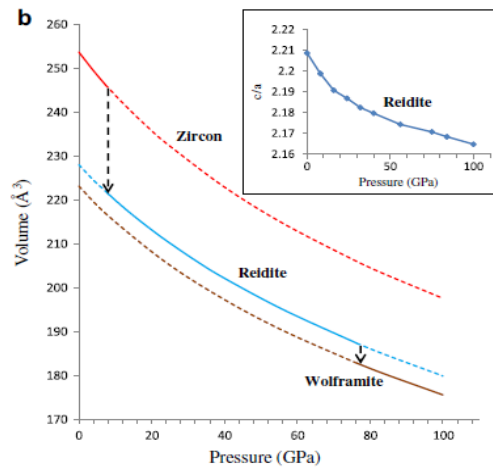


Figure 1.7. Plot of unit cell volume with increasing pressure. The solid and dashed lines indicate stable and metastable fields. Arrows symbolize the volume collapse during the phase transitions. The inset shows the c/a axial ratio as a function of pressure. (Dutta and Mandal, 2012).

Raman Spectroscopy

The vibration spectrum of zircon was first reported by Dawson *et al.*, in 1971. Later their data were supported by Gucsik *et al.*, in 2004. Finch and Hanchar (2001) concluded that zircon has 12 active Raman modes (Finch *et al.*, 2001).

$$2A_{1g} + 4B_{1g} + 1B_{2g} + 5E_g = 12$$

Table 1.2 Active Raman Modes of Zircon (Finch *et al.*, 2001).

WP	A _{1g}	A _{2u}	A _{2g}	A _{2u}	B _{1g}	B _{1u}	B _{2g}	B _{2u}	E _u	E _g
16h	2	.	.	.	2	.	1	.	.	3
4b	1	1
4a	1	1

It has been reported that the spectrum of zircon exhibits strong anti-symmetric stretching of the SiO₄ group (ν_3) near 1008 cm⁻¹ at ambient pressures. The band near 974 cm⁻¹ is assigned as a Si-O stretching band (ν_1 , symmetric stretching) with A_{1g} symmetry (Gucsik *et al.*, 2004). Bands at lower frequencies are mostly attributed to bending vibrations of SiO₄ groups and external bands are associated with SiO₄ group motions with respect to Zr atoms and its motions (Dawson *et al.*, 1971).

A Raman spectrum for high pressure polymorph of zircon, reidite, was first separated by Knittle and Williams in 1993. At that time an irreversible first order transition from zircon to reidite was detected at 23±1 GPa. Their discovery was in good agreement with high temperature, high pressure experiments (according to obtained lattice parameters, a: 0.4726nm and c: 1.0515 nm) (Knittle and Williams, 1993). The Raman experiment by van Westrenen *et al.* (2004) confirmed zircon-reidite transition. Although they failed to obtain clear zircon spectra (Figure 1.8), they were able to conclude that in the stability field of reidite some Raman modes of zircon will still be present (Van Westrenen *et al.*, 2004).

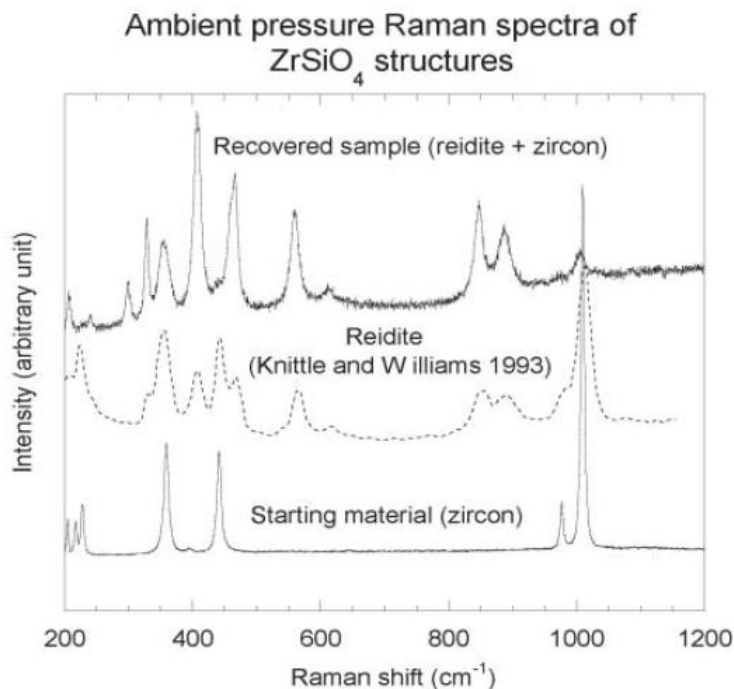


Figure 1.8 Raman spectra of starting material (bottom line); reidite raman spectra (from Knittle and Williams 1993) – dotted middle line; top- recovered sample collected after 106 hours of the experiment at 27GPa (van Westrenen *et al.*, 2004).

Deformation of zircon

Empirical evidence establishes that zircon can preserve primary geochemical information, though still there are only few detailed studies on the microstructural analysis of deformed zircon. The most detailed study was based on transmission electron microscopy (TEM), which provided the information about grain-scale deformation processes and mechanisms in major-forming minerals (Leroux *et al.*, 1999).

Zircon is one of the popular refractory minerals, which means that it can be used as an indicator for impact deformations. Moreover, due to its ability to retain trace elements, such as U and Th, zircon can be used for dating the formation of the melt and impact event to separate shocked/potentially shocked country rocks (Leroux *et al.*, 1999). Recent studies show that zircon can be found in impact breccias and shock metamorphosed basement rocks (Bohor *et al.*, 1993, Leroux *et al.*, 1999). Additionally, zircon age determinations are believed to correlate with their

microstructures. Different deformations create different pathways for diffusion, which results in uncertainties in age determination. In addition, crystal-plastic deformation in zircon can also affect zircon geochemistry (Reddy *et al.*, 2006).

Most importantly, knowledge of deformation of zircon at mantle conditions is very poor. Zircon grains were discovered in host igneous rocks with deformations, which are typical for low-melt, mid-low crustal cumulates (Reddy 2008). The study of zircon under high temperatures and pressures can help us better understand the physical properties of zircon and determine the nature of deformations at mantle conditions. To date, deformations in zircon have mainly been studied by TEM, SEM, EBSD, Cathodoluminescence and Raman. High pressure synchrotron radiation method provides the opportunity to in situ examine the deformation behavior of zircon at high pressures which brings the research to the next level of understanding.

1.4. Objectives

In this research, the main purpose aims to investigate the behavior of pure zircon under high pressure. The strength and elasticity of zircon powder were measured in DAC using radial X-ray diffraction by synchrotron radiation. In addition, the quenched samples were analyzed by electron backscatter diffraction (EBSD) using scanning electron microscope (SEM).

Preliminary objectives of this study were to:

- 1) Conduct an angle-dispersive X-ray diffraction experiment for two polycrystalline zircon samples: commercial (MP Biomedicals) and synthetic;
- 2) Determine the equation of state of zircon;
- 3) Measure the differential stress of zircon using lattice-strain theory (Singh 1993);
- 4) Measure the differential stress of each crystallographic plane and evaluate the elastic-plastic behavior of the planes under high pressure;
- 5) Study texture development under high pressure;
- 6) Detect zircon-reidite phase transformation;
- 7) Investigate the influence of grain size on deformation under pressure;
- 8) Analyze the crystal structure and strain of the quenched sample using EBSD.

2. INSTRUMENTATION AND EXPERIMENTAL METHOD

As one of the powerful tools for *in situ* study of the Earth's interior, high pressure research is of great importance. High pressure experiments have significantly improved in the past few decades and have contributed to Earth Sciences as well as other sciences and led to big discoveries in novel materials and their physical properties.

Two main types of apparatus are commonly used in high pressure static experiments: Large Volume Press (LVP) and Diamond-Anvil Cell (DAC). The main idea of the LVP experiment is to squeeze the sample between tungsten carbide anvils. However, the larger sample size has the limitation related to achievement of pressure, as it is hard to achieve pressure higher than 35-37 GPa without braking the tungsten carbide anvils (Xu *et al.*, 2002). The “comfortable” pressure range for the most types of the LVP is below 23 GPa. With a diamond-anvil cell one can obtain pressure up to 300 GPa by using diamonds of gem quality. Certain other flawless gem stones were tested as possible diamond substitute, such as sapphire and cubic zirconia, but the maximum possible pressure reached by using those materials did not exceed 30 GPa (25.8 and 16.7 respectively) (Xu *et al.*, 1996, 2002). Another synthetic analogue of diamond - moissanite was recently used in DAC. Experiments conducted with it were successful and allowed scientists to acquire pressure more than 50 GPa (Xu *et al.*, 2002).

In this study, the strength of zircon was investigated using the angle-dispersive X-ray diffraction method using DAC in a radial geometry. Diffraction patterns were obtained by probing the sample with synchrotron radiation at beamline X17C, National Synchrotron Light Source, Brookhaven National Laboratory, NY.

2.1. Diamond-anvil cell

A diamond-anvil cell is a device that consists of two opposed anvils that can create high pressure. It is the most fitted pressure device for monitoring materials optically under extreme pressures and temperature. Using modern DACs it is possible to reach pressures that are typical at lower mantle and core conditions (Oger *et al.*, 2005). Pressure is usually measured by using pressure standard, such as ruby, Au, NaCl etc. For lower pressure (between 0.1 to 600 Mpa) recently a “low pressure DAC” was designed which is mainly used in biology. To maintain

hydrostatic conditions in a regular high-pressure DAC, an appropriate pressure medium should be sealed along with the sample. One can use gas (Ar, He, Ne or N₂), liquid (silicon oil or ethanol-methanol in 4:1 ratio) or solid material (NaCl, KBr and MgO) as a pressure medium.

The main parts of the DAC are the diamonds. They should be flawless diamond of gem quality (Figure 2.1), usually around 1/3-1/4 carat sized (they can be bigger/smaller depending on the purpose of the experiment). Three main cuttings are usually used in DAC: Boehler-Almax, drukker standard cut and modified brilliant cut (Figure 2.2-2.4).

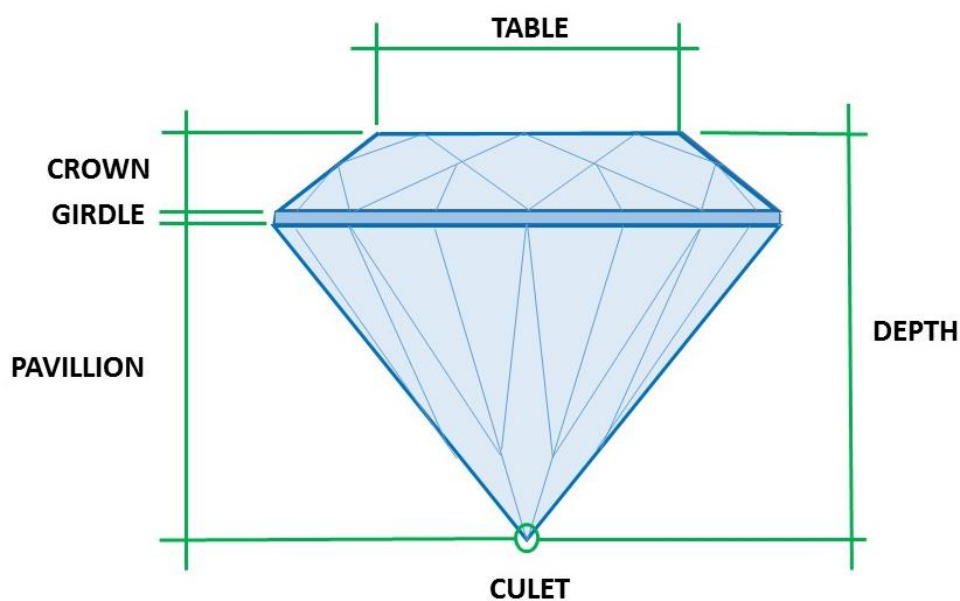


Figure 2.1 Main parts of the diamond with diamond cut.

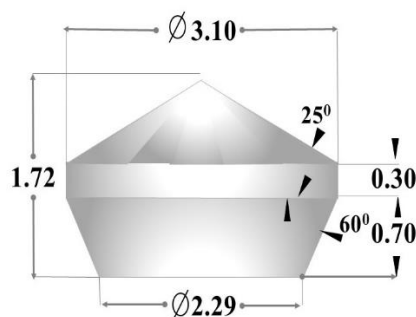


Figure 2.2 Boehler diamond cut.

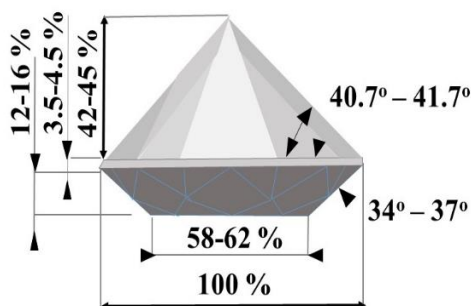


Figure 2.3 Modified brilliant cut.

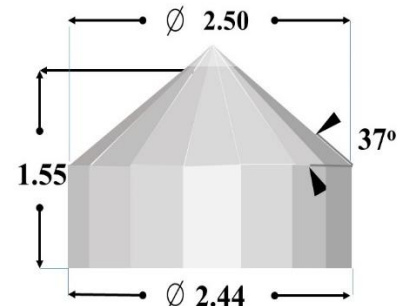


Figure 2.4 Drukker cut diamond.

Diamonds with the Boehler type of cut are optimized to support their crowns (Figure 2.2). This type of cutting requires a special tungsten carbide seat (Boehler 2006). The modified brilliant cut has a table polished with 16 facets, so the culet also has 16 sides (Figure 2.3). The table in this kind of diamond is ground down towards the girdle in order to increase the initial applied force (Katrusiak and McMillan, 2003). The drukker cut (Figure 2.4) was designed using a maximised height/base ratio. It is derived from a regular brilliant cut by reducing the number of facets and lowering the table. The higher the height/base ratio is, the higher the maximum load the anvil will sustain (Ewing 1987, Seal 1984).

In regular DAC, the sample is trapped in a special “chamber” (gasket) between two opposed culets of diamonds. The gasket can be made of metal (stainless steel, Re, Be) or another material (B-epoxy + kapton). The material of the gasket depends on the conditions and goals of the experiment. The gasket’s main purpose is to confine the sample and support the anvils (Hemmley and Ashcroft, 1998). Gasket preparation usually consists of three steps:

- 1) mounting of the gasket inside DAC between two diamonds;
- 2) preindentation of the gasket (calibrated by ruby and water); a perfect gasket should have a thickness of around 20–40 μ (corresponds to pressure around 22–25 GPa);
- 3) drilling the hole in the middle of the preindented region (Figure 2.5) (Lorenzana *et al.*, 1994).

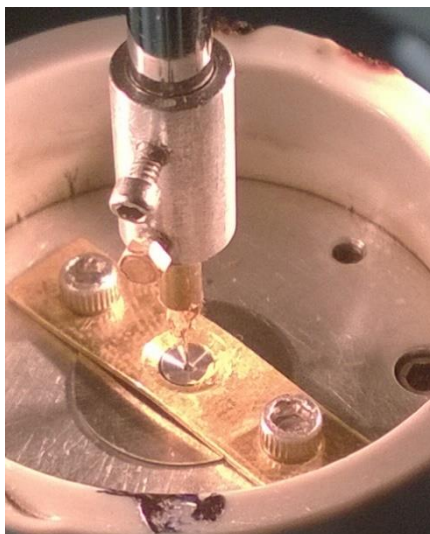


Figure 2.5 Drilling the hole using micro-EDM in Be gasket.

2.2. Synchrotron radiation

Synchrotron radiation is an exceptional tool in material science. By providing intensely bright radiation it makes probing of a very small sample possible (Mitra 2004). Since its first demonstration in the 1950s the facility has evolved from 1st to 3rd generation (which has already been in use at Advanced Proton Source, Chicago, for almost 15 years).

Synchrotron radiation is electromagnetic radiation emitted radially by electrons in a magnetic field (Sokolov and Temov, 1967). Third generation synchrotron facilities produce highly collimated light that covers a broad spectrum (from 1 keV to 40 keV). The availability of this kind of light gives an incredibly good spectroscopic resolution for light elements (C, N, O, Na, F, Cl, S, Al), as well as for elements with $Z \geq 18$ at the level of the first parts per million (ppms) (Kotzer 2004).

The application of synchrotron radiation has proven to be extremely helpful in geosciences, environmental and material sciences. By its abilities to analyze micron scale samples and detect the behavior of the material under extreme conditions, it is one of the most effective tools in mineral physics research. Moreover, synchrotron radiation is applicable in X-ray Absorption Spectroscopy (XANES/XAFS), X-ray Fluorescence (SXRF, Tomography), microscopy and synchrotron X-ray diffraction (Kotzer 2004).

In general, hardness is calculated from the size of the indentation mark left by the tip of an indenter. In turn, the size of an indent depends on the material's response to compression, and its capacity to withstand deformations in directions different from that of the applied load (Haines *et al.*, 2001). Since examining those bond deformations and stress states of materials is a nearly impossible task, high-pressure X-ray diffraction can be used as an appropriate tool to characterize a material's response under compression (Chung *et al.*, 2007, Kavner *et al.*, 2012, Xie *et al.*, 2012).

2.2.1. X17 Beamline

In order to reach temperature and pressure from the lower crust to the core special equipment is required (Hong *et al.*, 2011). The beamline X17, which is located in Brookhaven National Laboratory, Upton, NY is a perfect instrument for high pressure diamond-anvil cell research. This beamline is considered as the longest running high-pressure beamline in the world. Various materials (minerals, metals, nanocrystals etc) can be analyzed there (Hu *et al.*, 2002). As a result we can get information about strength, compressibility, phase transition, equation of state and other important properties for the materials. The X17 facility consists of two stations (X17C and X17B3) shared a superconducting wiggler beam line and a sample preparation laboratory (Hong *et al.*, 2011).

For X17B3 beamline it is possible to obtain high-pressure data using an angle-dispersive X-ray diffraction method with monochromatic light (~30 keV to ~80 keV). Also since 2011 it has become possible to conduct *in situ* laser heating as beams can be focused to ~10 μ m at 30 keV on X17B3. This method can be used for the measurement of distorted/amorphous materials as well as crystalline structures and even nanomaterials (Hong *et al.*, 2011).

The X17C beamline is the facility for analyzing polycrystalline samples in axial or radial geometry. This beamline can be used for obtaining angle and energy dispersive x-ray diffraction data (Hong *et al.*, 2011). Samples can be analyzed under pressures up to 200 GPa at ambient temperatures or up to 800°C. X-ray energies can vary from 5 to 80 keV. Adjustable beam size from 1mmx1mm to 20x23 μ m is obtainable by using focusing mirrors and slits.

2.2.2. Angle-dispersive X-Ray Diffraction

Angle-dispersive X-Ray diffraction allows us to study the behavior of the material under compression and the ability of the material to respond to applying forces. We can study material in two principal geometries – axial (Figure 2.6) and radial (Figure 2.7).

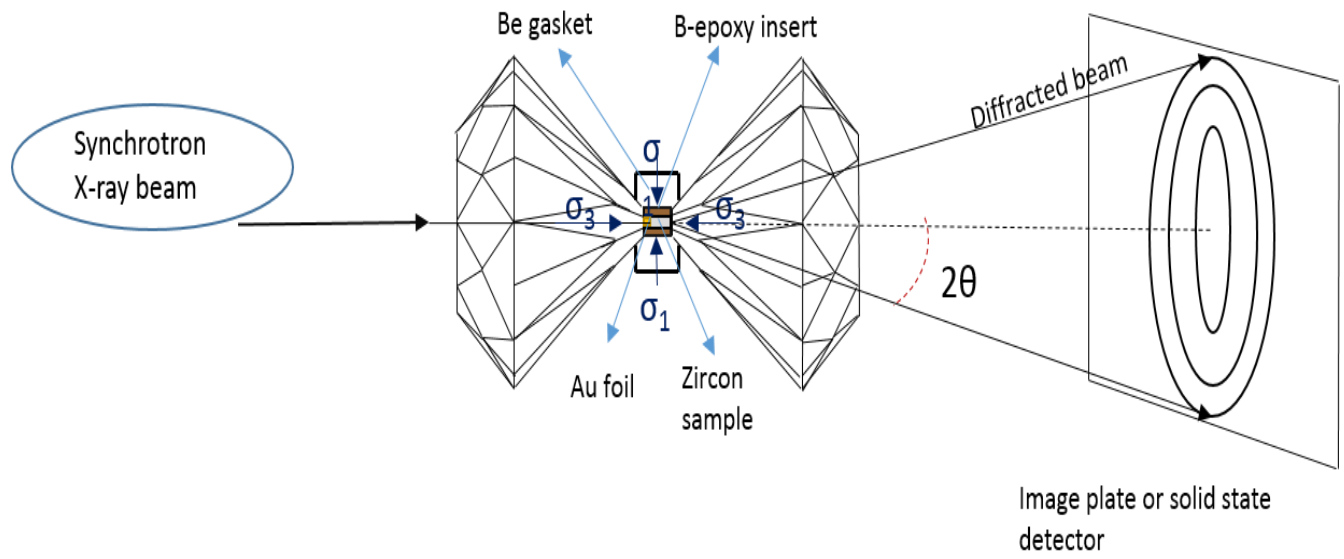


Figure 2.6. Schematic angle-dispersive X-ray diffraction in an axial geometry. σ_1 and σ_3 are radial and axial stress, respectively. 2θ is a diffraction angle.

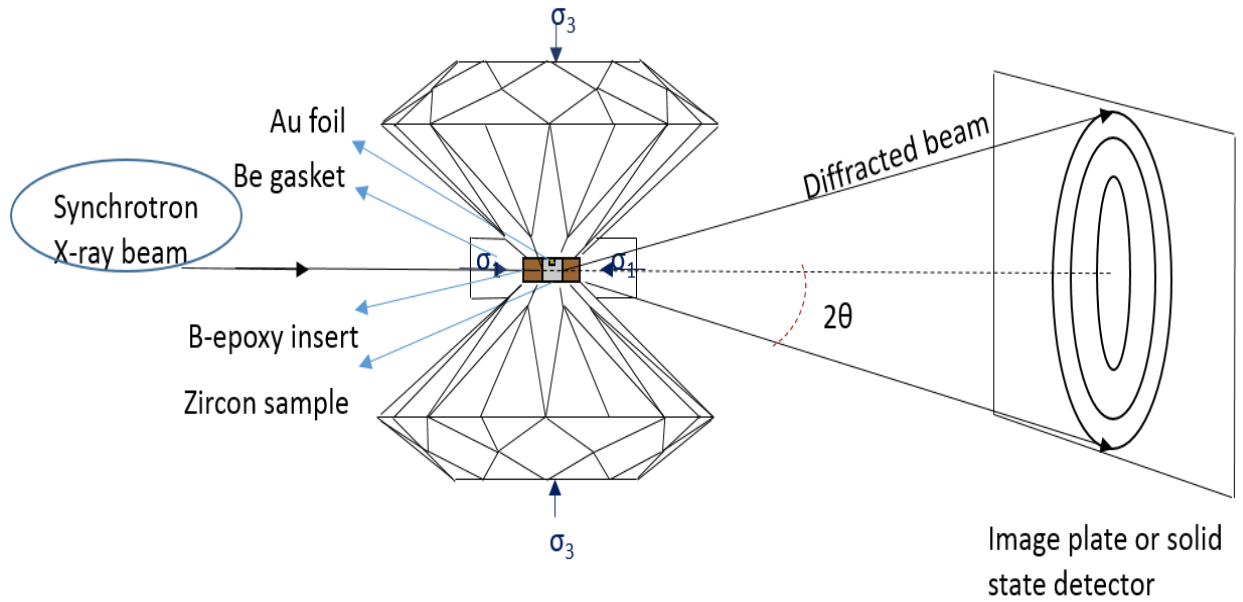


Figure 2.7 Schematic angle-dispersive X-ray diffraction in a radial geometry. σ_1 and σ_3 are radial and axial stress, respectively. 2θ is a diffraction angle.

Radial x-ray diffraction is the technique that allows us to study the mechanical properties of the polycrystalline material under non-hydrostatic conditions in diamond-anvil cell (Duffy 2007, Mao *et al.*, 1998, Merkel 2006, Merkel *et al.*, 2002). The transparent gasket for X-rays that holds the sample is mounted between two anvils in DAC. Merkel and Yagi (2005) used Kapton tape with a boron-epoxy mixture insert to probe the samples with minimum contribution from the gasket. In this research, Be gaskets with boron-epoxy insert were used (He *et al.*, 2004). No pressure medium is used in order to maintain the non-hydrostatic state. The sample is compressed uniaxially and X-ray beam goes through the sample and gasket. If Bragg's law (4.1) is satisfied, the diffraction pattern that is obtained during the experiment shows lattice planes at different azimuthal angles with respect to maximum (axial) and minimum (radial) stress directions (Singh 1993). While increasing pressure, one can observe d -spacings change due to elastic deformation. The data can be used to obtain differential stress values and yield strength, at which material undergoes plastic deformation (Merkel *et al.*, 2008, Ratteron *et al.*, 2012, Singh 1993, 1998, 2004, Weidner *et al.*, 2004) Also it helps to understand the behavior of the slip systems and development of aggregate anisotropy (Miyagi *et al.*, 2009).

In other words, due to the close relation of yield strength to the materials' hardness, knowing the differential stress of the mineral can provide us with insightful information into the mechanical properties of the studied material and explain the nature of lattice strains under deformation (Xie *et al.*, 2014).

2.3. Sample preparation

2.3.1. Diamond alignment

Diamonds should be mounted into the DAC and perfectly aligned. Various instruments have been developed to make this action easy (Figure 2.8). Perfect alignment is extremely important in order to maintain the good condition of the diamond, as during the experiment when pressure is applied, the diamond is very susceptible to breakage. In order to mount diamond we need a diamond, tungsten carbide (WC) seat with beveled sides, epoxy, set screws and mounting jig (Figure 2.9). The epoxy is mixed with a catalyst (7-10% of hardener by weight). When the diamond is mounted exactly in the centre of the seat, we apply the epoxy and leave it overnight to harden. The next morning, the diamond can be mounted into the DAC.

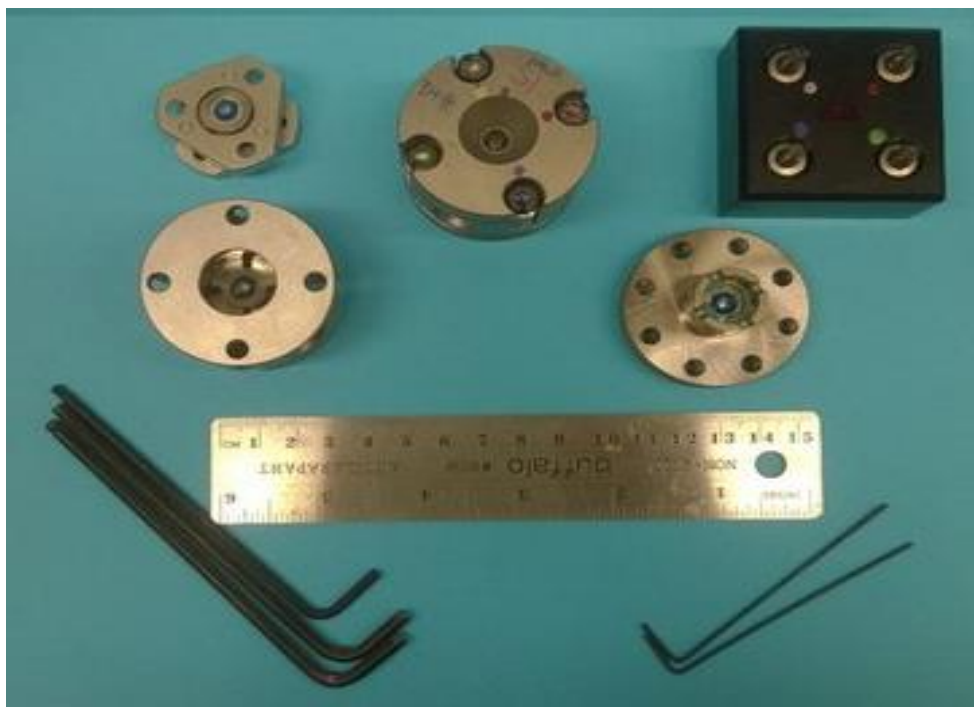


Figure 2.8 Instruments used in experiment. From left top: mini DAC, DAC, 4 screws with washers, cylinder part of DAC, piston part of DAC, wrenches of different sizes.



Figure 2.9 Diamonds are already mounted on the seats using mounting jig: the blue mixture is epoxy used to glue the diamonds to the seats.

The next step is to mount the diamond seat into the cylinder and piston parts of the DAC. By using four pin screws, we make sure that the culet of the diamond of the piston part of the DAC appears at the same position as the culet from the cylinder part and their positions are located exactly in the center of the cell. After making sure that the culets match each other, we check if there are any Newton rings on the culet by slightly compressing the cell. Newton rings appear if there is any space between the culets (the physical reason is the interference of the light with air). To avoid the appearance of Newton rings it is necessary to use a spacer. A spacer should be placed between the piston and cylinder parts of the DAC, the cell should be closed and compressed using set screws. After alignment is done, it is possible to start the sample preparation.

2.3.2. Boron epoxy gasket preparation

In this study, a Be gasket with a boron-epoxy insert as a sample chamber was used. The preparation of this kind of gasket takes a lot of time and consists of three main steps:

- 1) preparation of Be gasket;
- 2) boron-epoxy insert formation (from boron-epoxy mixture);
- 3) drilling the hole in the boron-epoxy gasket.

First step of the procedure was to prepare the Be gasket. In order to do that we took Be gaskets of two different sizes: gaskets with different preindentation size (previously made by 300 μ and 500 μ culet sized diamonds). Later the preindented part was removed from the gasket (Figure 2.10). This process was done to prepare that space for the boron-epoxy insert.

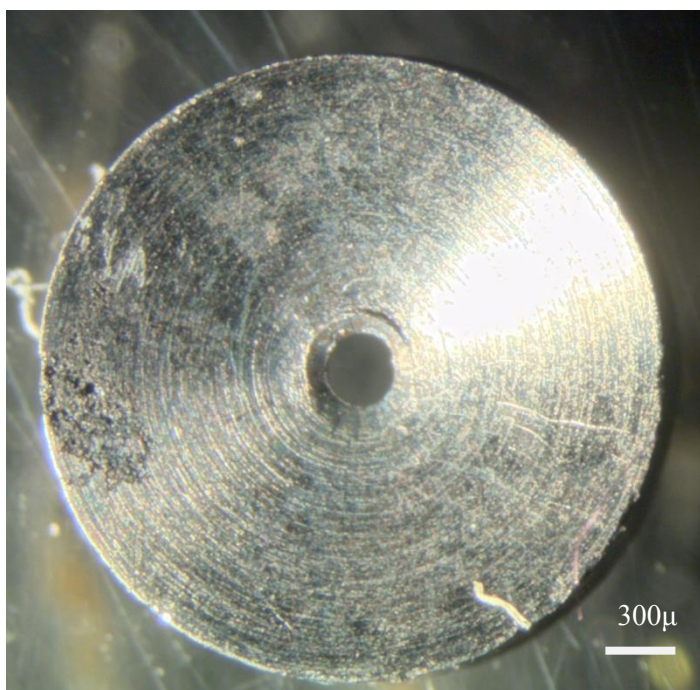


Figure 2.10 Be gasket with 300 μ hole size.

The boron-epoxy mixture was prepared by combining pure Boron powder and epoxy in a 3:2 ratio. For this experiment 1.446 g of boron powder was mixed with epoxy (approximately 0.461 g). Acetone was added in order to homogenize the mixture. The final weight of the boron-epoxy mixture was 1.908 g, which was very close to the calculated amount (1.907 g). The mixture was put into the furnace, pre-heated to 100°C and then cured for 24 hours.

The resulting material was ground into powder and prepared to be packed into the hole in the Be gasket. As it was previously stated, the size of the hole in the gasket exactly corresponded to the size of the diamonds in the DAC. In order to prepare the insert, the Be gasket was mounted directly on the culet of one of the diamonds of the DAC. To hold it still during the filling of the hole, small amount of clay was used (clay should have been removed right before the experiment to avoid unnecessary diffraction signal). The powdered boron-epoxy mixture was put into the

hole and then compressed up to 20 GPa using the DAC for three cycles. Before each compaction more material was added. This was done to make sure that mixture is well packed and also to obtain preindentation thickness of the gasket needed for the experiment. After the thickness reached about 50 μ , the gasket was left for 24 hours to harden at ambient conditions.

The last step of the gasket preparation was to drill (scratch) a hole in the boron-epoxy insert of the Be gasket. The hole was prepared using a simple metal needle. Hole size depended on the size of the insert and the culet size of the diamond in the DAC. For 300- μ m culet size diamond the hole size was not more than 50 μ m, whereas for 500 μ it is suggested as 80 μ m (Figure 2.11).

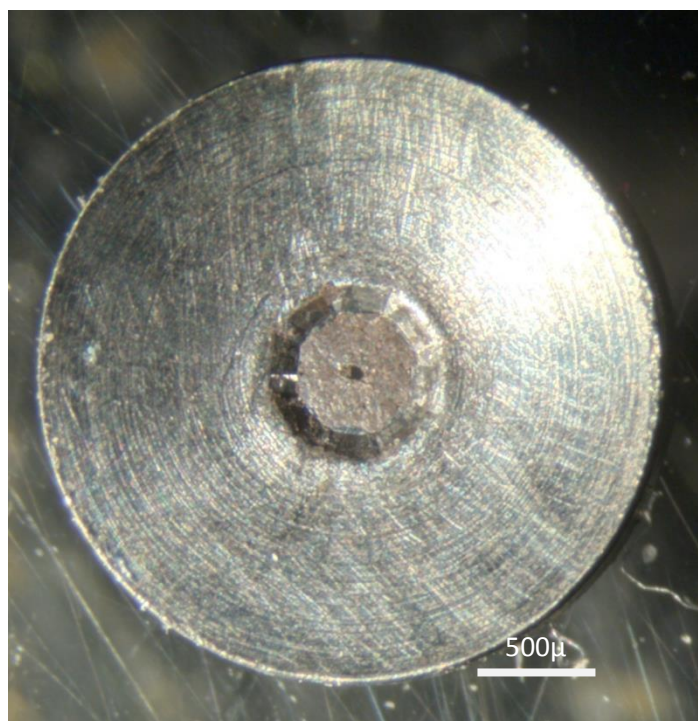


Figure 2.11 Be gasket (grey) with the 80 μ hole in B-epoxy insert (brown circle). B-insert size is 500 μ .

2.3.3. Sample loading for diffraction experiment

As the sample for the experiment, zircon powder from MP Biomedicals was used (Figure 2.12). According to MSDS (Material Safety Data Sheet), the sample had a chemical formula

ZrSiO_4 and purity more than 98%. Its detailed chemical composition was: ZrO_2 : 66.09%, SiO_2 : 32.27%, Ti: 0.07%, Al: 0.17%, Fe: 0.02%. Its molecular weight was 183.3036, melting point $> 280^\circ\text{C}$. The material was not toxic, but could only cause skin irritation or dermatitis, so it was possible to use it in our laboratory conditions without any danger to health.

Prior to packing the sample into the hole in the gasket, the sample was ground into very fine (close to homogeneous) powder in an agate mortar with acetone. This procedure was done to reduce the possibility of obtaining a dotted structure in the diffraction rings.



Figure 2.12 Zircon (IV) silicate powder. A- powder sample and Be gaskets. B- sample in original package.

After grinding the zircon powder in a mortar, the next step was to pack the sample into the hole in the gasket. The gasket was mounted on the top of the diamond culet in the piston part of the DAC. The hole should appear exactly in the centre of the culet, as this is critical for the experiment. The gasket also should not have been tilted in any direction. A tiny piece of golden foil was put exactly on the top of the diamond's culet of the cylinder part of the DAC. The size of the foil piece was around $20\ \mu\text{m}$ and it was used as a pressure marker during the experiment. The foil was prepared after compression of the powdered sample between two diamond culets in the mini DAC (Figure 2.13). Only dark part of the foil was eligible for the experiment (Figure 2.14).

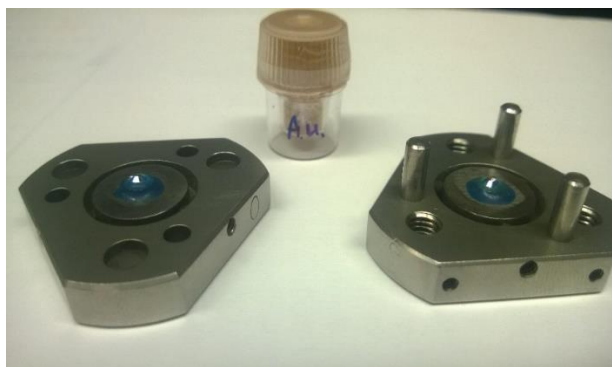


Figure 2.13 Mini DAC, cylinder (to the left) and piston (to the right) to the bottle with powdered nano-gold which was used in the experiment.

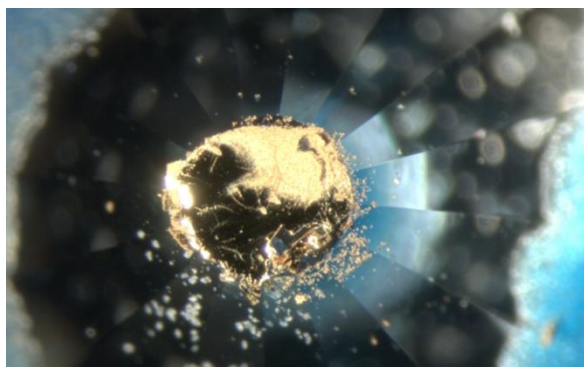


Figure 2.14 Gold foil formed on the top of the diamond's culet of the mini DAC. Dark part was used in the experiment.

After the gold foil was mounted, the cell was closed. As is visible in Figure 2.15, foil appears to be in the center of the hole, filled with the sample.

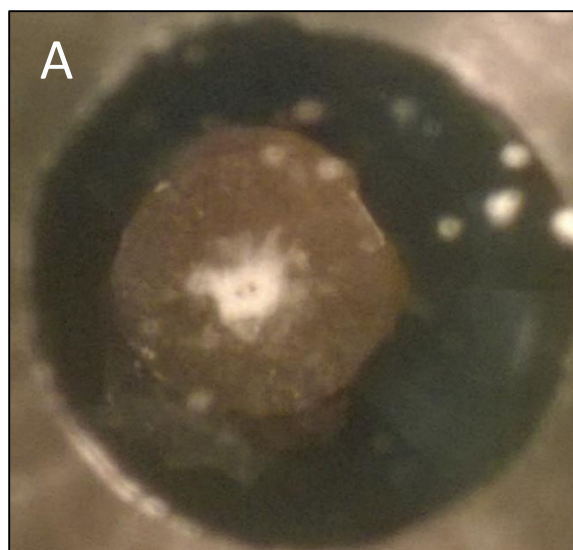


Figure 2.15 Be gasket before (a) and after (b) compression. Be+B-epoxy gasket with the hole filled with zircon. A piece of golden foil is situated in the center of a culet. Grey colored part is Be gasket; brown- boron insert; white- zircon sample and dark black with golden sides- gold foil.

2.4. Synchrotron x-ray diffraction experiment

As mentioned earlier, diffraction patterns were collected at the beamline X17C at National Synchrotron Light Source, Brookhaven National Laboratory, NY. The angle-dispersive X-ray diffraction technique with prevalence of radial x-ray diffraction was used as a main method for this experiment. The synchrotron source had a fixed beam wavelength, which was 0.4112 Å during our first experiment and 0.4099 Å during our second run. Beam size was focused to 20x23 μm^2 and a MAR CCD detector was used for X-ray diffraction pattern collections.

The calibration of the detector was done by collecting the CeO_2 diffraction patterns. Cerium oxide is a well-known standard and certified by the American National Institute of Standard and Technology, and is commonly used in X-ray diffraction experiments. By reducing the 2D diffraction images of the standard into 1D diffraction curve using the fit2d program, we obtained the required parameters of detector calibration (Tables 2.1 and 2.2).

Table 2.1 Instrumental calibration parameters, NSLS, March 2014.

The screenshot shows a window titled "FIT2D GRAPHICS WINDOW" with a sub-header "EXPERIMENTAL GEOMETRY" and "CONTROL FORM". Below the header are five buttons: O.K., CANCEL, ?, HELP, and INFO. The main area is a table with three columns: DESCRIPTIONS, VALUES, and CHANGE. The table contains the following data:

DESCRIPTIONS	VALUES	CHANGE
SIZE OF HORIZONTAL PIXELS (MICRONS)	79.59000	X-PIXEL SIZE
SIZE OF VERTICAL PIXELS (MICRONS)	79.59000	Y-PIXEL SIZE
SAMPLE TO DETECTOR DISTANCE (MM)	286.9201	DISTANCE
WAVELENGTH (ANGSTROMS)	0.411200	WAVELENGTH
X-PIXEL COORDINATE OF DIRECT BEAM	269.3257	X-BEAM CENTRE
Y-PIXEL COORDINATE OF DIRECT BEAM	955.4534	Y-BEAM CENTRE
ROTATION ANGLE OF TILTING PLANE (DEGREES)	-111.4708	TILT ROTATION
ANGLE OF DETECTOR TILT IN PLANE (DEGREES)	-0.317271	ANGLE OF TILT

At the bottom of the window, there is a text box that says "Click on variable to change, or 'O.K.'"

Table 2.2 Instrumental calibration parameters, NSLS, June 2014.

The screenshot shows a window titled "Light Graphics Window" with a sub-header "EXPERIMENTAL GEOMETRY" and "CONTROL FORM". Below the header are five buttons: O.K., CANCEL, ?, HELP, and INFO. The main area is a table with three columns: DESCRIPTIONS, VALUES, and CHANGE. The table contains the following data:

DESCRIPTIONS	VALUES	CHANGE
SIZE OF HORIZONTAL PIXELS (MICRONS)	79.59000	X-PIXEL SIZE
SIZE OF VERTICAL PIXELS (MICRONS)	79.59000	Y-PIXEL SIZE
SAMPLE TO DETECTOR DISTANCE (MM)	286.6526	DISTANCE
WAVELENGTH (ANGSTROMS)	0.409929	WAVELENGTH
X-PIXEL COORDINATE OF DIRECT BEAM	269.1343	X-BEAM CENTRE
Y-PIXEL COORDINATE OF DIRECT BEAM	955.1898	Y-BEAM CENTRE
ROTATION ANGLE OF TILTING PLANE (DEGREES)	-122.0932	TILT ROTATION
ANGLE OF DETECTOR TILT IN PLANE (DEGREES)	-0.449691	ANGLE OF TILT

At the bottom of the window, there is a text box that says "Click on variable to change, or 'O.K.'"

After calibration was done, the DAC with the sample inside was mounted onto the sample holder. The cell should be perfectly aligned according to the centre of rotation under the microscope. Using a microscope attached to the X17C high pressure system, diamond thickness correction was made via the application of refractive index of diamond. The final step before the collection of patterns was the scanning of the sample with photodiode (Figures 2.16 and 2.17). The location of the dimple shows the position of the sample and the gold flake. As it is clear, the position of the “dimple” is very close to the centre, which was the initial purpose of the loading.

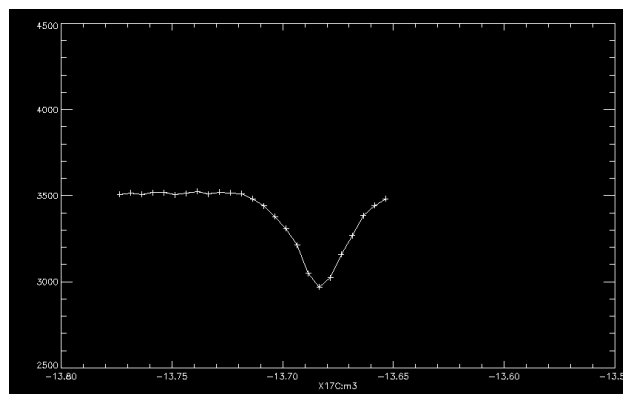


Figure 2.16 Photodiode scanning image along vertical direction (m3) at ambient conditions. The dimple shows the location of zircon + gold position.

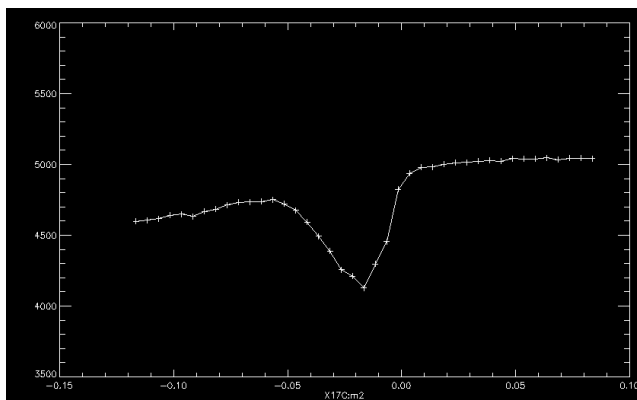


Figure 2.17 Photodiode scanning image along horizontal direction (m2) at 21 GPa. The dimple shows the location of zircon + gold position.

2.5. EBSD experiment using SEM

Electron Backscatter Diffraction (EBSD) Analysis is a method used to perform quantitative microstructure analysis of the crystallographic nature of minerals, metals, ceramics and semiconductors in the Scanning Electron Microscope (SEM) (Maitland and Sitzman, 2007). It allows us to make microstructural-crystallographic analyses in order to measure the crystallographic orientations in crystalline material (Kovaleva and Klotzli, 2013). Using this method, samples with mm up to several nm grain size can be analyzed. The EBSD is based on the idea that accelerated electrons can be diffracted by atomic layers in crystalline materials. Basically, the method is produced by incoherent wide-angle scattering of a stationary beam of high electrons from a virtual volume of crystal (Schwarzer 2015). By using crystallographic structure information, one can transform information and perform fabric analyses, identify phases, detect crystal orientation, grain size, texture (global and local), and make strain analysis etc. Moreover, EBSD mapping is supposed to be able to constrain potential diffusion pathways in minerals. It can indicate areas of damaged crystalline structure, help to examine substructures of minerals used in radiometric dating and assess the potential for resetting of ages by deformation events (Moser *et al.*, 2009, Reddy *et al.*, 2007, Kovaleva and Klotzli, 2013).

This method was first performed in 1928 by Shoji Nishikawa and Seishi Kikuchi (this is the reason why it is often called *backscatter Kikuchi diffraction* - BKD).

Basic principles of EBSD. This method is based on the interaction of well-polished sample and electrons with high energy. The sample is placed in the SEM with an angle relative to the normal of the electron beam (typically 70 degrees). With an accelerating voltage of 1-30 keV and incident beam currents up to 50 nA, electron diffraction occurs from the incident beam point on the surface of the sample (Maitland and Sitzman 2007). The detector (camera with phosphor screen) is mounted horizontally on a motorized carriage close to the surface of the sample. If the surface of the sample is well polished and has no defects, electrons that leave the sample are backscattered according to Bragg's law and are collected at the phosphor screen (Mariani *et al.*, 2009). In a situation when different lattice planes diffract different electrons Kikuchi bands are formed and the EBSD pattern is formed. Using Miller indices one can identify each plane.

Nowadays EBSD is considered to be the best method for acquiring data for crystalline structure, texture and orientation in a solid. Using this technique, a wide variety of materials, including isotropic and opaque phases can be analyzed with ability to obtain 3D patterns. However, though this method can provide us with high resolution pictures up to several microns, it has some limitations. Special sample preparation is required: samples should be not damaged and be well polished. There are some problems with resolution and quality in nonconductive materials analysis (conductive coating is required for the EBSD, but not desirable for materials-insulators). Problems with coating are usually solved by using carbon coating. Also there is a correlation between resolution and sharp EBSPs (resolution is reduced if one analyzed larger spots in order to get a sharper EBSP) (Mariani *et al.*, 2009). Data acquired by EBSD should be analyzed by appropriate software, which is proposed by Oxford Instruments HKL and TSL Crystallography (Schwarzer 2015).

2.5.1. SEM sample preparation

Quenched samples from the previous high pressure experiments were further analyzed by Scanning Electron Microscope (SEM). Sample preparation for analysis required three steps: 1) removal of the sample from the gasket, 2) mounting of the sample into epoxy glue (making epoxy plug) and 3) hand polishing the sample using lapping films and colloidal alumina mixture.

The zircon sample was removed from the gasket with the help of a needle of appropriate size and diameter. The idea was to separate the B-epoxy insert from the Be gasket. Later, the sample was mounted on a double-sided steel plate with aluminum foil previously put on the surface. A blue teflon ring was used as a mount holder. This holder was fully filled with epoxy resin (5.0g of Buehler Epoxicure resin and 1.0g of Buehler Epoxicure hardener (or 0.6g of Struers hardener) and was put into the pre-heated furnace at 20 degrees C for five minutes. The process of mixing the epoxy and filling the ring should be done very slowly in order to avoid bubbling. After heating the sample in the oven it was left overnight and later heated for another four hours at 50 °C. After removal of the epoxy mount, the sample was cleaned with ethanol. The back face of the epoxy plug was flattened with a 600 grit sandpaper (Figure 2.18 – 2.19).

After the epoxy plug was prepared, the sample was polished using two types of sand papers and VibroMet2 to prepare the sample for the SEM experiment. Polishing with 9 and 6 microns film allowed us to expose the sample. VibroMet2 finished polishing (three hours) removed the main scratches and prepared the surface for the EBSD (Figures 2.20 and 2.21). After each polishing step, the sample was cleaned with acetone and DI water several times to avoid extra scratches by the material itself. Finally the sample was coated with carbon (Barker 2014).

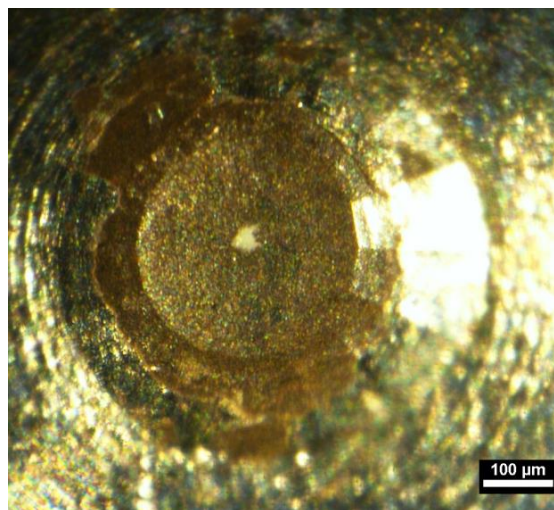


Figure 2.18 Quenched sample (#3) at 30 GPa before removal from the gasket. Brown color- B-epoxy mixture, zircon sample is white coloured part in the middle of the gasket.

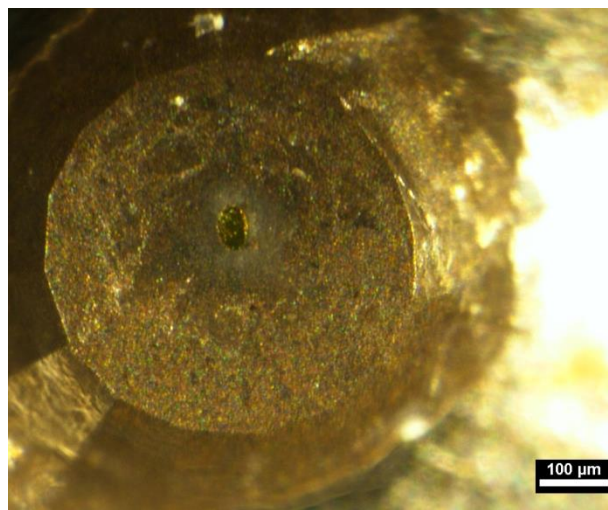


Figure 2.19 Quenched sample (#1) at 20 GPa before removal from the gasket. Brown color- B-epoxy mixture, zircon sample is white coloured part in the middle of the gasket; gold flake is on the top of the sample.

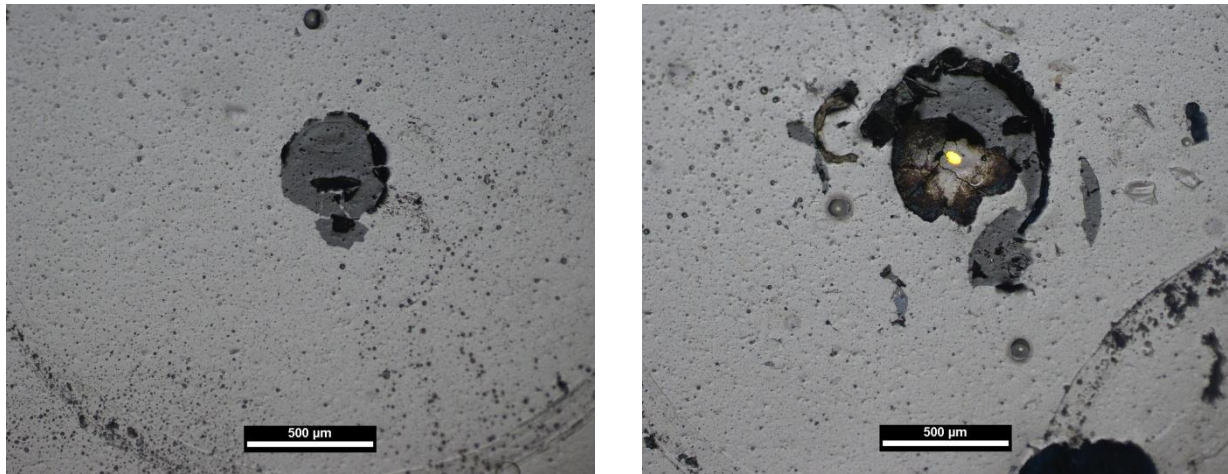


Figure 2.20 B-epoxy insert with zircon sample (#3 – left; #1 – right) mounted into epoxy before polishing in reflected light.

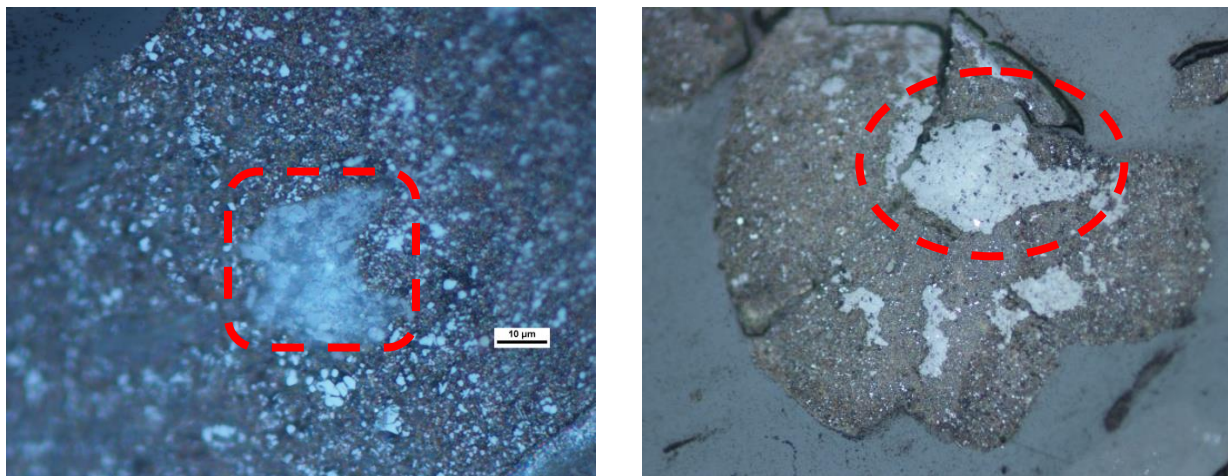


Figure 2.21 Sample #3 (left) and #1 (right) after 3 steps of polishing: 1) polishing with blue sand paper (9 microns); 2) with pink sand paper (6 microns); 3) with 0.05 microns grain size Bohler MasterPrep colloidal alumina mixture on VibroMet2. Analyzed region is marked with red color.

2.6. Data analysis. Instrumentation

Diffraction patterns were analysed by the fit2d software using calibration parameters recorded during each run at NSLS. Using information of wavelengths, the sample to detector distance and other important parameters from calibration files (Figures 2.17-2.18) diffraction patterns were sliced into 37 files with a 5-degree step. This action was required for further analysis of stress. All 37 files were recorded to be analysed by the PeakFit program. The PeakFit program allows one to collect information about the position (center) and peak width at half maxima (FWHM). The center of each peak corresponds to a 2θ angle of the sample. Applying Bragg's law ($\lambda = 2d\sin\theta$, $d = \frac{\lambda}{2\sin\theta}$, Figure 2.22) one can obtain d -spacings for every diffraction pattern. Following the theory proposed by Singh (see Theory), linear relations of d -spacing as a function of $1-3\cos^2\psi$ were plotted using the IgorPRO software. The same program was also used to plot the equation of state of zircon at different ψ angles (i.e., 0° , 54.7° and 90°) and for the calculation of the bulk modulus. Texture analysis was performed by MAUD software (Lutterotti *et al.*, 1997, 1999, 2004, 2007, Lutterotti 2010). Initial files were converted into the required format by fit2dmaud.

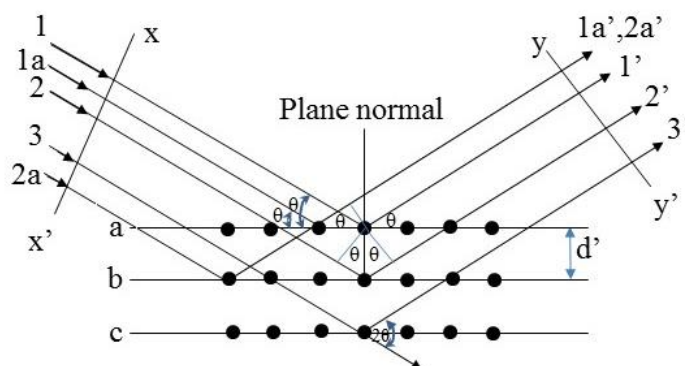


Figure 2.22 Schematic plot of the Bragg's Law.

2.6.1. Reitveld refinement and texture analysis

The X-ray diffraction images were analyzed with the Rietveld method using MAUD software (Lutterotti *et al.*, 1997, 1999, 2004, 2007, Lutterotti 2010). This software allows us to refine structural, instrumental, microstructural and textural parameters of diffraction data. The diffraction image was analyzed and sliced into 36 spectra with a 5-degree azimuthal angle step

using fit2dmaud software. Later, the obtained 36 files were converted to *esg* format with the fit2dmaud program (as *esg* is one of two acceptable formats in MAUD).

3. LATTICE STRAIN THEORY

The compression of a solid sample between two parallel faces of anvils without any pressure medium is subject to nonhydrostatic condition that results in lattice strains. The theory of lattice strains applied to diamond-anvil cell study was developed by Singh (1993). It was developed for cubic and hexagonal symmetries. Later this lattice strain theory was applied to the study of a tetragonal system in stishovite (Shieh *et al.*, 2002). Singh's lattice strain theory was supported and discussed in numerous publications and studies (Duffy *et al.*, 1999, Duffy and Heinz 1999, Merkel *et al.*, 2002, Raterron *et al.*, 2013, Shieh *et al.*, 2002), though there were some opponents that considered the theory applicable only to the samples that were not plastically deformed (Weidner *et al.*, 2004).

Under compression, maximum stress is located in the center of the diamond-anvil cell. From elasticity theory for single crystals, stress in a DAC sample chamber can be described by

$$\sigma_{ij} = \begin{pmatrix} \sigma_1 & 0 & 0 \\ 0 & \sigma_2 & 0 \\ 0 & 0 & \sigma_3 \end{pmatrix}, \quad (3.1)$$

where $\sigma_1 = \sigma_2$ and are radial stress components and σ_3 is an axial stress component (along the diamond cell axis) and σ_{ij} is a stress tensor (Singh 1993). Maximum shear stress (von Mises yield criterion) leads to

$$t = (\sigma_3 - \sigma_1) \leq 2\tau = Y, \quad (3.2)$$

where τ (Pa) is a shear strength and Y (Pa) is the yield strength of the material. Supported differential stress is considered the lowest bound to yield strength (Shieh *et al.*, 2002, Singh 1998).

Equivalent hydrostatic pressure (mean normal stress) is given by

$$\sigma_p = \frac{(\sigma_1 + \sigma_1 + \sigma_3)}{3} = \sigma_1 + \frac{t}{3} \quad (3.3)$$

This stress tensor can be described by a combination of mean normal stress and deviatoric stress:

$$\sigma_{ij} = \begin{pmatrix} \sigma_p & 0 & 0 \\ 0 & \sigma_p & 0 \\ 0 & 0 & \sigma_p \end{pmatrix} + \begin{pmatrix} \frac{-t}{3} & 0 & 0 \\ 0 & \frac{-t}{3} & 0 \\ 0 & 0 & \frac{2t}{3} \end{pmatrix} = \sigma_p + d_{ij} \quad (3.4)$$

σ_p is a mean normal stress (Figure 3.1). The second term in the equation corresponds to deviatoric stress tensor d_{ij} (Duffy *et al.*, 1999, Merkel *et al.*, 2002).

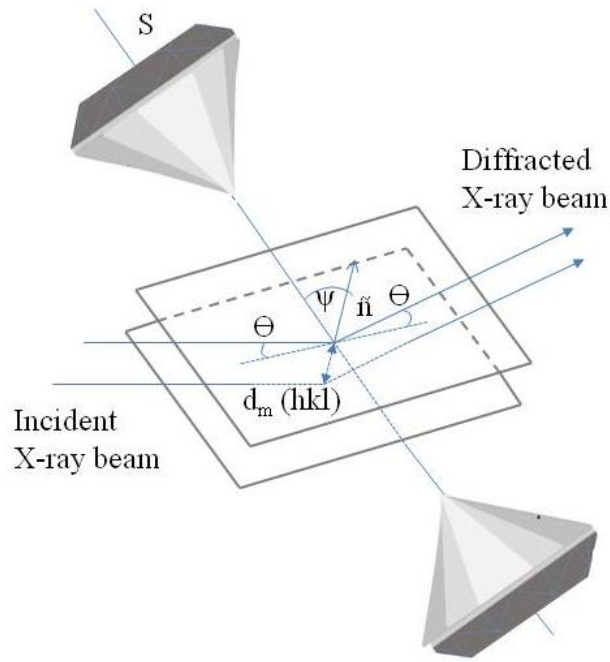


Figure 3.1 Geometry for a given ψ angle between the diffracting plane normal \hat{n} and the maximum stress axis S , $d_m(hkl)$ is a measured d-spacing function of the Miller indices h , k , and l . When $\psi = 0^\circ$, the diffracting plane is orthogonal with the maximum stress axis S , thus $d_m(hkl)$ is minimum. When $\psi = 90^\circ$, the diffracting plane is aligned with the maximum stress axis S , thus $d_m(hkl)$ is maximum (Merkel *et al.*, 2002).

In terms of interplanar distances, deviatoric component can be expressed by

$$\epsilon_d = \frac{[d_m(hkl) - d_p(hkl)]}{d_p(hkl)}, \quad (3.5)$$

where $d_m(hkl)$ is the measured interplanar d -spacings for the lattice plane (hkl) under stress conditions (σ_{ij}) and $d_p(hkl)$ is the d -spacings under hydrostatic stress (σ_p) (Mao *et al.*, 1998).

Measures of d -spacings as a function of ψ angle, which is the angle between the principal stress angle and the diffracting plane normal, are expressed by:

$$d_m(hkl) = d_p(hkl)[1 + (1 - 3\cos^2\psi)Q(hkl)] \quad (3.6)$$

where $Q(hkl)$ is given by

$$Q(hkl) = \frac{t}{3} \left\{ \frac{\alpha}{2G_R(hkl)} + \frac{1-\alpha}{2G_V} \right\}. \quad (3.7)$$

G_R and G_V are the shear modulus under Reuss (iso-stress) and Voigt (iso-strain) limits, respectively. A degree of stress-strain continuity across grain boundaries is defined as α parameter and it usually lies between 0 and 1 (Duffy *et al.* 1999).

According to the theory $d_m(hkl)$ has a linear relation with $1-3\cos^2\psi$. The intercept of the relation (at $\psi=54.7^\circ$ or $1-3\cos^2\psi=0$) gives the d -spacing to the hydrostatic component of the stress, where there is no contribution of deviatoric stress to the measured d -spacing (Duffy *et al.*, 1999). The slope of $d_m(hkl)$ vs $1-3\cos^2\psi$ yields the product of $d_p(hkl)$ $Q(hkl)$ (Duffy *et al.*, 1999, Merkel *et al.*, 2002, Shieh *et al.*, 2002,)

Assuming Reuss (homogeneous stress) conditions inside the DAC ($\alpha = 1$)

$$t = 6G_R \langle Q(hkl) \rangle, \quad (3.8)$$

where $\langle Q(hkl) \rangle$ is an average value of all observed reflections.

4. RESULTS AND DISCUSSION

4.1. Strength of zircon based on lattice strain theory

This high pressure radial x-ray diffraction experiment was performed on zircon powder up to 32 GPa. Three datasets were collected at pressure up to 20, 32 and 33 GPa, respectively. Diffraction patterns were collected at a radial geometry with the pressure step of 1 GPa. Obtained 2D image data were transformed into 1D patterns using *fit2d* program and later was analyzed by *PeakFit* software. Two-theta angle values and full width at half maximum (FWHM) along with the intensity were derived from PeakFit software. Two-theta angles were used to get the *d*-spacing of each (*hkl*) plane with different diffraction angle (ψ) at each pressure step using Bragg's law:

$$d = \frac{n\lambda}{2\sin\theta}, \quad (4.1)$$

where n is an integer, λ is the wavelength ($\lambda=0.4112 \text{ \AA}$ for 1st and 2nd run and $\lambda=0.4099 \text{ \AA}$ for the 3rd run), d is the interplanar spacing in lattice, θ is the angle between the incident X-ray and the scattering planes.

The observed diffraction pattern contained peaks which corresponded to crystallographic planes of zircon, gold, reidite, Be and BeO. In this study 101, 200, 211, 112, 031, 312 and 213 planes of zircon; 111, 200 and 220 of Au and 112 of reidite were observed and used for data processing. Au 111, 200 and 220 were used to determine the pressure. The pressure gradient was negligible due to the configuration of the sample chamber. The curvative shape of the diffraction lines was caused by stress and the deformation of the sample (Figure 4.1). By compiling all the spectra together, the variations of *d*-spacings as well as peak shift can be clearly observed (Figure 4.2).

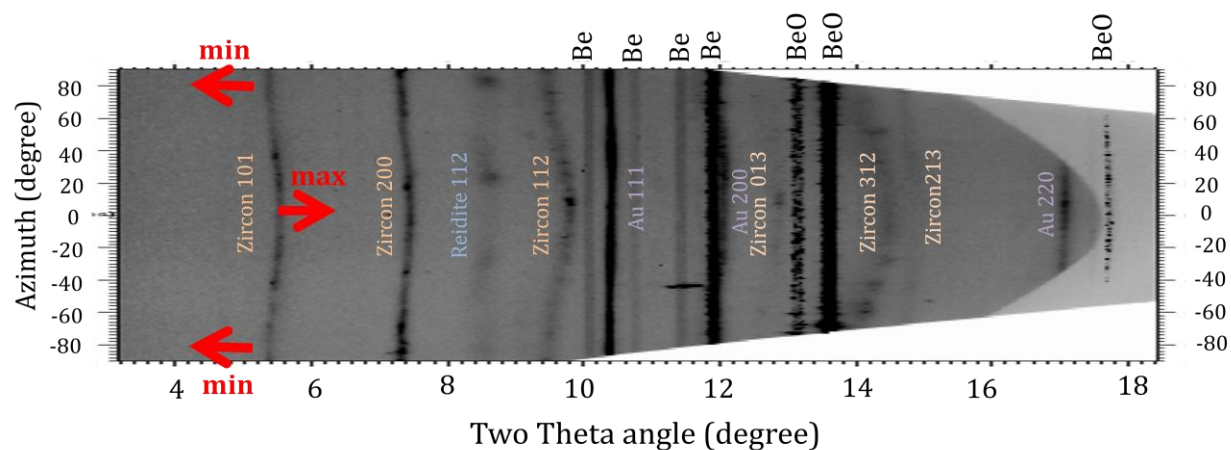


Figure 4.1 Representative sliced with 5° XRD image in 2D format converted using fi2d software at $P = 27.7$ GPa. Sample (zircon and reidite), pressure standard (Au) and gasket (Be, BeO) are marked accordingly. Maximum ($\psi = 0^\circ$) and minimum ($\psi = 90^\circ$) stress directions are shown by red arrows.

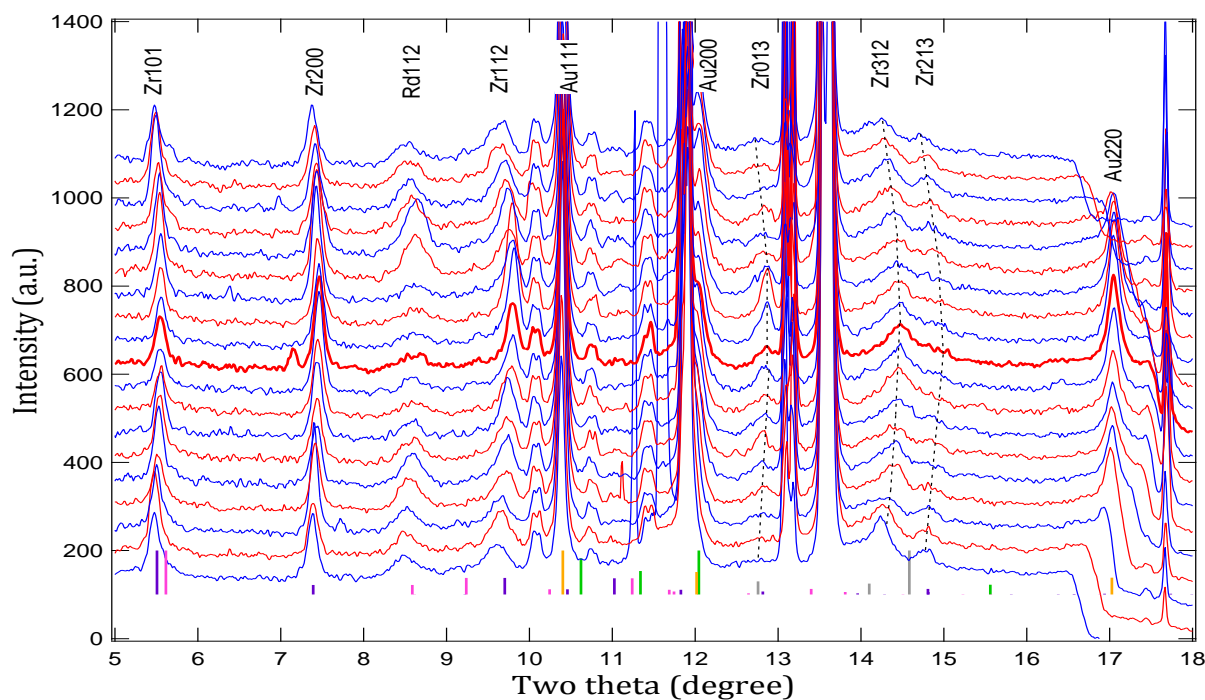


Figure 4.2 Representative ADXD diffraction pattern of zircon taken at $P = 27.7$ GPa. Bold red line represents maximum stress ($\psi = 0^\circ$). Sample's and pressure marker's planes are labelled on the top of the figure. At the bottom of the figure purple markers - zircon; pink -

reidite; yellow- Au; green- Be; grey- BeO. Black dashed lines are guide to the eye for stress development in zircon.

Under high pressure, zircon, a tetragonal phase ($I4_1/amd$ at ambient conditions) undergoes phase transition to reidite ($I4_1/a$), a scheelite structure. At 18.6 GPa additional peaks were observed, which indicated the occurrence of the new phase and the position corresponds to reidite 112 (Figure 4.3). The intensity was relatively low, but became stronger with pressure increase (up to 33 GPa). Phase transition to reidite was also proven by Raman spectroscopy, although Raman modes of reidite during the experiment were observed at slightly higher pressure (19.02 GPa). At 22 GPa, reidite developed only in the centre of the sample chamber, suggesting that the transition is very slow and maybe due to kinetics (see Raman, section 4.4). At the edges, where the stress was lower, zircon was the only existing phase. Nevertheless, this occurrence of reidite is interesting as it is the lowest recorded phase transition reported at ambient temperature. Note that the sample chamber of this Raman study has a large size compared to that of X-ray diffraction in a radial geometry. Knittle and Williams (1993) detected transition to reidite in natural zircon at 23 ± 1 GPa. Slightly lower transition pressure was reported for trace-element doped zircon 22.5 GPa (van Westrenen *et al.*, 2003). This discrepancy could have been caused by the impurity of the zircon (composition of starting material). The lowest previous pressure (and the closest to our results) was reported in 2004 by van Westrenen *et al.*, (2004). From van Westrenen's study, a 112 peak of reidite was detected at 19.66 ± 0.03 GPa.

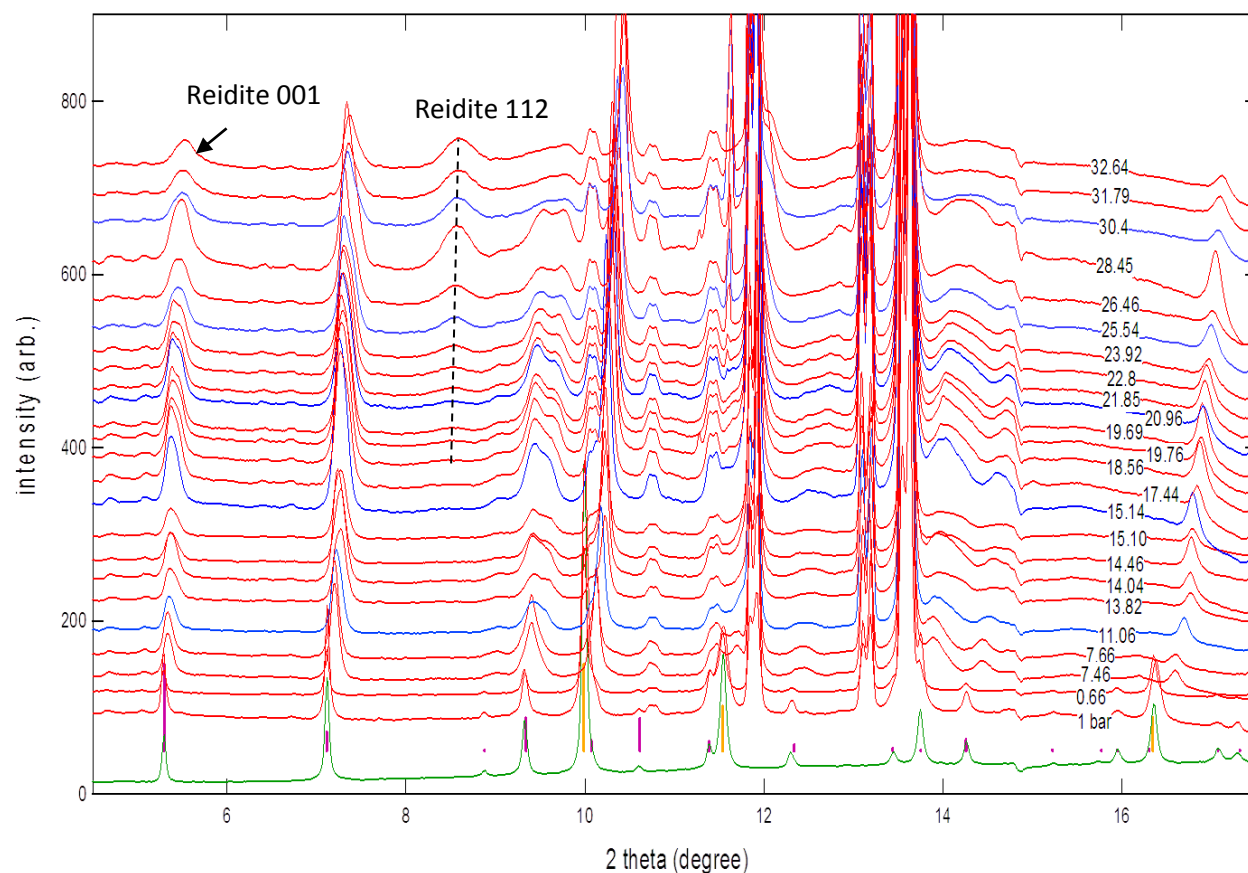


Figure 4.3 Diffraction patterns of zircon observed at different pressures using ADXD. Purple markers on the bottom of the figure correspond to zircon; yellow- Au. Black dashed line emphasizes reidite peak (reidite 112). Reidite 001 is shown by arrow.

The value of interplanar d -spacing depends on pressure (the greater the pressure, the smaller the d -spacing value) and ψ angle. A summarized plot of d -spacing distribution for each analysed crystallographic plane of powdered zircon is shown in Figure 4.4. A linear relation with gradually reduced d -spacing with increasing pressure can be considered a direct evidence of 1) all the d -spacings correspond to a certain crystallographic plane; 2) with increasing pressure the d -spacings become smaller due to the applied stress. Peaks 101, 200 and 112 are considered main planes and can be observed through the full pressure range. Peaks 211 and 213 are distinguished easily in a relatively low pressure range, though are overlapped with Be and BeO peaks at high pressure. This makes it impossible to locate the direct positions of those planes. The opposite situation is typical for 312. This plane is not clear at lower pressures, but becomes

clear starting at 18 GPa. Planes 112 and 312 experience the biggest change of d -spacing with pressure increase.

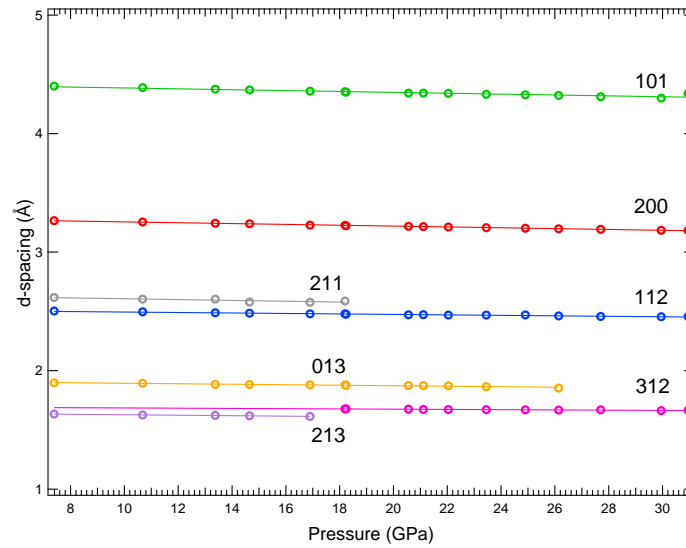


Figure 4.4 Variations of interplanar d -spacings of zircon with pressure (from 7 to 31 GPa).

The variation of d -spacings at the same pressure step is caused by the deviatoric stress, which has a sinusoidal relation along the ψ angle. Maximum stress occurs at $\psi = 0^\circ$ and minimum stress occurs at $\psi = 90^\circ$ (or -90°) (Figure 4.5). A partial deviation in linear distribution can be caused by the development of texture, shift of the sample off the centre of the anvil face (tilting of the gasket) or tilting of the anvils due to high pressure (Singh *et al.*, 2004).

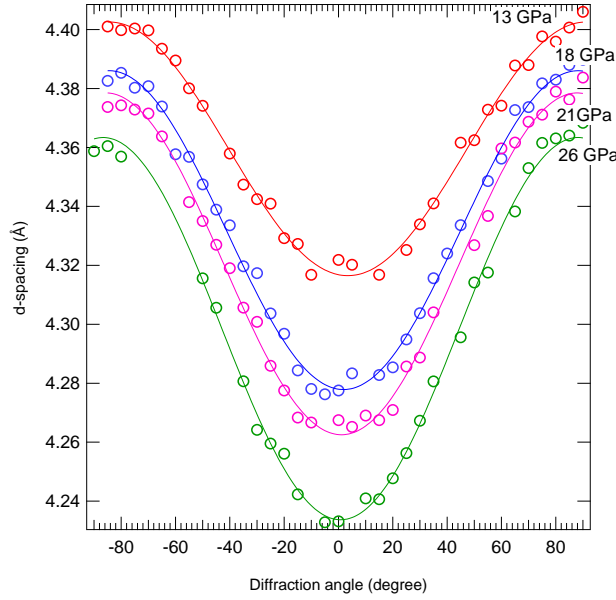


Figure 4.5 Plot of d -spacings as a function of diffraction angle for zircon (101) plane with different pressures. Hydrostatic pressure is labeled to the right of the sinusoidal curves. The d -spacing decreases with pressure. The largest values of d -spacings are observed around 90° and -90° .

Representative 2D image of zircon at $P = 27.7$ GPa, sliced into 19 diffraction patterns with 5° starting from -45° to 45° is shown on Figures 4.1 and 4.2.

According to lattice strain theory in order to obtain d -spacing for hydrostatic conditions at each pressure step it is necessary to create plots of observed d -spacings [$d_m(hkl)$] over $1-3\cos^2\psi$. An intercept at $1-3\cos^2\psi = 0$ will give the value at hydrostatic conditions. Variations of d -spacings over $1-3\cos^2\psi$ are shown in the Figures 4.6-4.9. Linear relation is observed for all the planes. The linear fit can be described by an equation $y = ax+b$, where a is the slope or $Q(hkl)$ and b is the d -spacing of the hydrostatic conditions. $Q(hkl)$ value can be directly derived from the slope. A steeper slope suggests the larger differential stress to shear modulus ratio. From this study it shows that (200) plane has the gentlest slope. The opposite situation is true with (112) and (312) planes that have the steepest slope (Figure 4.13). Maximum stress conditions correspond to $\psi = 0^\circ$ ($1-3\cos^2\psi = -2$), while minimum stress corresponds to $\psi = 90^\circ$ ($1-3\cos^2\psi = 1$). Hydrostatic conditions can be determined at $1-3\cos^2\psi = 0$, or $\psi = 54.7^\circ$ which is the pressure reported in this study, based on the equation of state of Au (i.e. Au 111, Au 200 and Au 220) (Fei *et al.*, 2007).

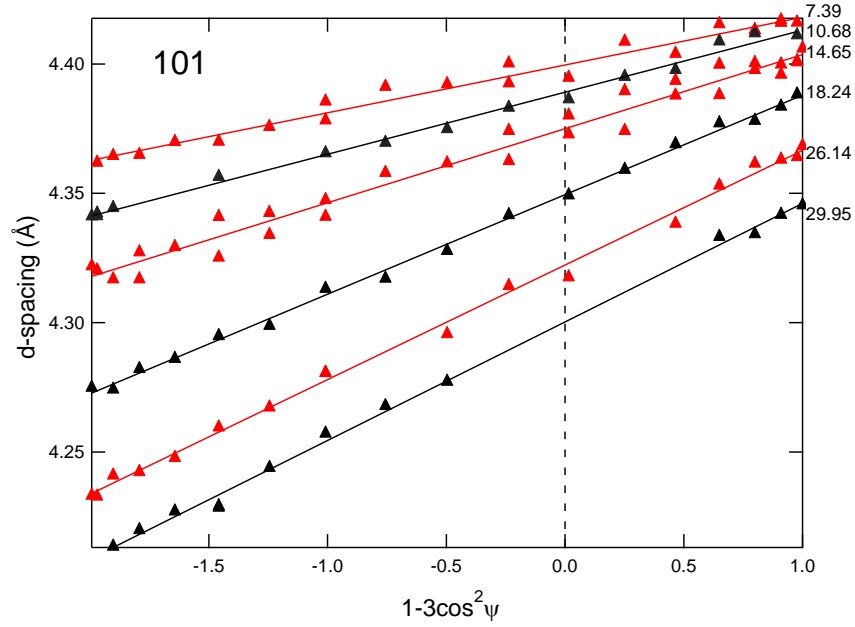


Figure 4.6 Variation of d -spacing as a function of $1-3\cos^2\psi$ for (101) diffraction line of zircon (3rd dataset) at different pressures. Solid lines represent linear fit to the measured d values. At $1-3\cos^2\psi = 0$ ($\psi = 54.7^\circ$) the measured interplanar distances are equal to hydrostatic conditions ($d_m = d_p$). Corresponding hydrostatic pressures obtained from equation of state of Au (Fei *et al.*, 2007) in GPa are shown on the right of the plot.

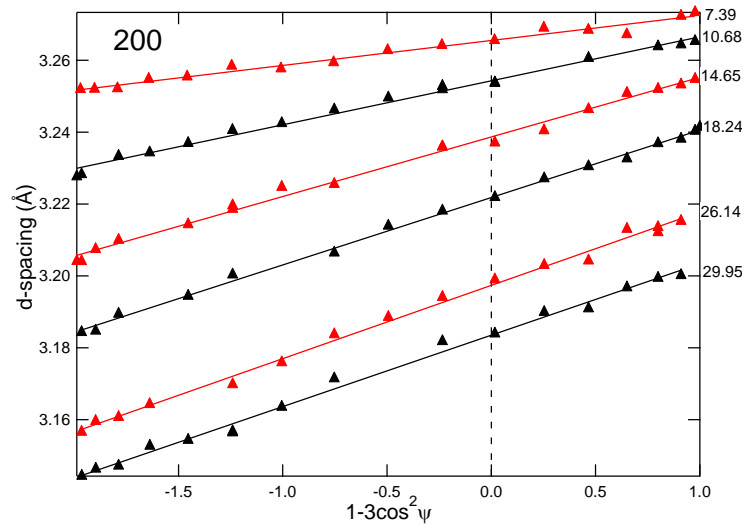


Figure 4.7 d -spacing as a function of $1-3\cos^2\psi$ for (200) diffraction line of zircon (3rd dataset) at different pressures. Solid lines represent linear fit to the measured values. At $1-3\cos^2\psi = 0$ ($\psi=54.7^\circ$) the measured interplanar distances are equal with those to

hydrostatic conditions ($d_m = d_p$). Corresponding hydrostatic pressures from Au equation of state (Fei *et al.*, 2007) in GPa are shown on the right of the plot.

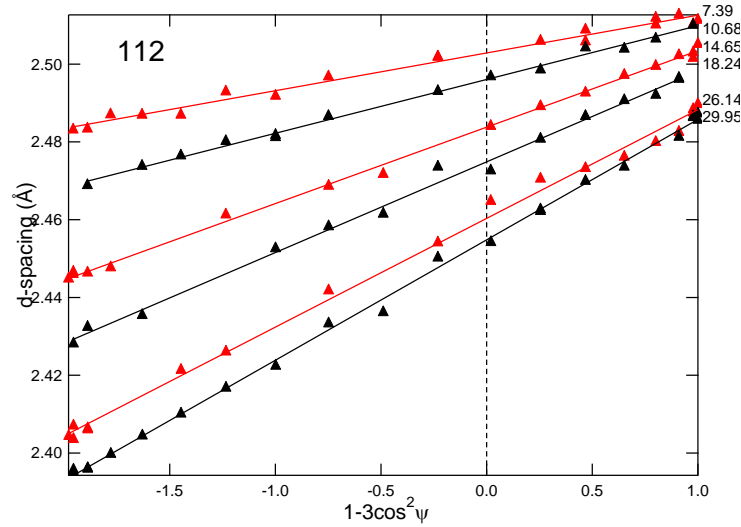


Figure 4.8 Variation of d-spacing as a function of $1-3\cos^2\psi$ for (112) diffraction line of zircon (3rd dataset) at different pressure. Solid lines represent linear fit to the measured values. Corresponding hydrostatic pressures from Au equation of state (Fei *et al.*, 2007) in GPa are shown on the right of the plot. At $1-3\cos^2\psi = 0$ ($\psi = 54.7^\circ$) the measured interplanar distances are equal with those to hydrostatic conditions ($d_m = d_p$).

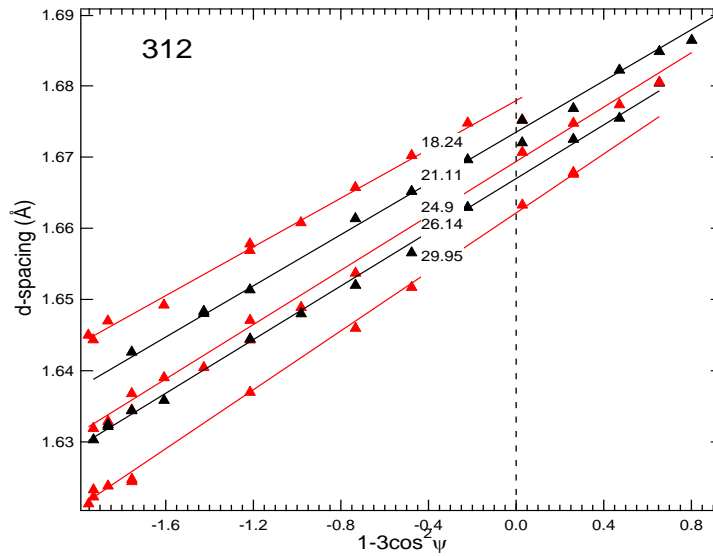


Figure 4.9 Variation of d-spacing as a function of $1-3\cos^2\psi$ for (312) diffraction line of zircon (3rd dataset) at different pressure. Solid lines represent linear fit to the measured

values. Corresponding hydrostatic pressures from Au equation of state (Fei *et al.*, 2007) in GPa are shown on the right of the plot. At $1-3\cos^2\psi = 0$ ($\psi = 54.7^\circ$) the measured interplanar distances are equal with those to hydrostatic conditions ($d_m = d_p$).

Shear modulus at ambient conditions obtained from Brillouin scattering for zircon has been reported elsewhere (Tkachenko *et al.*, 2007). Assuming Reuss (homogeneous stress) conditions inside the DAC, the ratio between differential stress and shear modulus can be obtained directly from the slope $Q(hkl)$ using the equation (3.7).

Table 4.3. Shear modulus and $Q(hkl)$ for each plane at different pressures.

Pressure, GPa	G _R , GPa	Q101	Q200	Q112	Q013	Q312	Q213
0	48	0	0	0			
1.17(1)	49.17	0.0013(2)	0.0012(2)	0.0006(2)			
3.89(4)	51.89	0.0022(3)	0.0016(3)	0.0025(4)			
4.25(2)	52.25	0.0022(4)	0.0024(5)	0.0027(3)			
6.43(6)	54.43	0.0037(4)	0.0024(5)	0.0045(3)			
7.39(7)	55.39	0.0039(2)	0.0024(1)	0.0052(2)	0.0035(2)		0.0019(1)
10.68(3)	58.68	0.0054(2)	0.0039(1)	0.0058(2)	0.0052(7)		0.0033(3)
13.38(4)	61.38	0.0065(2)	0.0046(1)	0.0066(3)	0.0055(4)		0.0058(3)
14.65(7)	62.65	0.0071(2)	0.0050(2)	0.0078(2)	0.0070(4)		0.0057(2)
14.95(7)	62.95	0.0070(4)	0.0049(3)	0.0079(4)			
15.6(1)	63.6	0.0082(4)	0.0053(2)	0.0091(3)			
16.9(1)	64.9	0.0077(2)	0.0058(2)	0.0088(2)	0.0068(4)		0.0060 (2)
17.4(2)	65.4	0.00934	0.0057(3)	0.0096(3)			

18.02(1)	66.02	0.0084(2)	0.0057(2)	0.0090(2)	0.0059(4)	0.0100(2)
18.7(1)	66.7	0.0089(2)	0.0058(2)	0.00933(3)	0.0077(9)	0.0102(4)
20.56(4)	68.56	0.0089(1)	0.0063(1)	0.0097(3)	0.0069(2)	0.0106(3)
21.11(1)	69.11	0.0090(2)	0.0063(1)	0.0098(3)	0.0080(4)	0.0108(3)
22.04(3)	70.04	0.0093(2)	0.0062(1)	0.0102(3)	0.008 (1)	0.0106(3)
23.45(1)	71.45	0.0097(2)	0.0062(5)	0.0093(3)	0.0066(9)	0.0108(3)
24.9(3)	72.9	0.0100(2)	0.0060(2)	0.0108(3)	0.028(4)	0.0114(3)
26.14(8)	74.14	0.0100(2)	0.0062(1)	0.0113(2)	0.0059(2)	0.0113(2)
27.7(3)	75.7	0.0098(2)	0.0063(1)	0.0115(3)		0.0133(3)
29.95(3)	77.95	0.0103(2)	0.0064(2)	0.0127(2)		0.0125(3)

The ratios between differential stress and shear modulus for each crystallographic plane are shown in Figure 4.10. Average value of t/G gradually increases to 0.05 (5%) before the phase transition pressure where reidite was detected. From that point, the t/G value increases slowly up to almost 0.08 (8%) in this study. This slope change can be largely caused by the behavior of the Zir (200) plane or the appearance of the reidite. As it is seen from the figure, the trend changes its behavior from steep to gentle slope. This can be regarded as typical for plastic deformation. The slope for Zir (101) is becoming gentler too. Though the slope steeply increases until about 26 GPa, it obtains horizontal distribution. Moreover, as there is no low pressure data for Zir (312) one can extrapolate it from the existing high pressure data. This extrapolated data show that the plane also has a trend of reduction in slope. This suggests mitigation of elastic deformation and the transition to the plastic region.

Moreover, obtained t/G values were compared to other mantle minerals such as olivine and ringwoodite (Figure 4.11). From the plot it clearly shows that zircon has relatively lower t/G values than both other mantle phases at pressure to 15 GPa.

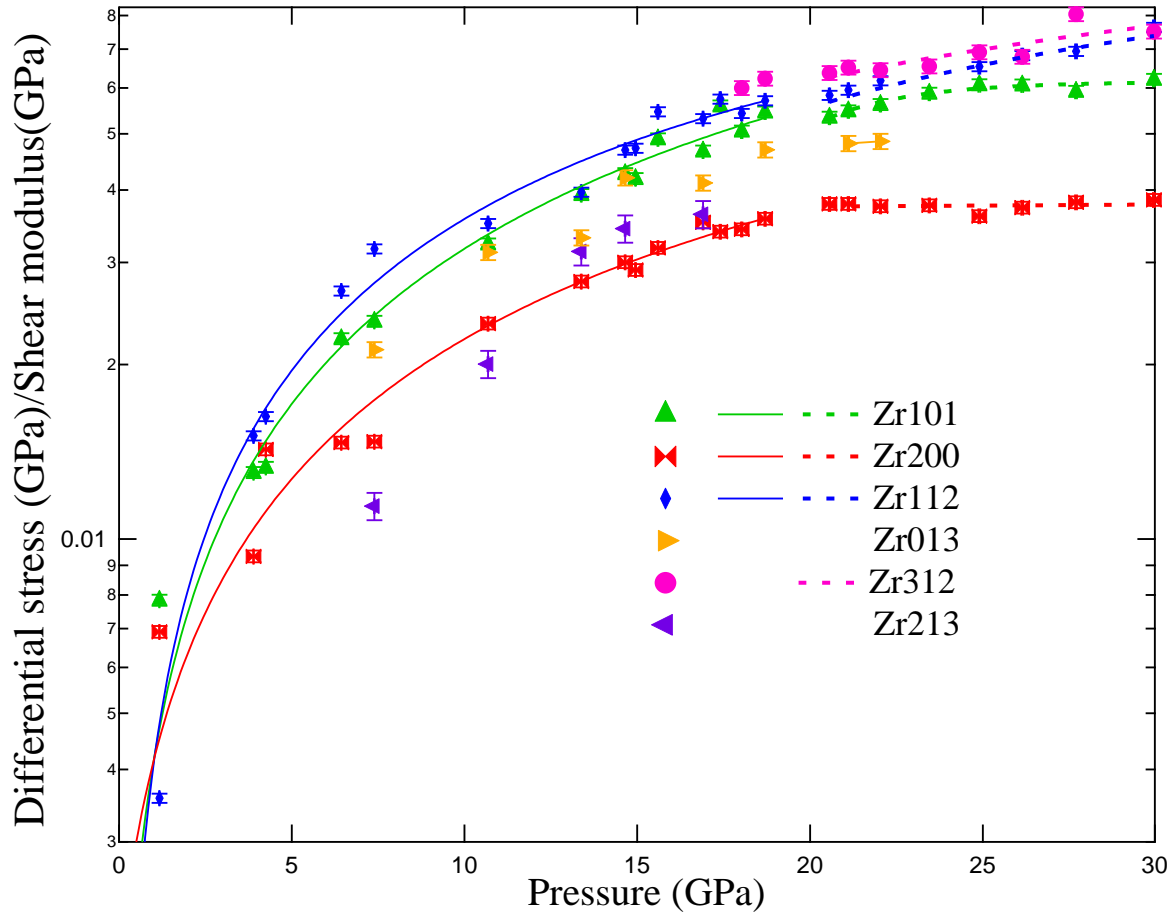


Figure 4.10 Ratios of differential stress to shear stress over pressure for zircon up to 30 GPa. Polynomial fit is applied to each plane to < 20 GPa. Solid line represents fit before phase transition (before reidite was observed), dashed line represents data after transition (both zircon and reidite phases are present).

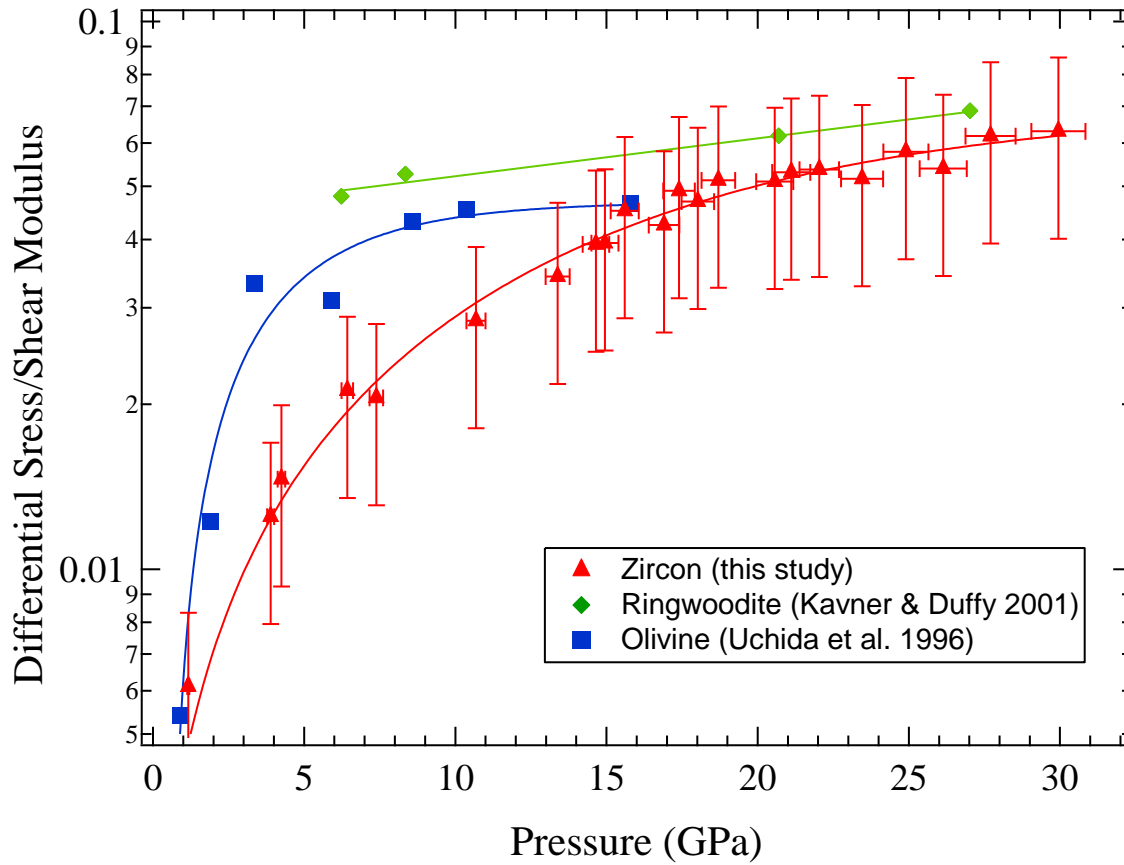


Figure 4.11 Differential stress/shear modulus ratio over pressure for different phasea up to 30 GPa: zircon (red triangles, this study), ringwoodite (green diamonds- Kavner and Duffy 2001); olivine (blue squares- Uchida *et al.*, 1996). Polynomial fits are applied.

The study of the differential stress supported by zircon shows that the material is very sensitive to stress. As it is seen from Figure 4.12, weak differential stress is already observed at as low as 1 GPa for all the planes, and gradually increases up to around 18 GPa where phase transition to reidite was first detected. At that point average differential stress is around 2.6 GPa. Phase transition pressure is also remarkable because of the small jump (0.5 GPa) in differential stress. After that zone differential stress comes back to its initial behavior and reaches as high as 4.5 GPa at a pressure around 30 GPa.

Average differential stress includes the contributions of all the crystallographic planes of the material. In this study, seven lattice planes (101, 200, 211, 112, 013, 312, 213) were analysed for their differential stress. From differential stress analysis, it showed that Zir (200) is the weakest plane. Differential stress increases up to 2.4 GPa until phase transition pressure (for Zir

(200)), when the plane undergoes plastic deformation (that is visible from the linear horizontal fit). On the contrary, Zir (112) is the strongest plane. At as low as 4 GPa, the differential stress of Zir (112) has already exceeded that of Zir (200) by 0.5 GPa. At 18 GPa, the difference was already more than 2 GPa. Maximum differential stress (5.4 GPa) was observed at 30 GPa. The distribution of Zir (312) plane data points suggests that its behaviour is similar to Zir (112). The absence of low pressure information for this plane prevents us from making clear conclusions about its quality. However, the existing data of Zir (312) suggest that it is the strongest plane for the studied pressure range. Before transition pressure the difference between Zir (312) and Zir (112) was around 0.5 GPa. But after reidite was detected, the Zir (312) plane changed its behavior. The sharpness of the slope decreases. This was clearly seen at 30 GPa, when Zir (312) intersected with Zir (112).

As for the Zir (101) plane, it had a similar behavior to both the Zir (200) and Zir (112) planes. The slope was getting gentler as Zir (200) after 18 GPa, which can mean that it was close to plastic deformation region. The differential stress supported by Zir (101) was sufficiently higher than for Zir (200). It closely followed Zir (112) with 0.5 GPa difference up to 18 GPa. After this pressure, the trend started to narrow down and the difference increased up to 1 GPa. At 30 GPa, differential stress supported by Zir (101) reaches 4.2 GPa.

Due to the problem with overlapping zircon peaks by much stronger Be and BeO peaks, Zir (031) and Zir (213) planes were presented only in a limited pressure range. But even at that range their behaviors fully supported the behavior of other planes. Differential stress increased gradually and at the highest pressure where those planes were observed, $t = 3$ GPa for Zir (031) (at $P = 21.5$ GPa) and $t = 2$ GPa for Zir (213) (at 17 GPa). Unfortunately, it is hard to make further conclusions due to the lack of experimental data at higher pressure ranges.

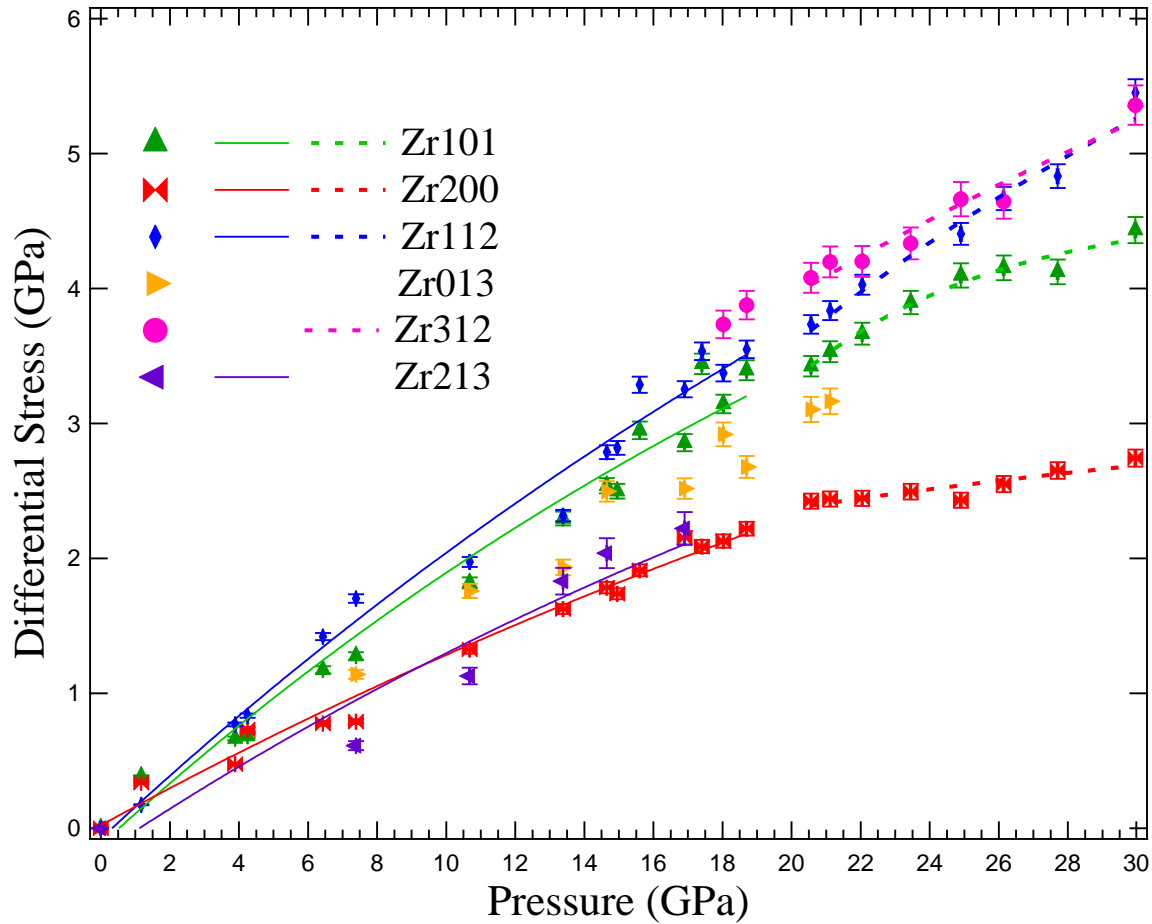


Figure 4.12 Differential stress over pressure for zircon up to 30 GPa. Polynomial (exponential) fit is applied to each plane. Solid line represents fit before phase transition (before reidite was observed), dashed line represents data after transition (both zircon and reidite phases are present).

The analysis of differential stress/shear stress ratio suggests that zircon has relatively low values of the t/G ratio, compared to other mantle minerals, such as olivine and ringwoodite below 15 GPa. The ratio gradually increases up to 15 GPa, after which it slows down. The trend above 20 GPa is more consistent with that of ringwoodite (Kavner and Duffy 2001), though the values of the t/G ratio of zircon are still lower than that of ringwoodite. This can be because of the contribution of reidite.

The obtained differential stress of zircon was compared to the differential stress of main mantle phases obtained from in situ compression at ambient temperatures (Figure 4.13). The values used for the analysis were reported elsewhere. Two methods were used to get data points:

lattice strain theory (Kavner and Duffy, 2001, Uchida 1996) and peak width methods (Chen 1998). The comparison suggests that the studied material has sufficiently lower differential stress than all the materials it was compared to (olivine, ringwoodite, majorite, wadsleite, garnet and Ca perovskite). In addition, zircon is very sensitive to stress, which is obvious from the fact that there is low differential stress below 1 GPa. Zircon supports linear increase of differential stress with pressure, the same as ringwoodite (Chen *et al.*, 1998, Kavner and Duffy, 2001). The linear trend with relatively sharp slope was detected for both zircon and ringwoodite (Kavner and Duffy, 2001). But from Chen *et al.*, (1998), the slope of ringwoodite is smaller. Differential stress of ringwoodite is almost twice higher than that of zircon. At pressure below 3 GPa, zircon has the same value of differential stress as olivine, and is the same as grossular at slightly higher pressure (i.e. 6 GPa) (Kavner 2007). But with pressure increase, olivine and grossular experience sharp jumps in differential stress which is getting smaller at 15 GPa, while differential stress of zircon grows gradually. Although there is no data for the differential stress of olivine above 17 GPa, based on its trend suggests that the value of differential stress will be in the range of 4.5-5 GPa. Therefore, it is estimated at 30 GPa, the differential stress of zircon is almost the same as that of olivine (4.5 GPa at pressure 30 GPa). Ca perovskite shows low differential stress at pressure of 18-19 GPa and is comparable with zircon (Shieh *et al.*, 2004). Wadsleite shows slightly higher trend than that of olivine but definitely its values are significantly higher than that of zircon.

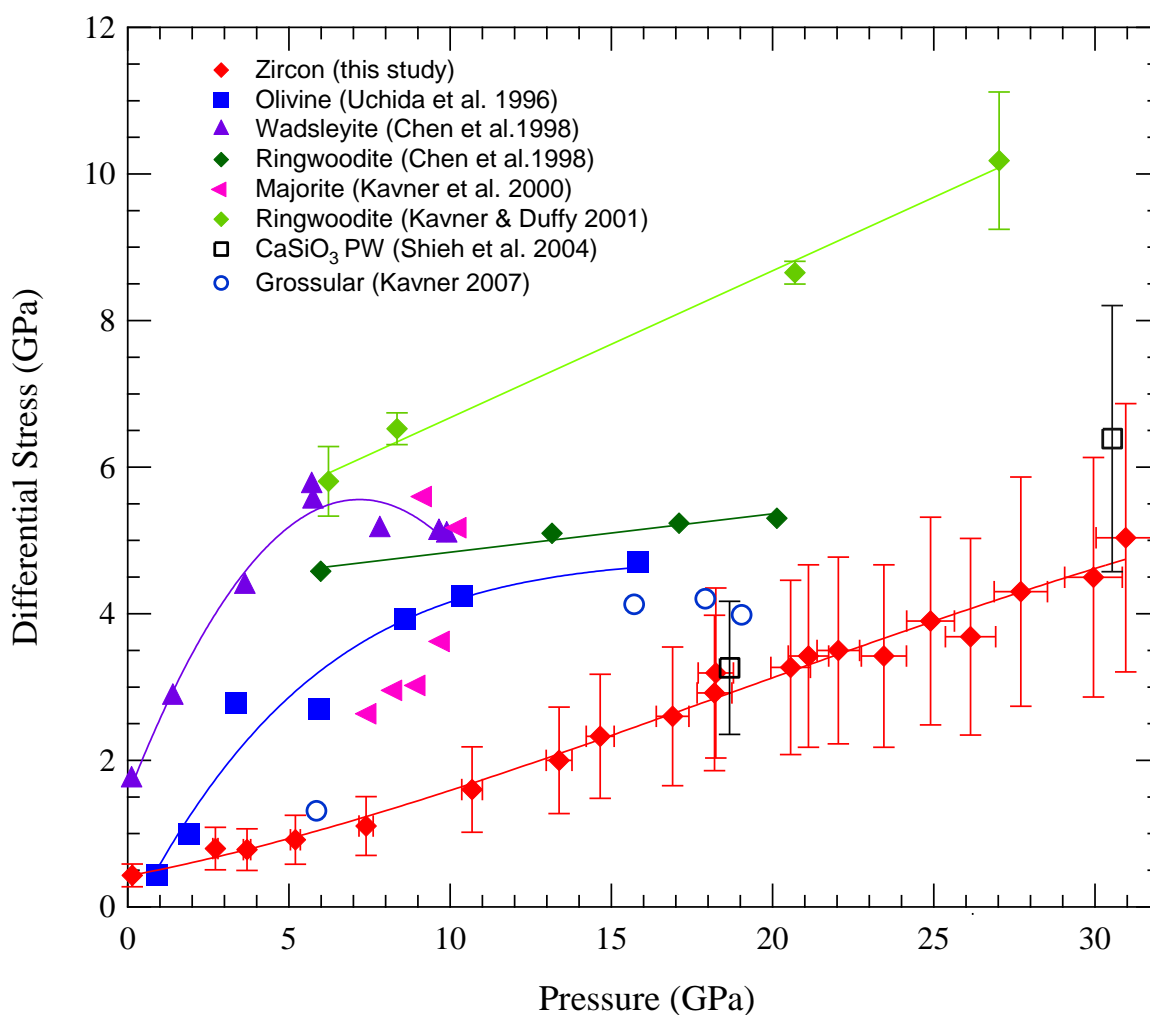


Figure 4.13 Differential stress over pressure for different minerals up to 30 GPa: zircon (red diamonds, this study), ringwoodite (light green diamonds- Kavner and Duffy, 2001; dark green diamonds-Chen *et al.*, 1998); olivine (blue squares- Uchida *et al.*, 1996); majorite (pink triangles- Kavner *et al.*, 2000); wadsleyite (purple triangles- Chen *et al.*, 1998); grossular (open circles – Kavner 2007); CaSiO₃ PW (open squares – Shieh *et al.*, 2004). Polynomial or linear fit is applied.

4.2. Equation of state

The overall quality of the initial diffraction data of zircon was evaluated by fitting the volume data of the sample to a third order Birch-Murnaghan equation of state. The volumes were calculated using d -spacings at three different angles, which corresponded to maximum ($\psi = 0^\circ$), minimum ($\psi = 90^\circ$) and hydrostatic ($\psi = 54.7^\circ$) stress states of the material. Third order Birch-Murnaghan equation of state was used to obtain the equation of state for corresponding stress conditions:

$$P = \frac{2}{3}K_{0T} \left[\left(\frac{V_0}{V} \right)^{7/3} - \left(\frac{V_0}{V} \right)^{5/3} \right] - \left\{ 1 - \frac{3}{4} (4 - K'_{0T}) \left[\left(\frac{V_0}{V} \right)^{2/3} - 1 \right] \right\} \quad (4.2)$$

Zircon is considered the most incompressible material with SiO_4 polyhedra (Scott *et al.*, 2002). Several studies were conducted in order to obtain reasonable values that could describe the nature of this strong material (Hazen and Finger, 1979, Crocombette and Ghaleb, 1998, van Westrenen *et al.*, 2004, Ono *et al.*, 2004). Hazen and Finger in 1979 reported two values of bulk modulus ($K_{0T} = 227$ GPa if K'_0 is fixed at 6.5 and $K_{0T} = 234$ GPa if K'_0 is fixed at 4). Crocombette and Ghaleb (1998) obtained $K_{0T} = 245$ GPa using six k points determined by the Monkhorst–Pack method. One of the latest bulk modulus was reported by Scott *et al.* (2002) ($K_{0T} = 301 \pm 12.5$ GPa) from a static compression experiment for scheelite-structured zircon. Van Westrenen *et al.*, (2004) managed to separate zircon and reidite and reported $K_{0T} = 199 \pm 1$ GPa for synthetic zircon. Ono *et al.*, (2004) reported bulk modulus, which is $K_{0T} = 205 \pm 8$ GPa, slightly higher than van Westrenen *et al.* (2004). Bulk modulus for amorphous zircon was reported by Tkachenko *et al.*, in 2007, and it was 92 ± 5 GPa.

In the current study, volume data were obtained from three datasets. The data are in broad relation with previous studies. Volume at ambient conditions was obtained from 1 bar diffraction pattern collected for each dataset ($V = 260.819 \text{ cm}^3/\text{g}$). K'_{0T} was fixed at 4, which was derived from the plot of normalized pressure (F) to Eulerian finite strain (f) linear relation as well as it was previously used in all EoS studies of zircon. The equation of state for hydrostatic conditions has an interesting trend (Figure 4.14). Below 11 GPa bulk modulus is determined as $K_{0T} = 203.1 \pm 13.4$ and is consistent with van Westrenen *et al.* (199 ± 1 GPa) (2004) and Ono *et al.* (205 ± 8 GPa) (2004). In the range from 11 to 15 GPa the V/V_0 of zircon slightly increases and this causes increase in bulk modulus. In this region my data ($K_{0T} = 225$ GPa) is in good agreement

with the one reported by Hazen and Finger ($K_{oT} = 227$ GPa) (1979). Above 15 GPa and up to 22 GPa incompressibility increases up to 240 GPa, which is in agreement with the values reported by Crocombette and Ghaleb ($K_{oT} = 245$ GPa) (1998). The equation of state at higher pressure yields bulk modulus of 259 ± 5.86 GPa. This discrepancy in bulk modulus values could be explained by applied stress to the material. Some contributions can come from reidite, which first appears above 18 GPa.

Obtained EOS fit was used for calculation of bulk modulus of the material at maximum and minimum stress, as well as at hydrostatic conditions. Obtained values show that at maximum stress the material behaves as the most compressible, the bulk modulus is $K_{oT} = 153 \pm 4.36$ GPa. These values are typical for various types of steel (159-165 GPa) and gold ($K_{oT} = 167$ GPa) (Callister 2013). Incompressibility at minimum stress conditions is much higher ($K_{oT} = 387.71 \pm 10.4$ GPa), which means that the material is extremely strong. This value lies in the range from tungsten carbide ($K_{oT} = 323 \pm 1$) reported by Xiong *et al.*, 2013 to diamond (443 GPa) (Kittel 2005).

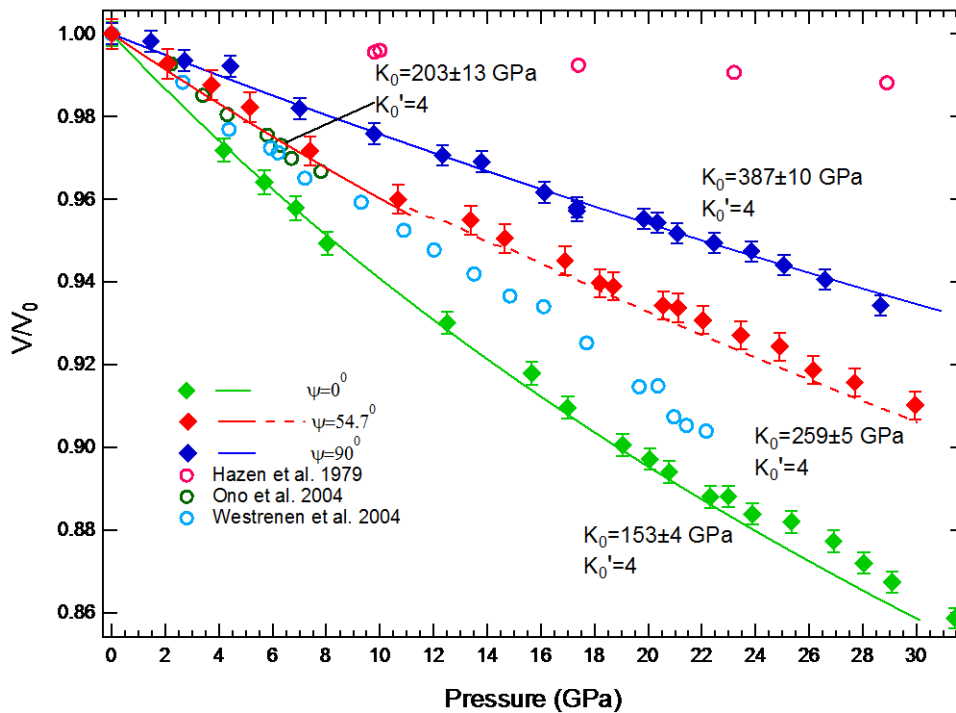


Figure 4.14 Equation of state of zircon at $\psi = 0^\circ$, 54.7° and 90° (solid diamonds). The solid curves are fits to the third order Birch-Murnaghan equation of state. Open circles are from Hazen *et al.* (1979), Ono *et al.* (2004) and van Westrenen *et al.* (2004).

4.3. Textures. Reitveld analysis

Texture and “lattice preferred orientation” are characteristics of the polycrystalline material. In material science, texture can be defined as an arrangement of the “building blocks” or, in other words, distribution of crystallographic orientations in a polycrystalline sample (Suwas and Gurao, 2008). It means that grains are distributed either in particular directions or randomly (no texture).

Texture can be studied by analyzing neutron, x-ray diffraction data and SEM. MAUD with Reitveld analysis uses a method of least squares to refine a theoretical line profile of reflections of a diffraction pattern (peaks in intensity). The ultimate purpose of the method is to obtain the most perfect fit with the measured profile, simultaneously refining microstructure and texture. This profile can be converted into a pole figure, which is a stereographic projection of pole density as a function of pole orientation. Real distribution of directions in the reference frame of the crystal can be detected from the inverse pole figures.

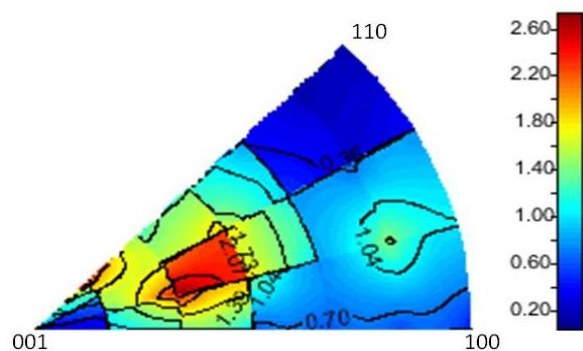
Zircon is not only a strong material but also is very sensitive to stress conditions. It shows signs of texture development at as low as 3.89 GPa (Figure 4.15). In the range of 3.89 to about 10 GPa most grains are oriented along the (001) plane, which lies in the plane of maximum stress direction in DAC. With increasing pressure, rotation of the texture from (001) to (110) has been observed. Along with texture rotation, a new development in the middle of (100) and (110) was observed in the pressure range of 11 to 14.5 GPa. This texture exists only in the limited pressure range and disappears at pressure above 14.5 GPa. At higher pressures, texture reorients from (001) to (110), which can be clearly observed in the inverse pole figures at 18.6 and 22 GPa.

It has been observed that texture development is also related to grain size. Higher intensities and textures were typical for the sample with larger sizes of grains (1st dataset).

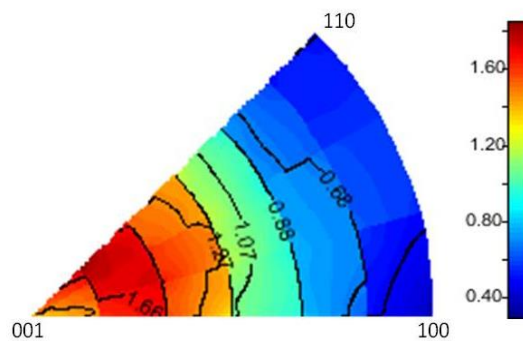
Diffraction patterns were also analysed in terms of texture index variation. Texture index is defined as the volume averaged integral of squared orientation density across the orientation distribution function. The value can vary from 1 (random powder) to infinity (perfect texture or single crystal) (Bunge 1982). In this study it was detected that texture index gradually increased from 1.4374 (1 bar) to 7.2698 (11 GPa) (Table 4.2). The first number shows that even at very

low pressure, there are some signs of its existence. In the range from 11 to 14 GPa, a sudden jump in the texture index (12.59) has been observed. This could be explained by the development of texture in a new area (between (100) and (110)). After its disappearance, texture index returned close to its previous value (5.55). This indicates that the texture was becoming weaker. Given this result, in general, with pressure increase texture index gradually increases too.

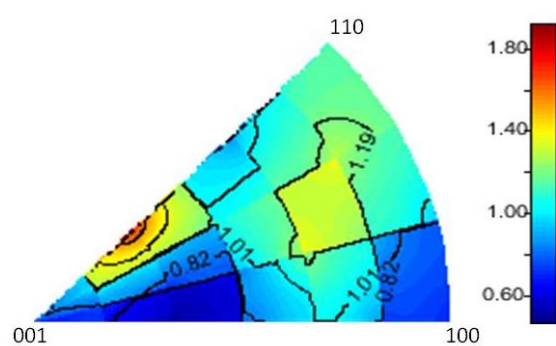
3.89 GPa



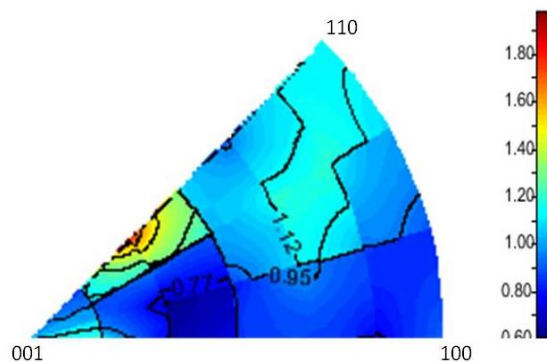
4.28 GPa



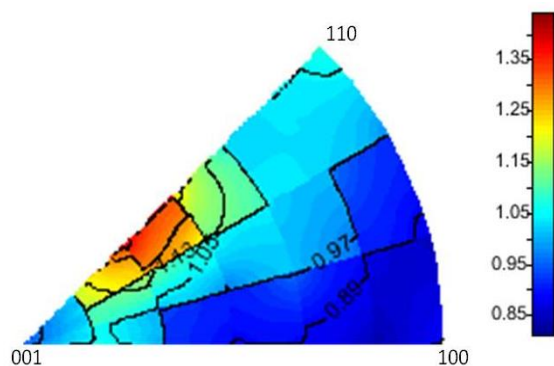
10.68 GPa



14.5 GPa



18.29



22.04 GPa

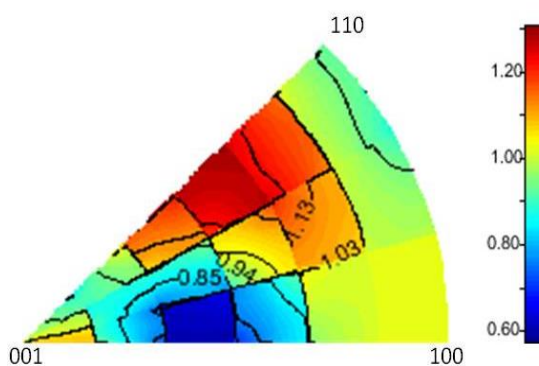


Figure 4.15 Inverse pole figures (IPFs) obtained from Reitveld analysis showing texture development along compression axis at different pressures. Texture was fit in MAUD with the E-WIMV model and fixed fiber symmetry. Intensity scale (in m.r.d.) is shown to the right of each figure. The scale was normalized in order to get comparable values.

Table 4.4 Variation of texture index of zircon at different pressures. The values were obtained from E-WIMV model of MAUD software with fixed 4-fold geometry.

Pressure	Texture index
0.0001 GPa	1.4374
0.04 GPa	3.2216
5 GPa	5.1607
7 GPa	6.6838
11 GPa	7.2698
13.38 GPa	12.5969
15 GPa	5.5506
16.9 GPa	7.6943
17.39 GPa	7.0231
18.29 GPa	13.4246
20.56 GPa	12.6667
22 GPa	24.9828

As has been previously reported elsewhere (Leroux *et al.*, 1999, Reddy *et al.*, 2007, Kovaleva *et al.*, 2014), zircon has tetragonal symmetry with two equivalent [100] and [010] directions. This means that two relevant orthogonal active glide systems are [100](010) and [010](100) that correspond to a slip system $\langle 100 \rangle \{010\}$. From our texture analysis, it is impossible to make conclusions about slip systems in zircon, but differential stress supports reported slip system information ((200) is the weakest plane).

Differential stress values, along with the results of the texture analysis allow us to make a comparison between zircon and olivine. As described earlier, $\langle 100 \rangle \{010\}$, or “a-slip” system, is the prevailing slip system that works in zircon. Below 3-4 GPa (1600 K) deformations in olivine

mostly contribute to the same slip system. Later in both minerals the contribution of “a-slip” decreases relative to “c-slip” [001] (010), which becomes the primary slip system (Hilairet *et al.*, 2012), so the c-slip becomes profound.

4.4. Raman spectroscopy

A powdered zircon sample was analyzed using Raman spectroscopy. The initial zircon powder was ground in two agate mortars of different size for 45 and 15 minutes, respectively (Figure 4.16). Acetone was added to make the grains more homogeneous and more easily ground.

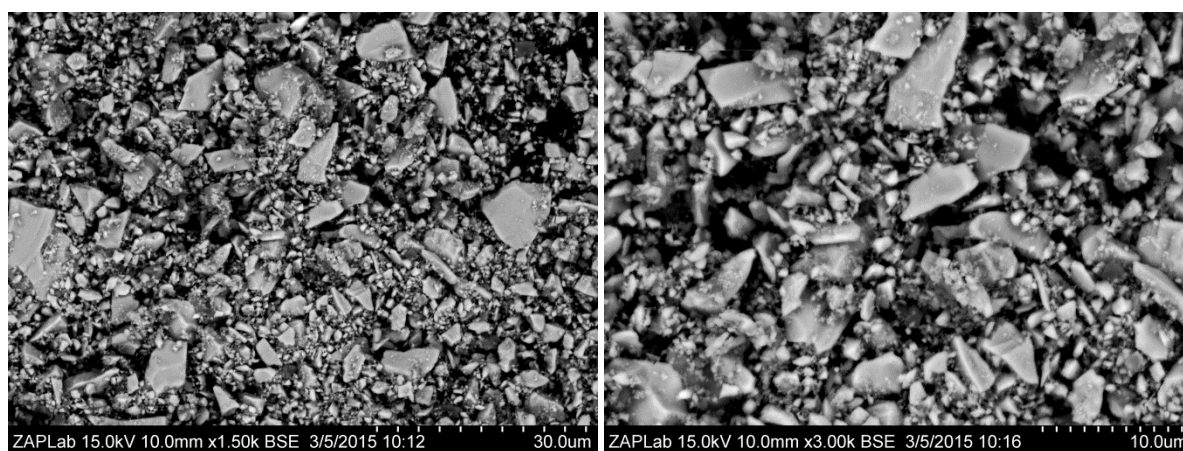


Figure 4.16 SEM image of bulk zircon grained sample. A-1500 times enlarged, B- 3000 times enlarged.

After that, the powder was packed into a 100 micron hole in a stainless steel gasket. The gasket was previously preintended to 27 microns. The 100 micron hole was drilled exactly in the centre of the gasket. A diamond-anvil cell with 300 micron culet size diamonds was used for the experiment. A small ruby (10 microns) was placed in the centre of the cylinder part of the DAC. The ruby, together with diamond, was used as a pressure determination tool. The sample was nonhydrostatically compressed to 21 GPa (Figure 4.17).

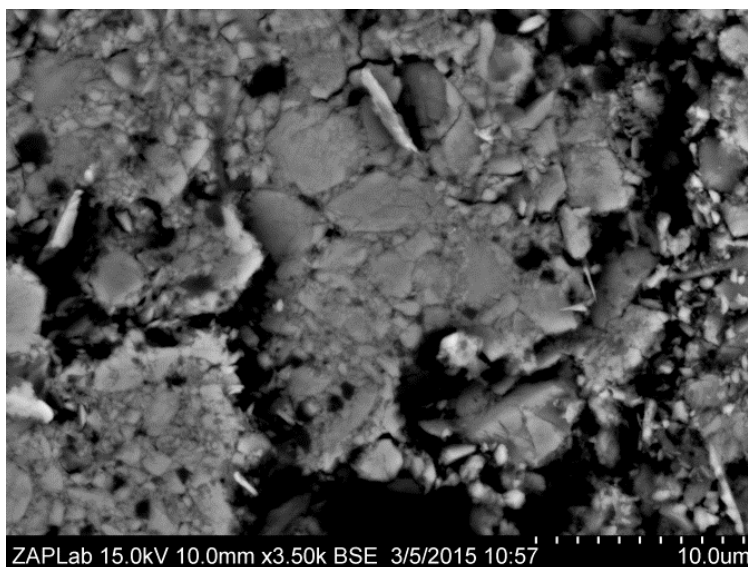


Figure 4.17 SEM picture of quenched sample of zircon powder compressed to 22 GPa in DAC using stainless steel gasket with 100 microns hole.

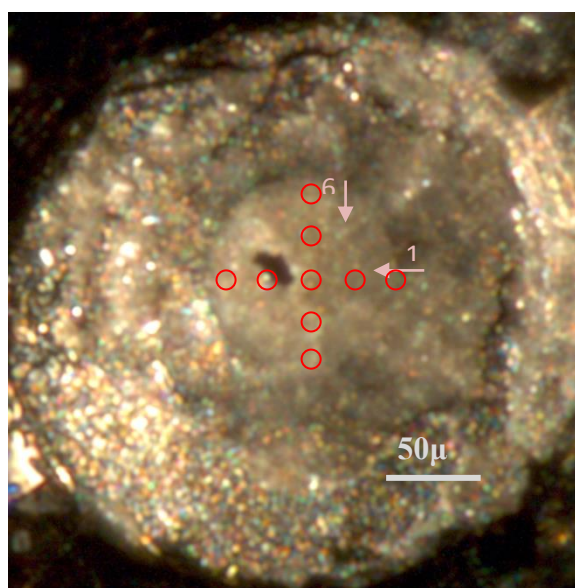


Figure 4.18 Location of points that were used for mapping of zircon sample using Raman spectroscopy.

Raman spectra of the sample and ruby were collected after each compression. The step was approximately 1.5-2 GPa for low pressure and 1 GPa for high pressure (after 15 GPa). At the highest pressure, different regions of the sample chamber were probed in order to detect distribution of high pressure polymorph of zircon (reidite). A total of 10 points (Figure 4.18) in

both the horizontal and the vertical direction were analysed. Pressure distribution at each point was obtained from diamond spectra based on a study by Akahama and Kawamura (2006). Each Raman spectra was collected three times for 45 sec in order to reduce the noise and the background level.

As was previously stated, zircon has 12 Raman modes in total (Table 1.2) (Finch *et al.*, 2001). Four distinctive peaks (E_g , A_{1g}, ν_2 ; A_{1g}, ν_1 ; B_{1g}, ν_3) of zircon were detected at frequencies of 362, 440, 988 and 1022 at 3.7 GPa. These frequencies are in good agreement with those previously reported for zircon (Gucsik *et al.*, 2004). With increasing pressure, peaks shifted to higher frequencies (Figure 4.19). At 11.4 GPa, the E_g peak shifted to 388, A_{1g}, ν_2 - to 449, A_{1g} - 1018 and B_{1g}, ν_3 to 1061. In the range between 4 and 10 GPa, A_{1g}, ν_1 ; B_{1g}, ν_3 merged together, though in higher pressure ranges they separated again. Starting from around 16 GPa, the first and second peaks started to merge together. First evidence of phase transition from zircon to reidite was observed at 19 GPa. Phase transformation to reidite was proven by the occurrence of an additional Raman band at around 596 cm^{-1} .

At the highest pressure conditions (21.7 GPa) multiple Raman spectra were collected (Figure 4.18). As is clear from Figure 4.19, in the central part of the initial material has already transformed to reidite (which is obvious from the occurrence of the reidite peak). From the middle part to the edge, reidite gradually disappears. This means that phase transition was not fully finished. And on the edge, we see clear zircon spectra with no evidence of reidite.

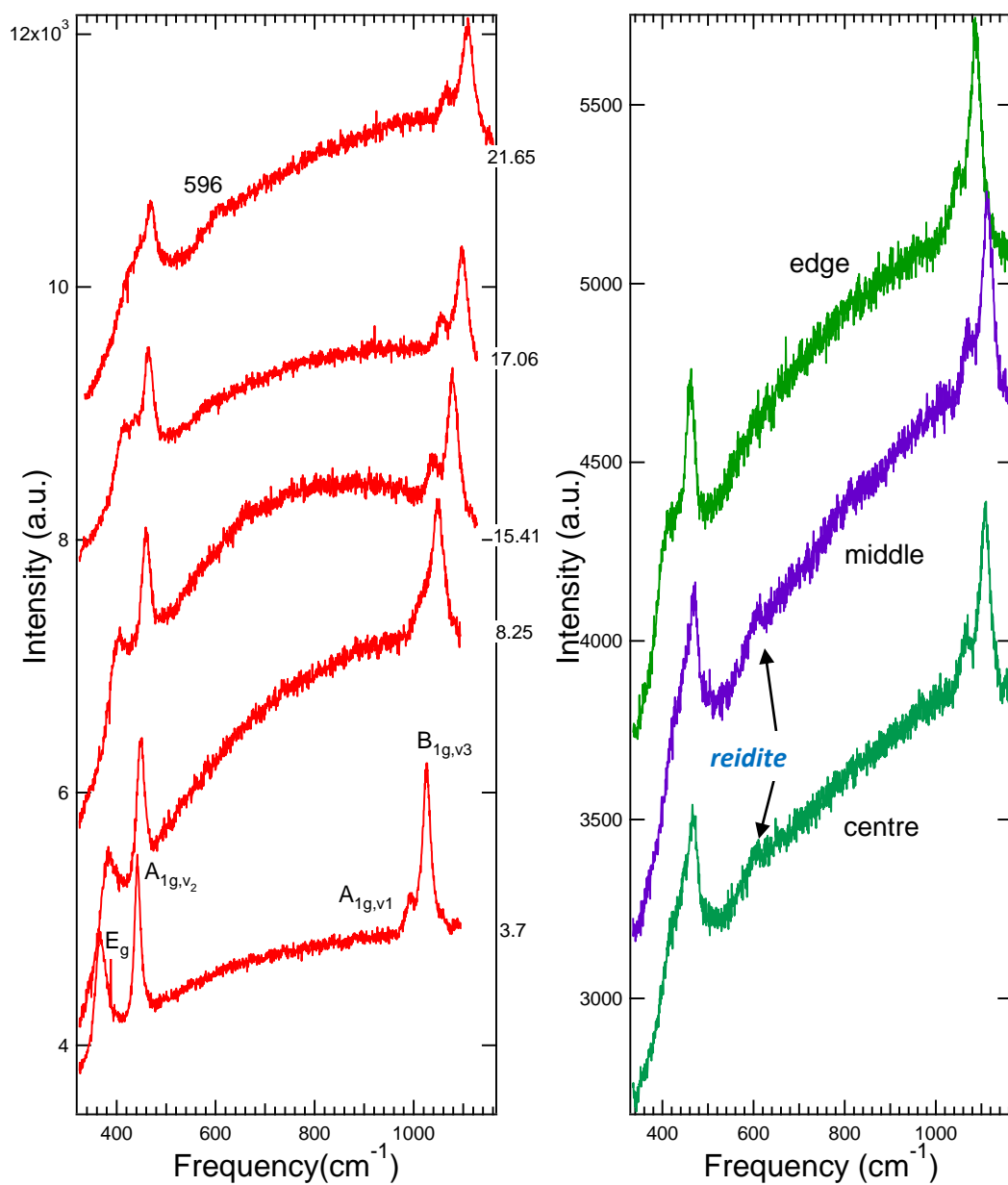


Figure 4.19 Raman spectra of zircon. A- spectra collected at different pressures, pressures are shown near each spectra to the right; b- spectra collected at highest pressure (21 GPa) in different regions.

4.5. EBSD

Two quenched zircon samples (1st- compressed to 20 GPa, 2nd- compressed to 32 GPa) were analyzed using the EBSD method on SEM. A total of six EBSD were taken for Sample #1 and four maps for the second.

The band contrast of the EBSD maps, or the intensity of the diffraction pattern, is high (from 20 to 120 DPI). This means that the quality of the obtained maps is good (Figures 4.20, 4.22). Moreover, the samples were analysed in terms of mineralogical composition. It was detected that the first sample was almost purely zircon with some corundum grains (Figure 4.21) and the second sample contained about 20 % reidite. This is consistent with what was reported by Fiske *et al.* (1994) who suggested that at 30 GPa around 10-15% of zircon transforms to a scheelite structure.

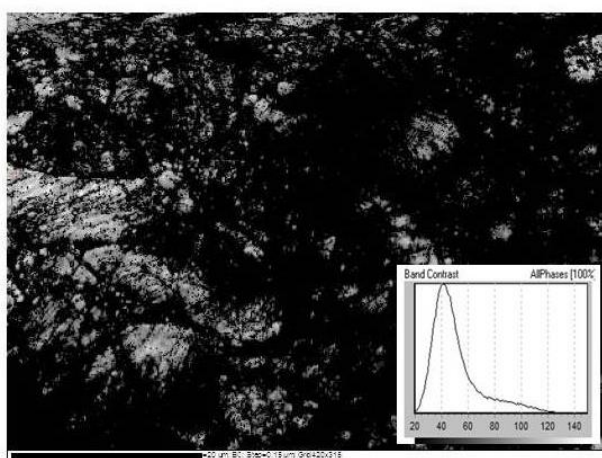


Figure 4.20 Band contrast of 500 EBSD D2
25 keV

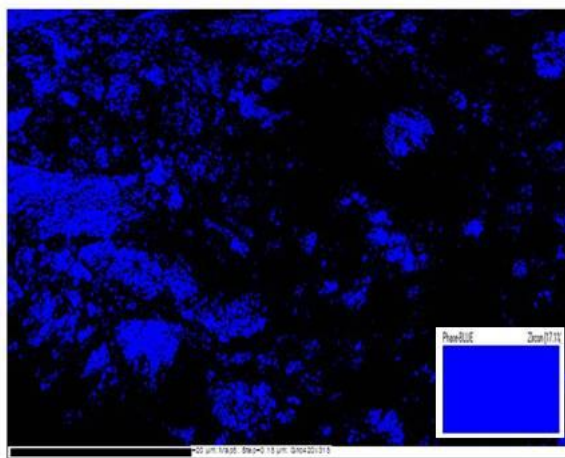


Figure 4.21 Composition of the sample.
Blue-zircon.

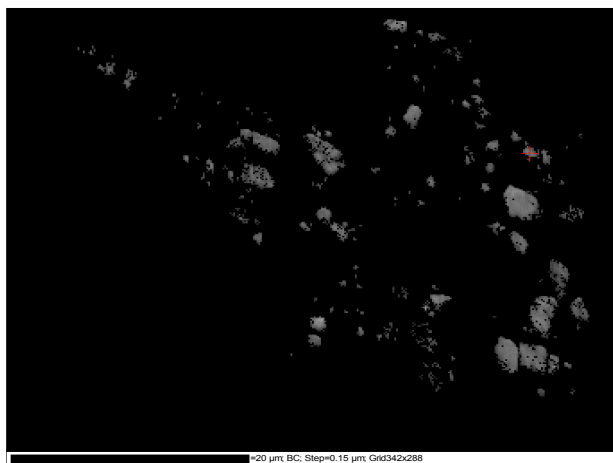


Figure 4.22 Band contrast of 300 EBSD D2 25 keV

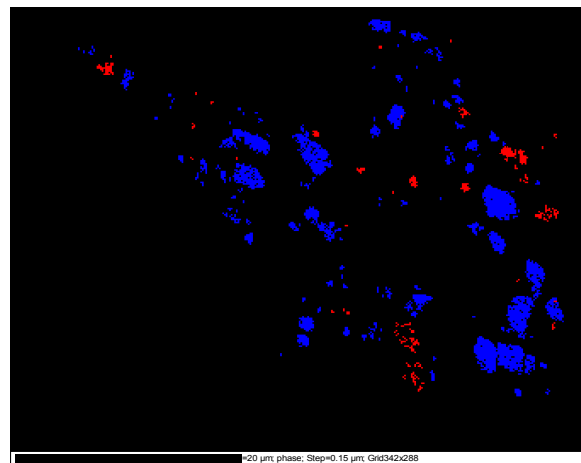


Figure 4.23 Composition of the sample. Blue-zircon, red- reidite.

The twinning of zircon has not yet been adequately studied. Before 1974, very little was known on this matter. In 1915 $\{101\}$ was reported to be the only well-established plane in zircon (Joselin and Pidgeon, 1974). Moser *et al.*, (2011) reported occurrence of microtwins in natural zircons about a $[110]$ axis with slight asterism of $\{100\}$, $\{001\}$ and $\{011\}$ poles. They were the first observed microtwins in zircon. They connected the creation of the twins with the late shock event when the planar features were “reworking” during the rarefaction stage. The asterism was caused by the internal crystal-plastic strain on the c-axis, accommodated by glide along (112) (Moser *et al.*, 2011). As a result of the EBSD experiment (Erickson *et al.*, 2013), some polysynthetic microtwins were detected along $\{112\}$. Those twins consisted of sets of lamellae of zircon oriented 65° about $\langle 110 \rangle$. Those twins were spotted within single grains in multiple crosscutting of $\{112\}$ (Erickson *et al.*, 2013).

Twinning is a typical process for reidite (Leroux *et al.*, 1999), especially if it is associated with zircon to reidite transition (Timms *et al.*, 2012) during a shock event. In impact structures, microtwinned lamellae within the planar microstructures that are parallel to $\{112\}$ have been considered a characteristic feature of reidite (Leroux *et al.*, 1999, Timms *et al.*, 2012). Moreover, the occurrence of those microtwinned lamellae is used as evidence of ultrahigh-pressure shock metamorphism (Cavosie *et al.*, 2015). It has been reported that the transition to scheelite structure is nucleated along $\{100\}$ planes in zircon via a simple shear mechanism. Basically, the

[110] plane of zircon undergoes transition to the [100] plane of reidite and (112) of zircon aligns with (112) of reidite (Leroux *et al.*, 1999, Kusaba *et al.*, 1985).

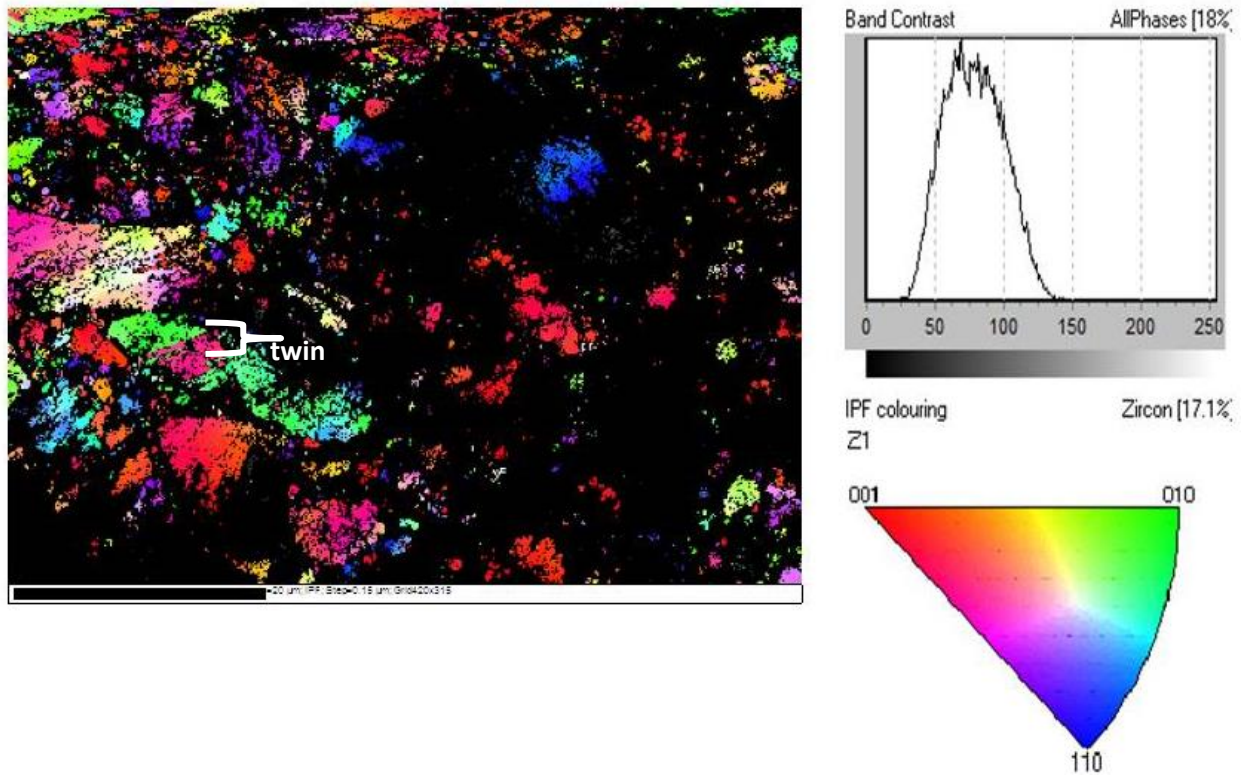


Figure 4.24 Texture development in 500 EBSD2 map 25 keV. Wide twin is labeled. Band contrast and IPF are shown on the right.

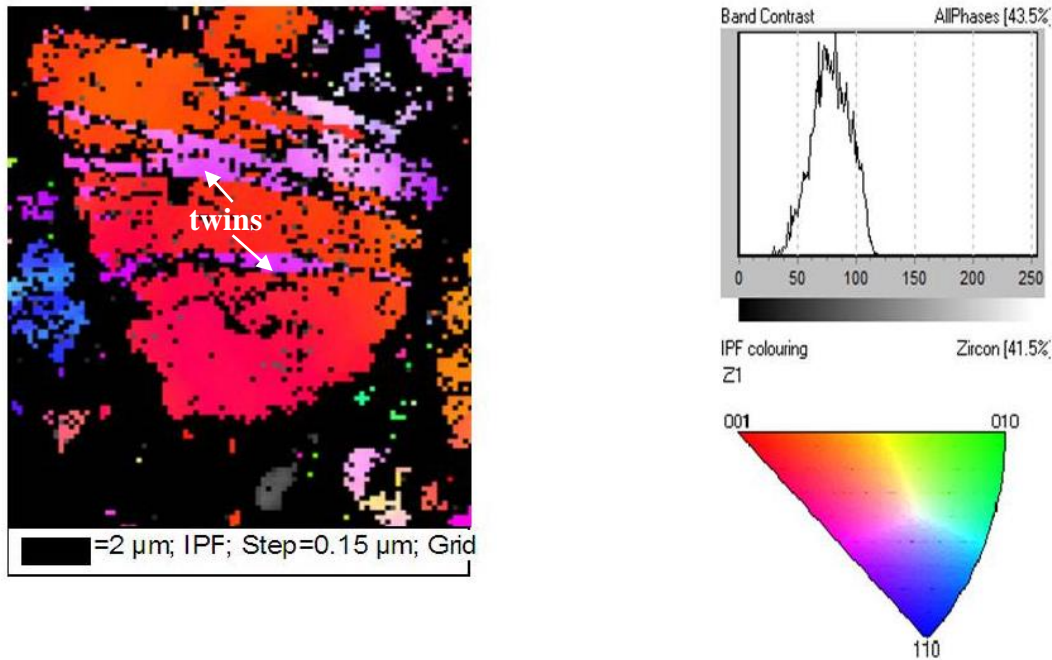


Figure 4.25 500 EBSD map 6 25 keV. Texture development and twinning in a zircon grain (1st sample). Host zircon grains parts are red, twinned parts are pink.

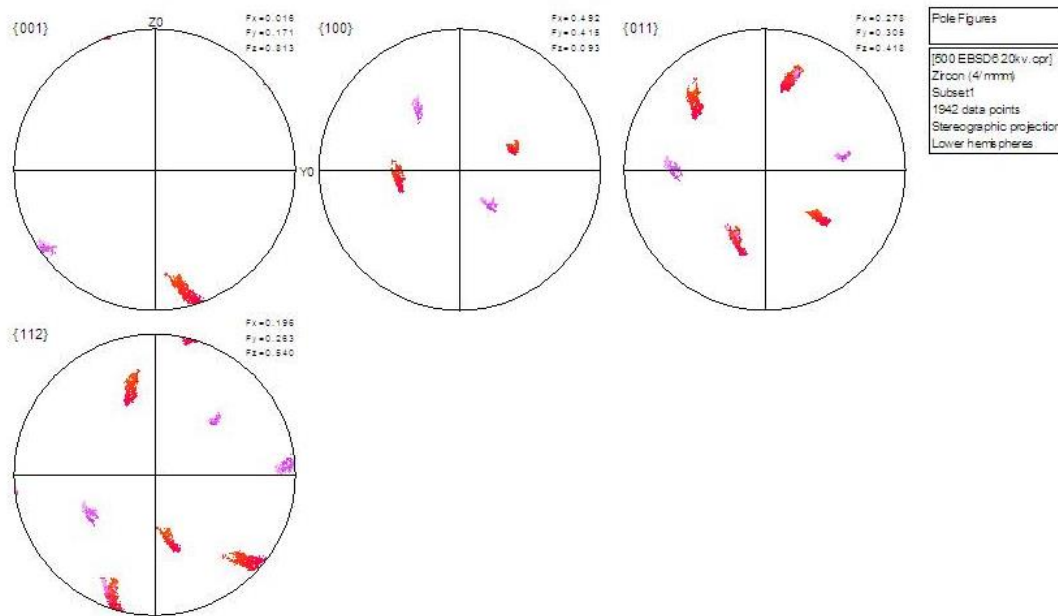


Figure 4.26 Stereographic projections of 500 EBSD 6 25 keV. Misorientation of a,b,c axes and (112) are colour-labelled (red- main body of the grain, pink- twinned zones).

The quenched sample has a residual strain (permanent) from 5 to 25 degrees within one grain, which is in good relationship with that previously reported for natural zircon. Strain is well preserved. The occurrence of zircon twins is not associated with grain boundaries. Twinned zones have “residual” strain as well, but almost two times lower than that of the nontwinned areas of the same grain. For “parent” grain areas, preserved strain rate varies from 11 to 21 degrees with some grains up to 25 degrees (Figure 4.26). Twinned zones have strain rate not higher than 13 degrees, and most abundant is at 8^0 - 9^0 (Figures 4.24 and 4.25). Not all the grains have twins, but they were spotted through the entire sample. The size of twins is different for each particular grain (it varies from 0.5 μm to almost 4 μm).

No particular texture was observed for the recovered zircon sample previously compressed to 20 GPa. The opposite situation was observed for the sample compressed to 33 GPa. A clear texture along (001) was observed as is seen from Figure 4.27. Pole figure higher intensities were all concentrated in the centre of the pole figure. Reidite grains, on the contrary, were randomly distributed, which means that no preferred orientation at 33 GPa was observed for reidite.

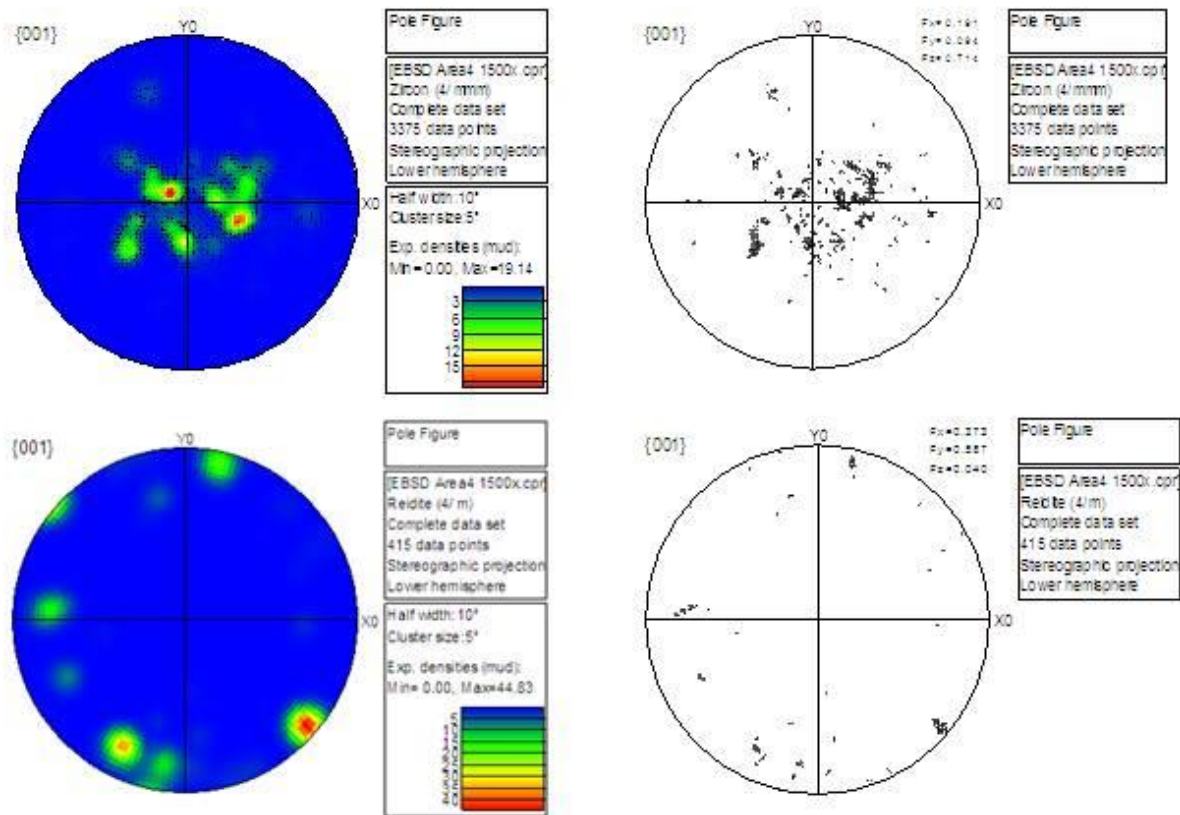


Figure 4.27 Pole figures for zircon (top) and reidite (bottom) derived from EBSD technique for a quenched sample #2.

As has been mentioned earlier, the first sample consists of purely zircon phase. Taking the detected twinning into consideration, it can be concluded that twins were created within the stability field of zircon and this was caused purely by the deformation processes. This was a new discovery as previously twinning processes in natural zircons were associated with shocked processes. The formation of those twins was previously explained by phase transition from zircon to reidite.

4.6. Geological implication

Strength study of a material in controlled environment can provide with important information about mechanical properties of the material. It is understandable that experiments conducted at low temperature cannot fully represent the conditions of deep Earth, but they are still of great importance for providing valuable geological information. So far no studies on the differential stress of zircon were conducted under high pressures; in such a case this study focuses on pressure dependence of strength of zircon without any influence of temperature. Definitely, temperature would have great contribution to the differential stresses. Therefore, further examination of zircon under high temperature should be the next step in zircon.

Zircon has been popularly used as an age determination tool in geology for years. Its strength to resist to the applied stress coupled with its ability to retain Th and U has made it very important for geochronological studies. One of the main goals in current study was to evaluate the strength of zircon and to evaluate the relationship between the mechanical properties of the material and the ability of material to create pathways for diffusion (Reddy *et al.*, 2006). In the case of a mechanism at lower temperatures, “Pb loss” can happen due to enhanced diffusion caused by various processes. Elsewhere it has been described that this problem can happen due to the effect of self-irradiation that causes metamictization (Chernyak *et al.*, 1991). Nevertheless, what is of great interest is that this loss can be caused by crystal-plastic deformation (Moser *et al.*, 2009, Piazzolo *et al.*, 2012). In the case of plastic deformation that occurs after the rocks were formed, the whole isotopic system “reset”, which means that due to the superimposed diffusion, zircon may lose part of its initial Pb. My study suggests that below 18 GPa and room T zircon is still in its elastic regime, so the deformations can be reversible. At 18 GPa zircon undergoes plastic deformation. Moreover, Zir (200) was found to be the weakest plane, which means that this plane will be the first to deform in zircon, and expects to activate diffusion processes.

In fact this observation is supported by reported slip systems found in zircon (Leroux *et al.*, 1999, Reddy *et al.*, 2007, Kovaleva *et al.*, 2014). Experimental results show that Zir (200) exceeds its elastic limit at around 18 GPa and encounters deformation at low temperature. This means that at ambient temperature and above 18 GPa, activation of the slip plane of zircon is likely.

Based on this idea, one can infer that at higher pressure conditions some of the initial elements within zircon can begin to diffuse. Notable, this situation does not take into consideration of temperature effect. In the case of impact crater formation, geological materials are subjected to both temperature and pressure and therefore will influence the physical properties of the rocks. Therefore, dislocations may happen at even at lower pressures and low temperatures.

Additionally, in nature, zircon is usually found close to pyroxene and/or garnet. Garnet is much stronger than zircon, based on this study. This means that zircon is more likely to be affected when next to garnet in an impact event. It has also been reported that sometimes zircon can stay unchanged even after external applied forces. For the role of pyroxene, it is limited to current available data and cannot have a conclusive answer. However, natural observation suggested higher strain rate of zircon was observed when exists next to pyroxene.

My study suggests that strength of zircon is much weaker than it was expected at low temperatures. It is almost two times weaker than most popular minerals in mantle, such as olivine, ringwoodite and garnet. This means, most likely, when there is deformation occurred, zircon will be the first to respond and deform at high pressure and low temperature conditions. Nevertheless this kind of trend is not observed in nature. This brings the conclusion that temperature effect may have a great influence on differential stress and strength of the mantle phases.

Twinning in zircon crystals has already been reported elsewhere (Erickson *et al.*, 2013, Leroux *et al.*, 1999, Moser *et al.*, 2011, Timms *et al.*, 2012). Those twins were observed at naturally shocked samples. Moreover, they were explained by occurrence as phase-transformation related. Later this point of view was questioned by Moser *et al.* (2011). In this study twinning was observed within the stability field of zircon and was not associated with phase transformation from zircon to reidite. Also those twins were originated not from the shock, but from the static compression at low temperatures. This means that even at low temperatures zircon can be deformed plastically with formation of deformational twins with 65° misorientation.

4.7. Future studies

The current research was conducted in a diamond-anvil cell to 32 GPa at ambient temperatures. Further research on zircon at high temperatures and at higher pressure conditions is required. The evaluation of high temperature can provide insightful information about the processes that take place in impact craters and in mantle conditions. Moreover, recent publications (from theoretical calculations) suggest that, at higher pressure, scheelite structured reidite undergoes second order transition to a wolframite structure. But so far no *in situ* study of this transition has been conducted.

Additionally, this study of differential stress was limited to 32 GPa, which allowed the detection of plastic transformation on the (200) plane. Higher pressure investigation is required to detect the yield pressure when zircon undergoes plastic deformation, as well as the pressure conditions at which particular zircon planes undergo plastic deformation.

Some limitations of the method and equipment used in the current research did not allow for the analysis of the complete range of crystallographic planes of zircon (ex. overlapping of zircon peaks by Be and BeO peaks with higher intensity). This is the reason why it is suggested to substitute the Be gasket by using the B-epoxy insert with Kapton tape. The combination of B-epoxy insert with Kapton tape does not give significant diffraction peaks and can be easily reduce contributions from the gasket materials during analysis. By using this relatively new gasket material it is possible to obtain more information from crystallographic planes and fill in the blanks in the current research. As a result, more accurate volume data can be obtained. This will lead to clarification of the equation of state of zircon.

5. CONCLUSIONS

Zircon was studied up to 32 GPa using angle-dispersive X-ray diffraction in radial geometry in a diamond-anvil cell at ambient temperatures at National Synchrotron Light Source, Brookhaven National Laboratory, Upton NY. The sample was also analyzed using Raman spectroscopy at the High Pressure DAC Laboratory at the University of Western Ontario, London ON. The quenched sample was analyzed by EBSD at ZAP Laboratory, the University of Western Ontario, London ON. Diffraction patterns were recorded with one GPa step in three runs (up to 20, 32 and 33 GPa). Pressure was obtained from the equation of state for gold, based on Au 111, Au 200 and Au 220. The analysis of the zircon sample was based on seven zircon planes (101, 200, 211, 112, 301, 013, 312 and 213). Lattice strain theory was applied to the diffraction data to calculate the differential stress of each crystallographic plane. The value of shear stress was reported by Tkachenko *et al.* (2007).

Ratio of differential stress to shear modulus (τ/G) supported by zircon was in the range of 0.2-0.8%. Differential stress was found to be almost two times smaller than that for the most abundant phases of the upper mantle (olivine, ringwoodite, wadsleyite and grossular). This could be explained by the shear strength of the zircon, as it appears to be sufficiently lower than that for the mantle minerals. Differential stress supported by (200) was the weakest and it underwent plastic deformation above 18 GPa. Zircon (112) is the strongest plane and yielded differential stress of 5.5 GPa at pressures around 30 GPa. Phase transition to reidite was found above 18.6 GPa, which was one GPa lower than in previous studies. This could be caused by shear strength. Zircon was found to be a very strong material with $K_0=203$ GPa, which was in good relationship with that previously reported by van Westrenen (2004) and Ono (2004). Pure zircon appeared to be more compressible than its natural analogue, as the obtained bulk modulus was almost 12% lower than that reported for natural zircon. Moreover, synthetic zircon was still almost 10% less compressible (stronger) than most mantle minerals mentioned earlier. A high pressure study also has shown that zircon is very sensitive to stress, as deformation was observed even at 1 GPa.

Reitveld analysis using MAUD software showed that weak texture was developed at 3 GPa along (001) and turned to (110) with pressure. The texture index supported the trend as it grew gradually with pressure. At 0.4 GPa, it was slightly higher than one, which meant that it

was close to random distribution, and it grew gradually up to 24 at 22 GPa. The analysis of the recovered sample with EBSD previously compressed to 32 GPa showed the preferred orientation of zircon grains along (001) and no particular texture for reidite.

Twinning with 65° misorientation along (110) in zircon within the stability field of zircon was detected using the EBSD technique. Twins were distributed randomly, with no particular texture. And also they were not associated with grain boundaries. Residual strain in “parent” zircon grains up to 21° and up to 13° within the twinned zones was also observed.

REFERENCES

- Akahama Y. and Kawamura H. (2006) Diamond anvil Raman pressure scale. *J. Appl. Phys.* **100**, 043516
- Akhtar, M.J., Waseem, S. (2001) Atomistic simulation studies of zircon. *Chem. Phys.* **274** 109-120.
- Anseau, M.R., Biloque, J.P., Fierens, P. (1976) Some studies on the thermal solid state stability of zircon. *Journal of Materials Science Letters* **11** (3), pp. 578-582
- Barker, I. R. (2014) Sample preparation Lab Techniques. ZAPLab, Western University
- Bassett, W.A., Brown, G.E.Jr. (1990) Synchrotron radiation: applications in the earth sciences. *Annu. Rev. Earth Planet. Sci.* **18**:387-447
- Bhimasenachar, J. and Venkatarathnam, G. (1955) Elastic constants of zircon. *The journal of the Acoustical Society of America*, **27**
- Boehler, R. (2006) New diamond cell for single-crystal x-ray diffraction. *Rev. Sci. Instrum.* **77**, 115103.
- Bohor B.F., Betterton W.J., Krogh T.E. (1993) Impact-shocked zircons: discovery of shock-induced textures reflecting increasing degrees of shock metamorphism, *Earth Planet. Sci. Lett.* **119** 419–424.
- Bunge, H. J. (1982) Texture Analysis in Materials Science-Mathematical Methods.
- Butterman, H., Foster, W.F. (1967) Zircon stability and the $\text{ZrO}_2\text{-SiO}_2$ phase diagram. *Amer. Mineral*, **52** pp. 880-885.
- Callister, W.D., Rethwisch, D.G. (2013) Materials Science and Engineering: An Introduction, 9th Edition.
- Cavosie, A.J., Erickson, T.M. and Timms, N.E. (2015) Nanoscale records of ancient shock deformation: Reidite (ZrSiO_4) in sandstone at the Ordovician Rock Elm impact crater. *Geology* **43**

Chaplot, S.L., Pinschovius, L., Choudhury, N. and Mittal, P. (2006) Phonon dispersion relations, phase transitions, and thermodynamic properties of ZrSiO_4 : inelastic neutron scattering experiments, shell model, and first-principles calculations. *Phys. Rev. B*, **73**, 94308.

Chen, J.T., Inoue, D.J., Weidner, Y. Wu, Vaughan, M.T. (1998) Strength and water weakening of mantle minerals, olivine, wadsleyite and ringwoodite, *Geophys. Res. Lett.*, **25**, 575–578 1103–1104

Cherniak, D. J., Lanford, W. A., and Ryerson, F. J.(1991) Lead diffusion in apatite and zircon using ion implantation and Rutherford Backscattering techniques. *Geochim. Cosmochim. Ac.* **55**, 1663–1673

Chung, H.-Y., Weinberger, M. B., Levine, J. B., Kavner, A., Yang, J.-M., Tolbert, S. H., and Kaner, R. B. (2007) Synthesis of ultra-incompressible superhard rhenium diboride at ambient pressure. *Science* **316**, 436

Crocombette, J. P. and Ghaleb, D. (1998) Modeling the structure of zircon (ZrSiO_4): empirical potentials, ab initio electronic structure *Journal of Nuclear Materials* **257** (3), 282–286

Crystallographic database for MAUD software. COD <http://www.crystallography.net>

Curtis, C.E. and Sowman, H.G. (1953) Investigation of the thermal dissociation, reassociation, and synthesis of zircon. *Journal of The American Ceramic Society*. Vol. **36** No. 6.

Dawson, P., Hargreave, M.M. and Wilkinson, G.F (1971) The vibrational spectrum of zircon (ZrSiO_4). *Journal of Physics C: Solid State Physics*, **4** 240256

Duffy, T.S. (2007) Strength of materials under static loading in the diamond anvil cell. *AIP Conf. Proc.* **955**, 639

Duffy, S., Shen, G., Heinz, D.L., Shu, J., Ma, Y., Mao, H.K., Hemley, R.J. and Singh, A.K. (1999) Lattice strains in gold and rhenium under non-hydrostatic compression to 37 GPa, *Phys. Rev. B* **60**, 15063-15073

Dutta, R. And Mandal, N. (2012) Structure, elasticity and stability of reidite (ZrSiO_4) under hydrostatic pressure: A density functional study. *Materials Chemistry and Physics* **135**, 322-329

Erickson, T.M., Cavosie, A.J., Moser, D.E., Barker, I.R. and Radovan, A.H. (2013) Correlating planar microstructures in shocked zircon from the Vredefort Dome at multiple scales: Crystallographic modeling, external and internal imaging, and EBSD structural analysis *Mineralogical Society of America* **98** (1)

Ewing, R.C., Lutze, W. (1997) Disposing of plutonium. *Science* **275**:737

Fei, Y., Ricolleau, A., Frank, M., Mibe, K., Shen, G., and Prakapenka, V. (2007) Toward an internally consistent pressure scale PNAS **104**, 9182

Ferrari, M. and Lutterotti, L (1994) Method for the simultaneous determination of anisotropic residual stresses and texture by X-ray diffraction, *J. Appl. Phys.*, **76** (11), 7246-55

Finch, J. R., Hanchar, M.J. (2003) Structure and chemistry of zircon and zircon-group minerals. In Hanchar, J.M. and Hoskin, P.W.O. eds., *Zircon. Mineralogical Society of America. Reviews in mineralogy and geochemistry*, v. **53** pp.1-25.

Finch, J. R., Hanchar, M. J., Hoskin, W.O. P. and Burns, C. P. (2001) Rare-earth elements in synthetic zircon: Part 2. A single-crystal X-ray study of xenotime. *American Mineralogist*, Volume **86** pages 681-689.

Fiske, P.S., Nellis, W.J., Sinha, A.K. (1994) Shock-induced phase transitions of ZrSiO_4 , reversion kinetics, and implications for terrestrial impact craters, *EOS Trans. Amer. Geophys. Union* **75** 416–417.

Glass, B.P., Liu, S. (2001) Discovery of high-pressure ZrSiO_4 polymorph in naturally occurring shock-metamorphosed zircons. *Geology* **29**:371–373

Glass, B.P., Liu, S., Leavens, P.B. (2002) Reidite: An impact-produced high-pressure polymorph of zircon found in marine sediments. *Am Mineral* **87**:562–565

Gurao, N., Suwas, S. and Kapoor, R. (2008) Study of Texture Evolution at High Strain Rates in FCC Materials, in Applications of Texture Analysis (ed A.D. Rollett), John Wiley & Sons, Inc., Hoboken, NJ, USA

Gucsik, A., Zhang, M., Koeberl, C., Salje, E. K. H. and Redfern, S. A. T. (2004) Infrared and Raman spectra of ZrSiO_4 experimentally shocked at high pressures. *Mineralogical Magazine*, **68** (5). pp. 801-811.

Haines, J., Leger, J. M., and Bocquillon, G. (2001) Synthesis and design of superhard materials. *Annu. Rev. Mater. Res.* **31**, 1

Hanchar, J.M., Miller, C.F., Wooden, J.L., Bennet, V.C., Staude J-MG (1994) Evidence of xenoliths for a dynamic lower crust, eastern Mojave desert, *California. J Petrol* **35**:1377-1415

Hazen, R.M. and L.W.Finger (1979) Crystal structure and compressibility of zircon at high pressure. *American Mineralogist* **64**, 196-201

He, D., Shieh, S.R., and Duffy, T.S. (2004) Strength and equation of state of boron suboxide from radial x-ray diffraction in a diamond cell under nonhydrostatic compression. *Physical Review B* **70**, 184121

Heaman, L.M. and Parrish, R.R. (1991) U-Pb geochronology of accessory minerals. In L.M. Heaman and J.N. Ludden, Eds, *Applications of Radiogenic Isotope Systems to Problems in Geology*, **19**, 59-102. Mineralogical Association of Canada, Toronto.

Hemley, R. J., Ashcroft, N. W. (1998). The Revealing Role of Pressure in the Condensed Matter Sciences. *Physics Today* **51** (8): 26

Hilairer, N., Wang, Y., Sanehira, T., Merkel, S., Mei, S. (2012) Deformation of olivine under mantle conditions: An in situ high-pressure, high-temperature study using monochromatic synchrotron radiation. *Journal of Geophys. Research*, **117**, B01203

Hong, X., Chen, Z., Sengupta, A., Goncharov, A.F., Ehm, L., Duffy, T.S., Weidner, D.J. (2011) COMPRES X-ray beamlines (X17B3 and X17C) for the diamond anvil cell at the National Synchrotron Light Source. *AGU Fall Meeting Abstracts*.

Hu, J., Guo, Q., Hemley, R. J., Mao, H. (2002) X17C - The Superconducting Wiggler Beamline Dedicated for Diamond Cell Research. American Geophysical Union, Fall Meeting 2002, abstract #U11A-0022

Jocelyn, J. and Pidgeon, R.T. (1974) Examples of twinning and parallel growth in zircons from some Precambrian granites and gneisses. *Mineralogical Magazine* **39**, pp. 587-94.

Katrusiak, A., McMillan, P. (2003) High – Pressure Crystallography. Proceedings of the NATO Advances Research Workshop on High Pressure Crystallography. Erice, Italy

Kavner, A. (2007) Garnet yield strength at high pressures and implications for upper mantle and transition zone rheology. *Journal of Geophysical Research*, **112** B12207

Kavner, A., Duffy, T.S. (2001) Strength and elasticity of ringwoodite at upper mantle pressures *Geophysical Research Letters* **28** (14), 2691-2694

Kavner, A.S., Sinogeikin, V., Jeanloz, R., Bass, J. D. (2000) Equation of state and strength of natural majorite. *J. Geophys. Res.*, **105**, 5963–5971

Kavner, A., Weinberger, M. B., Shahar, A., Cumberland, R. W., Levine, J. B., Kaner, R. B., and Tolbert, S. H. (2012). Lattice strain of osmium diboride under high pressure and nonhydrostatic stress *J. Appl. Phys.* **112**, 013526

King, E.M., Barrie, C.E., and Valley, J.W. (1998) Hydrothermal alteration of oxygen isotope ratios in quartz phenocrysts, Kidd Creek mine, Ontario: Magmatic values preserved in zircon _Reply. *Geology*, **26**, 764

Kittel, C. (2005) Introduction to Solid State Physics, 8th edition ISBN 0-471-41526-X

Knittle, E., Williams, Q. (1993) High-pressure Raman spectroscopy of ZrSiO₄: Observation of the zircon to scheelite transition at 300 K. *Am Mineral* **78**:245–252

Kotzer, T. (2004) Synchrotron Radiation in the Earth and Environmental Sciences: Applications to the Petroleum Geosciences T. Canadian Light Source, University of Saskatchewan, Saskatoon

Kovaleva, E., Klötzli, U. (2013) Rejuvenation effects during plastic deformation of Zircon: geochronological implications. *Geophysical Research Abstracts* **15**, EGU2013-4181

Kusaba, K., Syono, Y., Kikuchi, M., Fukuoka, K. (1985) Shock behavior of zircon: Phase transition to scheelite structure and decomposition. *Earth Planet Sci Lett* **72**: 433–439

Leroux, H., Reimold, W.U., Koeberl, C., Hornemann, U., Doukhan, J.-C. (1999) Experimental shock deformation in zircon: a transmission electron microscopic study, *Earth and Planetary Science Letters* **169** 291–301.

Liu, L.G. (1979) High-pressure phase transformations in baddeleyite and zircon, with geophysical implications. *Earth Planet Sci Lett* **44**:390–396

Lorenzana, H.E., Bennahmias, M. and Radousky, H. (1994) Producing diamond anvil cell gaskets for ultrahigh-pressure applications using an inexpensive electric discharge machine. *Rev. Sci. Instrum.* **65** (11)

Luo W. and R Ahuja (2008) High pressure structural phase transition in zircon (ZrSiO_4) *J. Phys.: Conf. Ser.* **121** 0220014

Lutterotti, L. (2010) Total pattern fitting for the combined size-strain-stress-texture determination in thin film diffraction, *Nuclear Inst. and Methods in Physics Research, B*, **268**, 334-340

Lutterotti, L., Bortolotti, M., Ischia, G., Lonardelli, I. and Wenk, H.- R. (2007) Rietveld texture analysis from diffraction images, *Z. Kristallogr., Suppl.* **26**, 125-130

Lutterotti, L., Chateigner, D., Ferrari, S. and Ricote, J. (2004) Texture, Residual Stress and Structural Analysis of Thin Films using a Combined X-Ray Analysis, *Thin Solid Films*, **450**, 34-41

Lutterotti, L., Matthies, S., Wenk, H.-R., Schultz, A.J. and Richardson, J. (1997) Combined texture and structure analysis of deformed limestone from time-of-flight neutron diffraction spectra, *J. Appl. Phys.*, **81**[2], 594-600

Lutterotti, L., Matthies, S. and Wenk, H.-R. (1999) MAUD: a friendly Java program for material analysis using diffraction." *IUCr: Newsletter of the CPD*, **21**:14-15

Maitland, T. and Sitzman, S. (2007) Electron backscatter diffraction (EBSD) technique and materials characterization examples. *Scanning Microscopy for Nanotechnology* **XIV** 522

Malone, L., Boonsue, S., Spray, J., Wittmann, A. (2010) Zircon-reidite relations in breccias from the chesapeake bay impact structure. *41st Lunar and Planetary Science Conference*, held March 1-5, 2010 in The Woodlands, Texas. LPI Contribution No. **1533**, p.2286

Manghnani, M. H. (1987) High Pressure Research in Mineral Physics. The Akimoto Volume. Geophysical monograph 38. Mineral physics 2

Mao, H. K., Shu, F., Shen, G. Y., Hemley, R. J., Li, B. S. and Singh, A. K. (1998) Elasticity and rheology of iron above 220 GPa and the nature of the Earth's inner core. *Nature (London)* **396**, 741

Mao, H.K., Wo, Y., Hemley, R.J., Chen, L.C., Shu, J.F., Finger, J.F. (1989) X-ray diffraction to 302 gigapascals high-pressure crystal structure of cesiou iodine.

Mariani, E., Prior, D.J., McNamara, D., Pearce, M.A., Seaton, N., Seward, G., Tatham, D. and Wheeler, J. (2009) Electron back-scattered diffraction (EBSD) in the SEM: applications to microstructures in minerals and rocks and recent technological advancements. *Seminarios de la Sociedad Espanola de Mineralogia*, **5**, pp. 7–19, eds Subias, I. & Bauluz, B. Spanish Mineralogical Society.

Merkel, S. (2006) X-ray diffraction evaluation of stress in high pressure deformation experiments *J. Phys.: Condens. Matter* **18**, S949

Merkel, S., Wenk, H.R., Shu, J., Shen, G., Gillet, P., Mao, H-K. and Hemley, R.J. (2002) Deformation of polycrystalline MgO at pressures of the lower mantle. *J. Geoph. Res.* **107** (B11)

Merkel, S. and Yagi, T. (2005) X-ray transparent gasket for diamond anvil cell high pressure experiments. *Rev. Sci. Instrum.* **76**, 046109

Mitra, S. (2004) High pressure geochemistry & mineral physics: basics for planetology and geo-material science. First edition ISBN: 0 444 51266 7

Mittal, R., Chaplot, S.L., Preyoshi, B.P. and Choudhury, N. (2007) Lattice dynamics and high pressure stability of zircon structured compounds. *Journal of Physics: Conference Series* **92** 012143.

Miyagi, L., Merkel, S., Yagi, T., Sata, N., Ohishi, Y., Wenk, H.R. (2009) Diamond anvil cell deformation of CaSiO_3 perovskite up to 49GPa. *Physics of the Earth and Planetary Interiors* **171**, 159-164

Moser, D.E., Cupelli, C.L., Barker, I.R., Flowers, R.M., Bowman, J.R., Wooden, J. and Hart, J.R. (2011) New zircon shock phenomena and their use for dating and reconstruction of large impact structures revealed by electron nanobeam (EBSD, CL, EDS) and isotopic U–Pb and (U–Th)/He analysis of the Vredefort dome. *Can. J. Earth Sci.* **48**: 117–139

Nielsen, R. (2005) Zirconium and Zirconium Compounds, Ullmann's Encyclopedia of Industrial Chemistry. Wiley-VCH, Weinheim. doi:10.1002/14356007.a28_543

Oger, P.M., Daniel, I. and Picard, A. (2005) Development of a low-pressure diamond anvil cell and analytical tools to monitor microbial activities in situ under controlled P and T. *BBA Proteomics* **1764**:434-442

Ono S., Funakoshi K., Nakajima Y., Tange Y., Katsura T. (2004) Phase transition of zircon at high P-T conditions. *Contrib. Mineral. Petrol.*, **147** 505-509.

Ono, S., Tange, Y., Katayama, I., and Kikegawa, T. (2004) Equation of state of ZrSiO_4 phases in the upper mantle. *American mineralogist* **89**,185-188

Paszkowicz, W., Ermakova, O., Lopez-Solano, J., Mujica, A., Munos, A., Minikayev, R., Lathe, C., Gierlotka, S., Nikolaenko, I., Dabkowska, H. (2014) Equation of state of zircon- and scheelite-type dysprosium orthovanadates: a combined experimental and theoretical study. *J. Phys.: Condens. Matter* **26** 025401

Piazolo, S., Austrheim, H., and Whitehouse, M. (2012) Brittle-ductile microfabrics in naturally deformed zircon: Deformation mechanisms and consequences for U-Pb dating. *Am. Mineral.* **97**, 1544–1563

Pidgeon, R.T., Nemchin, A.A., Kamo, S.L. (2011) Comparison of structures in zircons from lunar and terrestrial impactites. *Can.J.Earth Sci.* **48**: 107-116.

Quartieri, S. (2014) Synchrotron Radiation. Book. Synchrotron radiation in the Earth Science. *Springer-Verlag Berlin Heidelberg* pp.641-660

Raterron, P., Merkel, S. and Holyoke, C.W. III (2013) Axial temperature gradient and stress measurements in the deformation-DIA cell using alumina pistons. *Rev Sci Instrum.* **84**(4):043906

Reid, A.F., Ringwood, A.E. (1969) Newly observed high pressure transformations in Mn_3O_4 , $CaAl_2O_4$ and $ZrSiO_4$. *Earth Planet Sci Lett* **6**:205–208

Reddy, S.M., Timms, N.E., Trimby, P., Kinni P.D., Burchan, C., Blake, K. (2006) Crystal-plastic deformation of zircon: A defect in assumption of chemical robustness. *Geology* **34**(4) p. 257-260

Reddy, S.M., Timms, N.E., Pantleon, W., Trimby, P. (2007) Quantative characterization of plastic deformation of zircon and geological implications. *Contributions to Mineralogy and Petrology* **153** (6), pp 625-645

Reddy, S.M., Timms, N.E., Hamilton, P.J., Smyth, H.R. (2009) Deformation-related microstructures in magmatic zircon and implication for diffusion. *Contributions to Mineralogy and Petrology* **157** (2), pp 231-244

Schwarzer, R. (2015) An Introduction to EBSD Backscatter Kikuchi Diffraction in the Scanning Electron Microscope ("BKD", "ACOM/SEM", "Orientation Microscopy") - www.ebsd.info

Scott, H. P., Williams, Q., Knittle E. (2002) Ultralow Compressibility Silicate without Highly Coordinated Silicon. *Phys. Rev. Lett.* **88** 15506

Seal, M. (1984) Diamond anvils. *High Temp. – High Press* **16**, 573-579

Shieh, S. R., Duffy, T. S. and Li, B. (2002), Strength and elasticity of SiO_2 across the stishovite- $CaCl_2$ - type structural phase boundary, *Phys. Rev. Lett.* **89**, 255507.

Shieh, S. R., Duffy, T.S., Shen, G. (2004), Elasticity and strength of calcium silicate perovskite at lower mantle pressures, *Phys. Earth Planet. Inter.*, **143-144**, 93– 105.

Singh, A. K. (1993) The lattice strains in a specimen (cubic system) compressed nonhydrostatically in an opposed anvil device. *J. Appl. Phys.* **73**, 4278

Singh, A. K. (2004) X-ray diffraction from solids under nonhydrostatic compression—some recent studies. *J. Phys. Chem. Solids* **65**, 1589

Singh, A. K., Balasingh, C., Mao, H. K., Hemley, R. J. and Shu, J. F. (1998) Analysis of lattice strains measured under nonhydrostatic pressure. *J. Appl. Phys.* **83**, 7567

Sokolov, A. A. and Ternov, I. M. (1967) Synchrotron Radiation. *Soviet Physics Journal. Izvestiya VUZ. Fizika*, **10**, 66-82, 1967

Takahashi, T., Liu, L.-G. (1970) Compression of ferromagnesian garnets and the effect of solid solutions on the bulk modulus. *J. Geophys. Res.* **75** (29)

Tange, Y. and Takashi, E. (2002) Stability of zircon at high-pressure and temperature. Special Issue of the Review of High Pressure Science and Technology 12:50

Timms, N.E., Reddy, S.M., Healy, D., Nemchin, A.A., Grange, M.L., Pidgeon, R.T., and Hart, R. (2012) Resolution of impact-related microstructures in lunar zircon: A shock-deformation mechanism map. *Meteoritics & Planetary Science* **47** (1)

Tommaseo, C.E., Devine, J., Merkel, S., Speziale, S., Wenk, H.R. (2006) Texture development and elastic stresses in magnesiowüstite at high pressure. *Phys Chem Minerals* **33**:84-97

Tkachenko, K., Brazhkin, V.V., Tsiok, O.B., Dove, M.T., Salje, E.K. (2007) Pressure-induced structural transformation in radiation-amorphized zircon. *Phys Rev Lett* **98**(13):135502

Uchida, T., Funamori, N., Ohtani, T. and Yagi, T. (1996) Differential stress of MgO and Mg₂SiO₄ under uniaxial stress field: variation with pressure, temperature, and phase transition., Proceedings of the 15th AIRAPT conference, Warsaw, 183– 185.

Valley, J.W., Cavosie, A.J., Ushikubo, T., Reinhard, D.A., Lawrence, D.A., Larson, D.J., Clifton, P.H., Kelly, T.K., Wilde, S.A., Moser, D.E. & Spicuzza, M.J. (2014) Hadean age for a post-magma-ocean zircon confirmed by atom-probe tomography. *Nature Geoscience* **7**, 219–223

Van Westrenen W., Frank M.R., Fei Y., Hanchar J.M., Finch R.J., Zha C-S (2003) In situ measurements of the compressibility of pure and trace element doped synthetic zircon. Abstract, EUG-EGS-AGU meeting, Nice, France.

Van Westrenen W., Frank M.R., Hanchar J.M., Fei Y., Finch R.J., Zha C-S (2004) In situ determination of the compressibility of synthetic pure zircon (ZrSiO₄) and the onset of the zircon-reidite phase transition. *American Mineralogist* **89**, 197-203.

Weidner, D. J., Davis, L.L.M., and Chen J. (2004) Effect of plasticity on elastic modulus measurements *Geophysical Research Letters* **31** L06621

Wenk, H.-R., Matthies, S. and Lutterotti, L. (1994) Texture analysis from diffraction spectra", *Mater. Sci. Forum*, 157-162, 473-480

Wittmann A., Goderis S., Claeys P., Elburg M., Vanhaecke F., Zaiss J., Ravizza G., Deutsch (2009) A. Depositional Record of Pristine Impactites and Traces of the Projectile in El'gygytyn Crater. *GSA Spec. Pap.* **458**, 349-396.

Xie, M., Mohammadi, R., Mao, M., Armentrout, M. M., Kavner, A., Kaner, R.B., and Tolbert, S.H. (2012). Exploring the high-pressure behavior of superhard tungsten tetraboride *Phys. Rev. B* **85**, 064118

Xie, M., Mohammadi, R., Turner, C.L., Kaner, R.B., Kavner, A., and Tolbert, S.H. (2014) Lattice stress states of superhard tungsten tetraboride from radial x-ray diffraction under nonhydrostatic compression. *Phys. Rev. B* **90**, 104104.

Xiong, L., Liu, J., Bai, L., Li, Y., Lin, C., He, D., Peng, F. and Lin, J.F. (2013) Radial X-ray diffraction of tungsten tetraboride to 86 GPa under nonhydrostatic compression. *Journal of Applied Physics* **113**, 033507

Xu, J., Mao, H., Hemley, R., and Hines, E. (2002) The moissanite anvil cell: a new tool for high-pressure research. *J. Phys.: Condens. Matter* **14** 11543

Xu, J., Yeh, S., Yen, J. and Huang, E. (1996) Raman Study of D₂O at High Pressures in a Cubic Zirconia Anvil Cell *J. Raman Spectrosc.* **27** 823

Appendix 1. Differential Stress

Table A1.1. Differential stress (t) of each (hkl) plane for zircon at different pressures.

Pressure, GPa	$t101$, GPa	$t200$, GPa	$t112$, GPa	$t013$, GPa	$t312$, GPa	$t213$, GPa
0	0	0	0			
1.17	0.383291	0.338054	0.17457			
3.89	0.664745	0.475996	0.768777			
4.25	0.68239	0.732311	0.834823			
6.43	1.174544	0.777281	1.420508			
7.39	1.27677	0.790968	1.702593	1.140253		0.612812782
10.68	1.819219	1.325499	1.973578	1.758596		1.128340263
13.38	2.296013	1.62436	2.317294	1.933031		1.831775882
14.65	2.53843	1.783696	2.787533	2.495887		2.039075931
14.95	2.498374	1.737377	2.818858			
15.6	2.949683	1.912344	3.28614			
16.9	2.857902	2.152343	3.252744	2.516824		2.221792303
17.4	3.441728	2.088029	3.535521			
18.02	3.144321	2.12765	3.373755	2.215753	3.733468	
18.7	3.393834	2.21997	3.549826	2.919259	3.877557	
20.56	3.423518	2.424181	3.733308	2.67791	4.079419	
21.11	3.532194	2.439264	3.836429	3.103899	4.197476	
22.04	3.665615	2.445319	4.027918	3.163537	4.201239	
23.45	3.896773	2.494593			4.334221	
24.9	4.097313	2.431136	4.404897		4.662615	
26.14	4.153961	2.550208	4.667751		4.644545	
27.7	4.122561	2.651289	4.832486		5.601822	
29.95	4.433421	2.743427	5.45003		5.358661	

Table A1.2. Differential stress and shear stress ratio for each observed (*hkl*) plane at different pressures.

Pressure,	Shear stress,						
GPa	GPa	t/G(101)	t/G(200)	t/G(112)	t/G(013)	t/G(312)	t/G(213)
0	48	0	0	0			
1.17	49.17	0.007795	0.006911	0.003569021			
3.89	51.89	0.013025	0.009327	0.015063962			
4.25	52.25	0.013298	0.014271	0.016268591			
6.43	54.43	0.022155	0.014661	0.026794258			
7.39	55.39	0.023748	0.014712	0.031667783	0.021208		0.01139816
10.68	58.68	0.032296	0.023531	0.035035751	0.031219		0.02003075
13.38	61.38	0.039291	0.027797	0.039654975	0.033079		0.03134649
14.65	62.65	0.042715	0.030015	0.04690685	0.041999		0.03431228
14.95	62.95	0.041876	0.029121	0.04724791			
15.6	63.6	0.049024	0.031783	0.054616069			
16.9	64.9	0.046711	0.035179	0.053165056	0.041137		0.03631448
17.4	65.4	0.055898	0.033912	0.057420925			
18.02	66.02	0.050555	0.034209	0.054243924	0.035625	0.060027	
18.7	66.7	0.054539	0.035675	0.057046211	0.046913	0.062313	
20.56	68.56	0.053462	0.037856	0.058299419	0.041818	0.063704	
21.11	69.11	0.054792	0.037838	0.059511078	0.048148	0.065112	
22.04	70.04	0.056229	0.03751	0.061786223	0.048527	0.064445	
23.45	71.45	0.058783	0.037631			0.065382	
24.9	72.9	0.060771	0.036059	0.065333228		0.069156	
26.14	74.14	0.06074	0.03729	0.068252746		0.067913	
27.7	75.7	0.059227	0.03809	0.069426283		0.080479	
29.95	77.95	0.062127	0.038444	0.076372672		0.075092	

Appendix 2. Texture analysis of zircon powder using Material Analysis Using Diffraction software (MAUD).

Starting MAUD

The resulting .esg files for each pattern were imputed into the MAUD software. Further analysis was done using almost all the 36 spectra for each set. Firstly, some spectra that had anomalous intensities were removed from the list. Secondly, calibration of instrumental parameters was done by standard, collected at the time of the experiment. In the current study, CeO₂ was used as a standard. The two theta range between 4.5 and 13 degrees was chosen as it included enough peaks for refinement and it was the best representative interval of further zircon data.

A diffraction instrument was manually set according to the information about the sample to detector distance, wavelength, detector tilt and other parameters collected at NSLS and later refined by fit2d software. The instrumental set up was:

1. Intensity Calibration was set as no calibration for CeO₂ and later changed to Polynomial Angular Intensity for actual analysis.
2. For angular calibration, Flat Image Transmission was chosen. In options, detector distance was set according to fit2d information (286.9201mm and 286.65 mm for different sets respectively)
3. For geometry, Image 2D with Monochromator was chosen.
4. Measurement was set as 2 theta.
5. Synchrotron was chosen as a source with a specific wavelength that corresponded to the one recorded at NSLS.
6. Detector: Scintillation with no options.
7. Instrument broadening was set as Caglioti, but both of the coefficients were set as zero.

The average profile for CeO_2 was calculated using information from open-access collection of crystal structures of organic, inorganic, metal-organic compounds and minerals (COD database).

Refinement of the standard is an essential part of this research as it allows us to get some precise information about the initial set up with smaller errors. So, the refinement of the standard provided us with the specific instruments' values that were later applied to actual data.

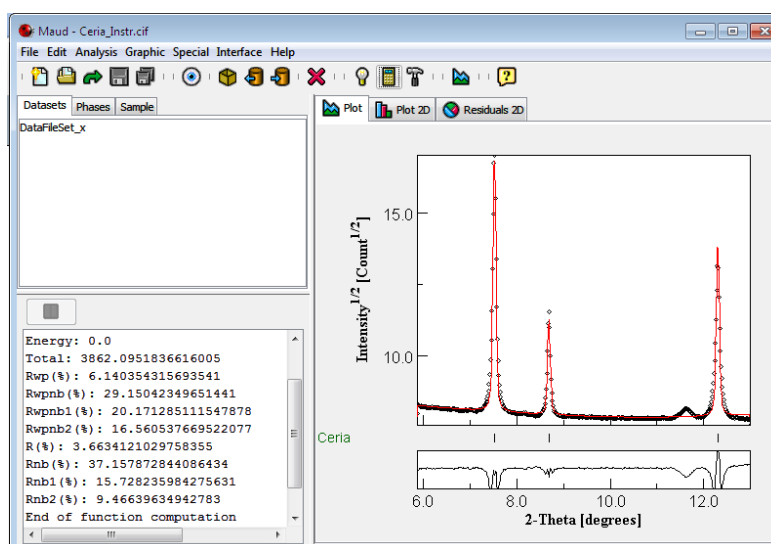


Figure A2.1 CeO_2 standard after full refinement in MAUD software. Black color is initial collected data, red- calculated (refined) spectra.

After perfect fit of measured and refined spectra was obtained (Figure A2.1), the actual analysis was initiated.

MAUD Refinement of the Zircon Diffraction Data

Zircon .esg files previously prepared by fi2dmaud were input into MAUD. Instrumental parameters were refined using the standard. Spectra were fitted using the zircon.cif file obtained from the MAUD database. The gasket's and pressure standard's spectra were fit with Be, BeO and Au (.cif files were downloaded from COD database), respectively.

The full refinement of the radial X-ray diffraction data of the zircon was described as follows (Figure A2.2): Firstly, spectra with anomalous intensities were removed from analysis to avoid “weird” peaks. Secondly, backgrounds and intensities were fitted several times to achieve the best fit. Thirdly, the linewidth of peaks was corrected after the refinement of microstrain and crystalline size with the isotropic model for each phase. Stress applied to Au was assumed triaxial with $2\sigma_{11}=2\sigma_{22}=-\sigma_{33}$ and refined using an isotropic model based on Young’s modulus and Poisson ratio. Values for σ_{11} and σ_{12} were considered to be fixed as -0.5, σ_{33} was refined by itself, later with cell parameters and beam centre. Zircon stress and strain was fit with Radial diffraction in DAC strain model. Strike angle α and dip angle β were related to the DAC compression axis, which were set as 90° and 0° , respectively. $Q(hkl)$ were obtained for individual planes (101, 200, 112, 013, 312, 213) using Singh’s theory (Singh *et al.*, 1998). Texture was applied to both zircon and Au phases. The E-WIMV model was used. Fiber and 4-fold and fiber symmetry were applied with 10-15% of Gauss filter for ODF.

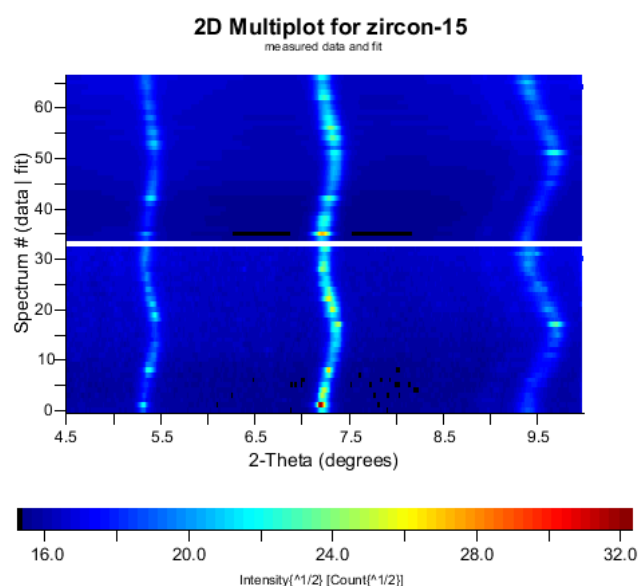
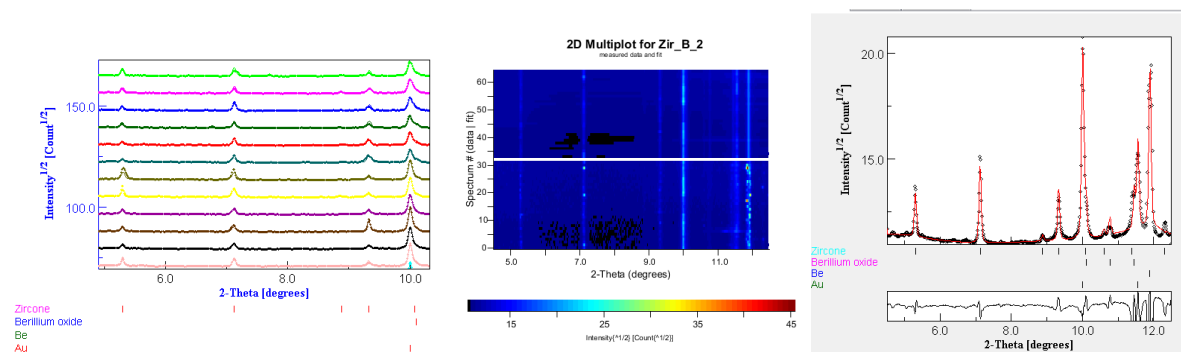


Figure A2.2 Multiplot for zircon obtained after refinement using MAUD software. Bottom- initial data, top- result (calculated).

Zircon_3rd dataset_2pattern_Pressure_1bar



Texture index 1.4374 Not normalized 6.4968314816

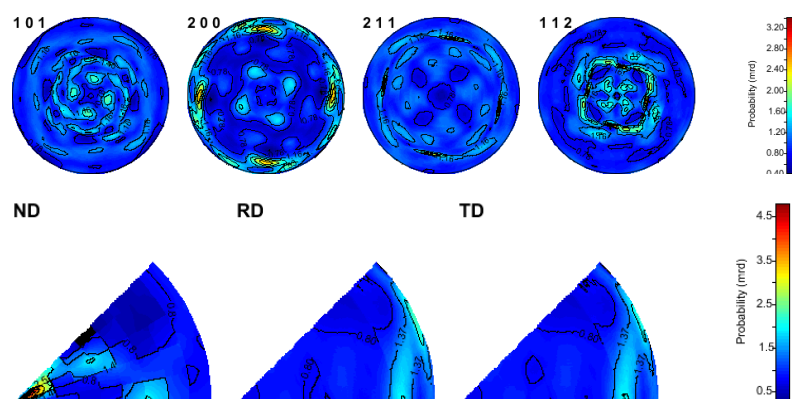
Zircon- 4-fold symmetry-10% Gaussian smooth ODF. *Not normalized*

Reconstructed intensity. Pole figures intensity range:

-calculated: min= 0.4007817365094, max= 3.425178011028

Inverse pole figures. Range:

-calculated: min= 0.2201918374051, max= 4.82191676451766



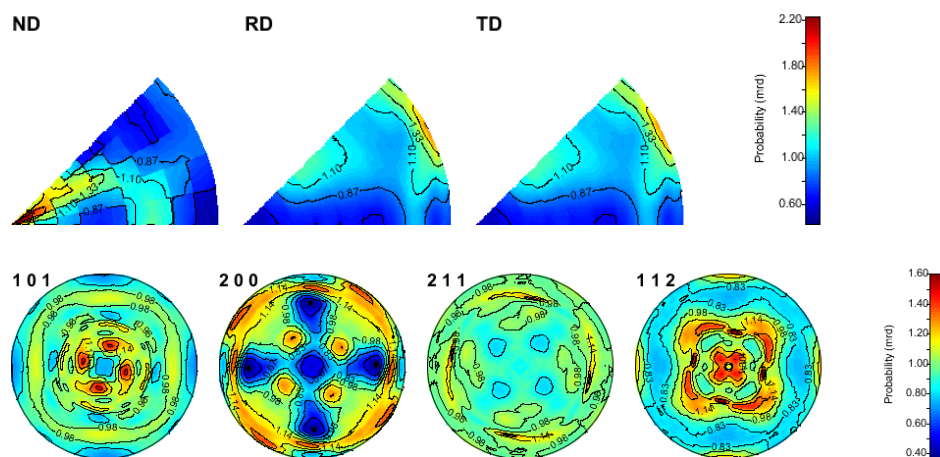
Zircon- 4-fold symmetry-10% Gaussian smooth ODF. *Normalized*

Reconstructed intensity. Pole figures intensity range:

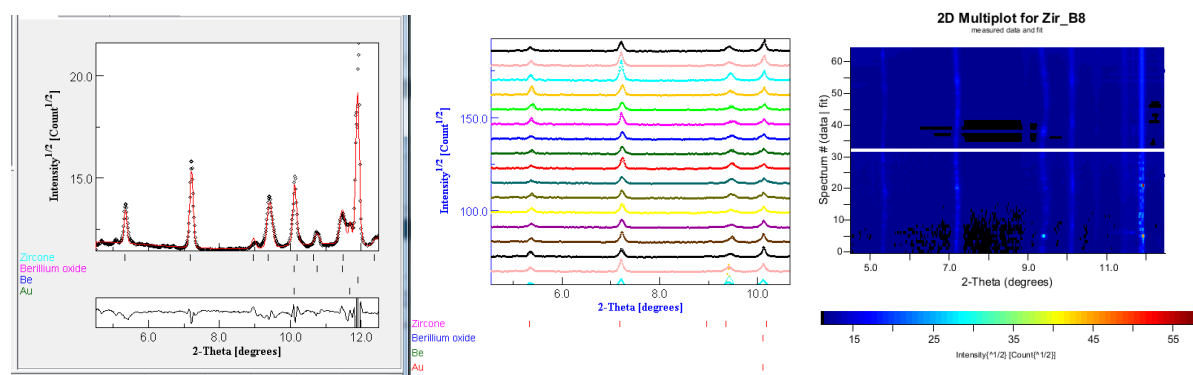
-calculated: min= 0.36155904432, max= 1.60797770422

Inverse pole figures. Range:

-calculated: min=0.01942285055, max= 2.2368356194



Zircon_3rd dataset_8pattern_Pressure_7GPa



Texture index 1.60263477509 (norm)/6.6838611010526(not norm)

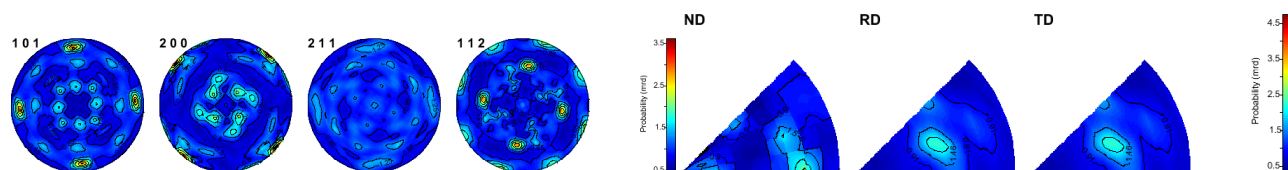
Zircon- 4-fiber symmetry-11% Gaussian smooth ODF. *Not normalized*

Reconstructed intensity. Pole figures intensity range:

-calculated: min= 0.45038882176, max= 3.628895911082

Inverse pole figures. Range:

-calculated: min=0.353173493414, max= 4.77323946876



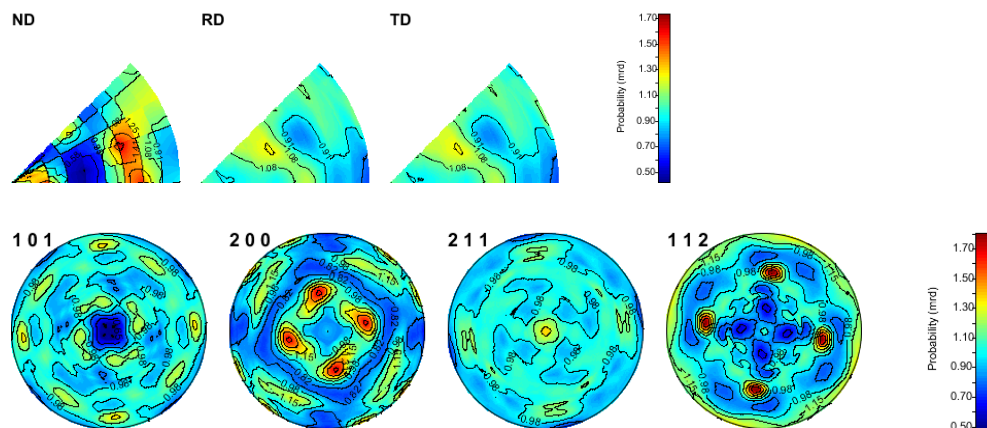
Zircon- 4-fiber symmetry-11% Gaussian smooth ODF. *Normalized* (inverse figure is almost the same as the one with fiber symmetry)

Reconstructed intensity. Pole figures intensity range:

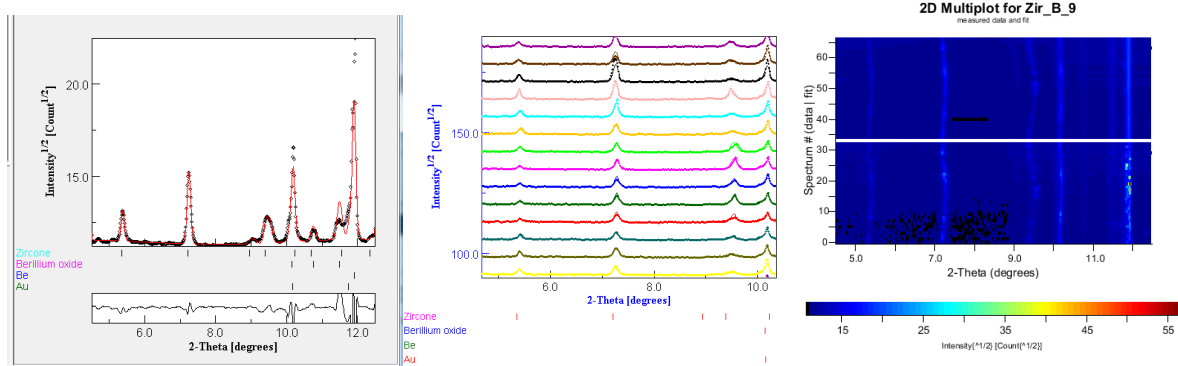
-calculated: min= 0.483131781796, max= 1.8127061245949

Inverse pole figures. Range:

-calculated: min=0.41543756297556, max= 1.7427376054323



Zircon_3rd dataset_9pattern_Pressure_11GPa

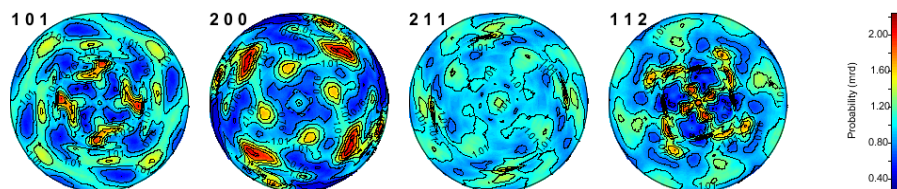


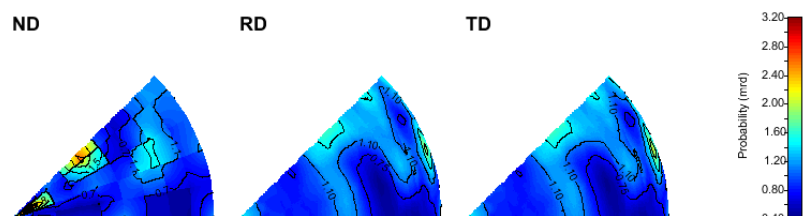
Texture index 3.0968929680(norm)/7.2698083877(not norm)

Zircon- 4-fold symmetry-10% Gaussian smooth ODF. *Not normalized*

Reconstructed intensity. Pole figures intensity range: min= 0.25625275007, max=2.2553474116938

Inverse pole figures. Range: : min= 0.39313565311, max= 3.22834319049

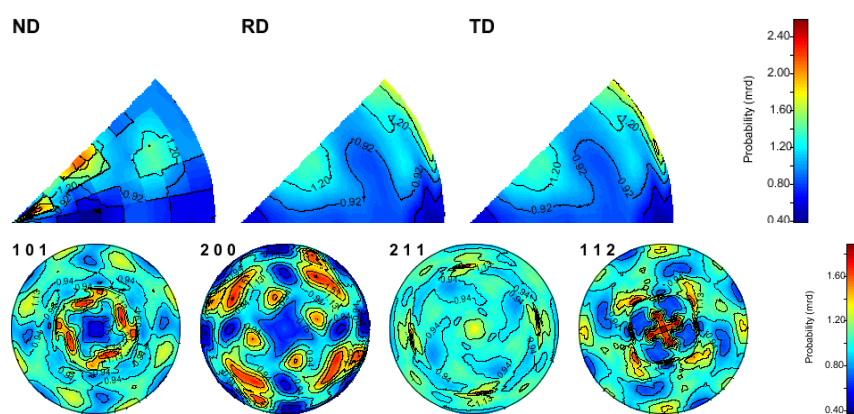




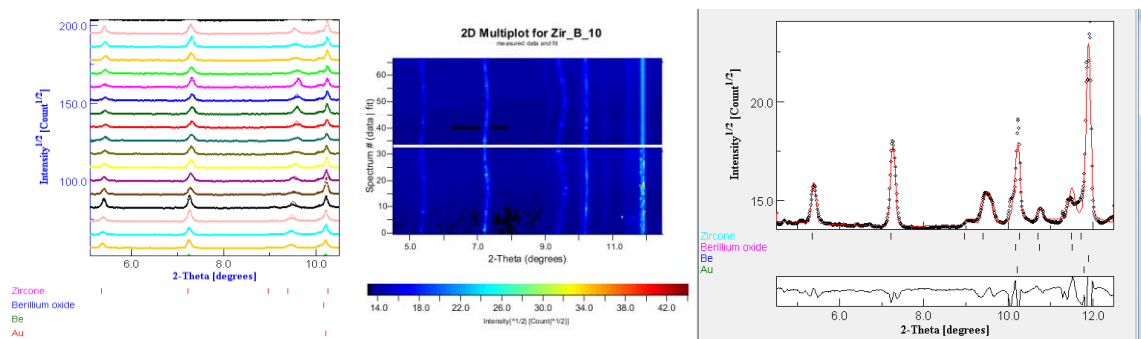
Zircon- 4-fold symmetry-10% Gaussian smooth ODF. **Normalized**

Reconstructed intensity. Pole figures intensity range: min= 0.36349913656, max= 1.89580459965

Inverse pole figures. Range: : min= 0.36672927090359, max= 2.594375380344



Zircon_3rd dataset_10pattern_Pressure_14GPa

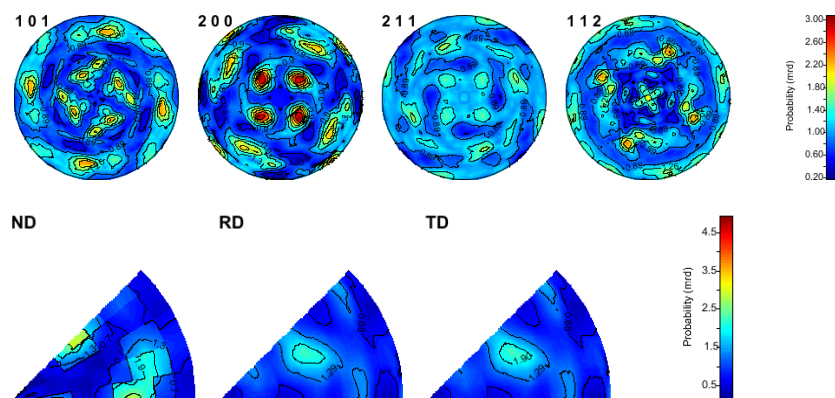


Texture index 1.32031611848 (norm)/12.5969585626(not norm)

Zircon- 4-fold symmetry-10% Gaussian smooth ODF. **Not normalized**

Reconstructed intensity. Pole figures intensity range: min= 0.15753689913, max=3.0881631414

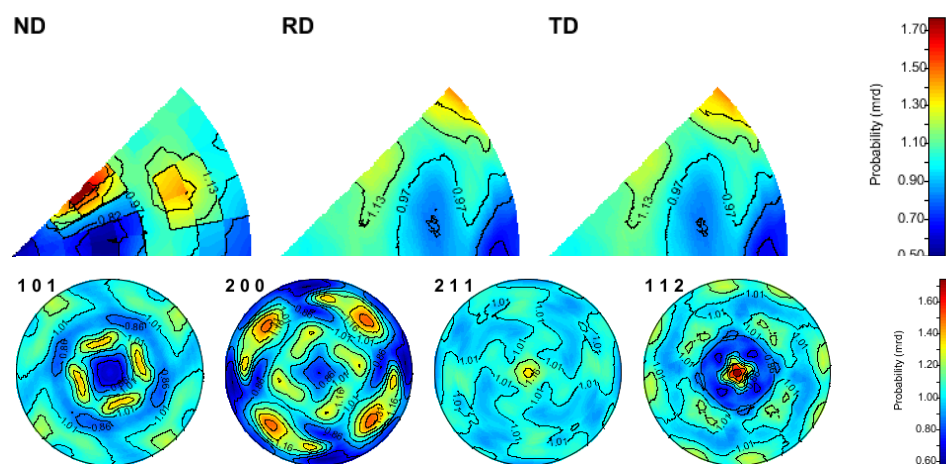
Inverse pole figures. Range: : min= 0.064143586623, max= 4.95441977435



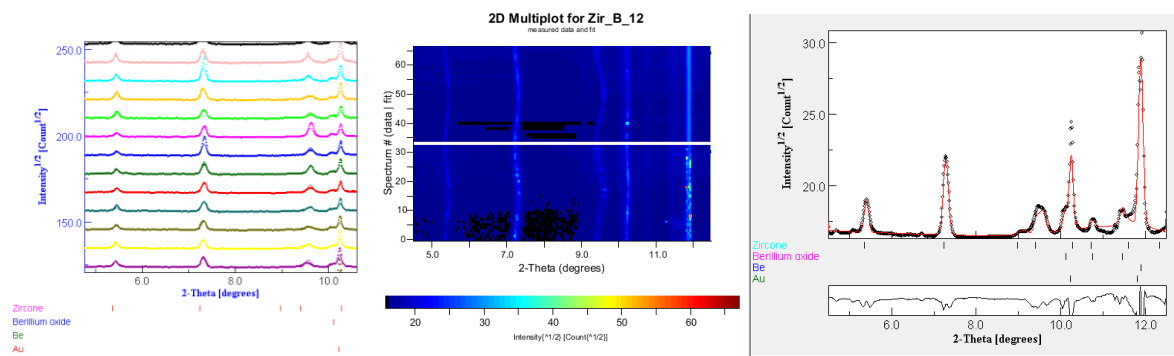
Zircon- 4-fold symmetry-10% Gaussian smooth ODF. *Normalized*

Reconstructed intensity. Pole figures intensity range: min= 0.571410706335, max= 1.74569327570

Inverse pole figures. Range: min= 0.49623006888, max= 1.77235648994



Zircon_3rd dataset_12pattern_Pressure_15GPa

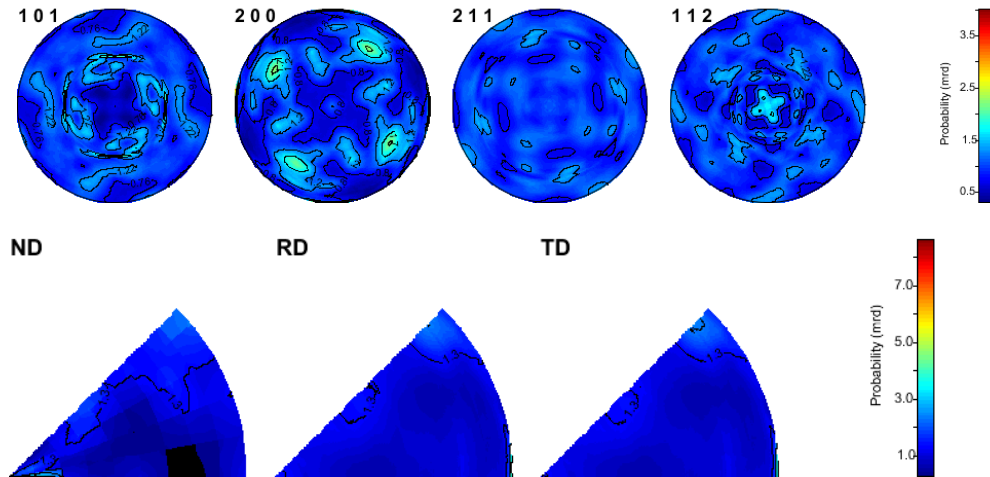


Texture index 1.6167560526 (norm)/5.550647326(not norm)

Zircon- 4-fold symmetry-10% Gaussian smooth ODF. *Not normalized*

Reconstructed intensity. Pole figures intensity range: min= 0.288775161129, max=4.03066275742

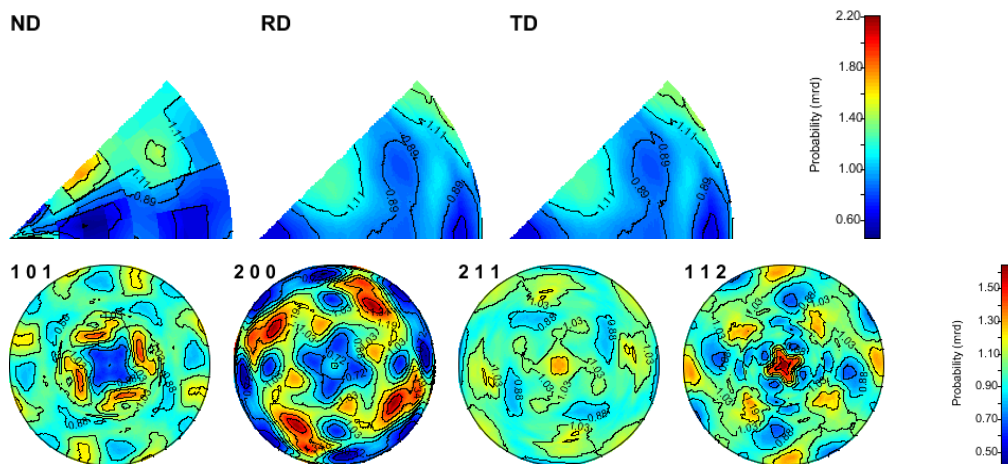
Inverse pole figures. Range: : min= 0.23625185067, max= 8.66614192866



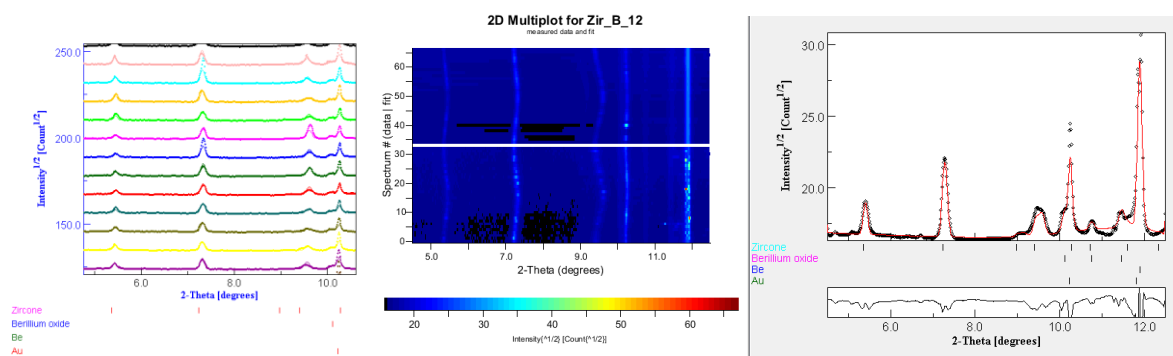
Zircon- 4-fold symmetry-10% Gaussian smooth ODF. *Normalized*

Reconstructed intensity. Pole figures intensity range: min= 0.41296281952, max= 1.65181813464

Inverse pole figures. Range: min= 0.4489717496, max= 2.2209373644



Zircon_3rd dataset_12pattern_Pressure_15GPa

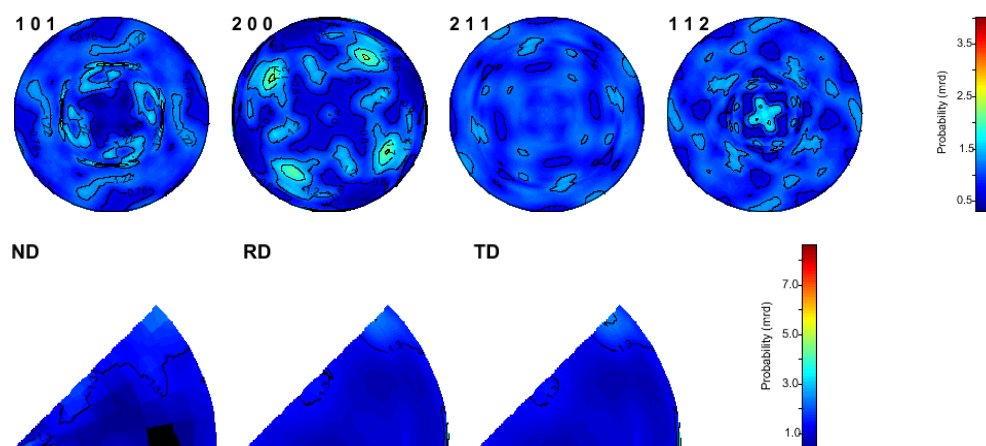


Texture index 1.6167560526 (norm)/5.550647326(not norm)

Zircon- 4-fold symmetry-10% Gaussian smooth ODF. *Not normalized*

Reconstructed intensity. Pole figures intensity range: min= 0.288775161129, max=4.03066275742

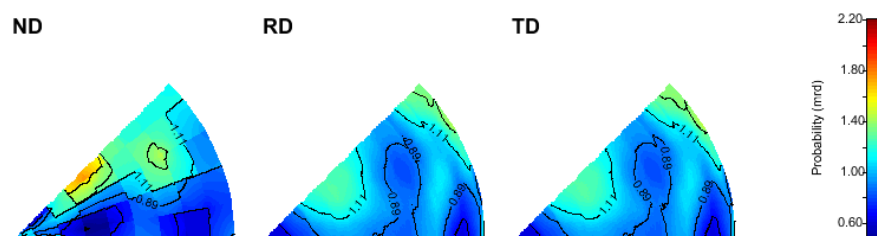
Inverse pole figures. Range: : min= 0.23625185067, max= 8.66614192866

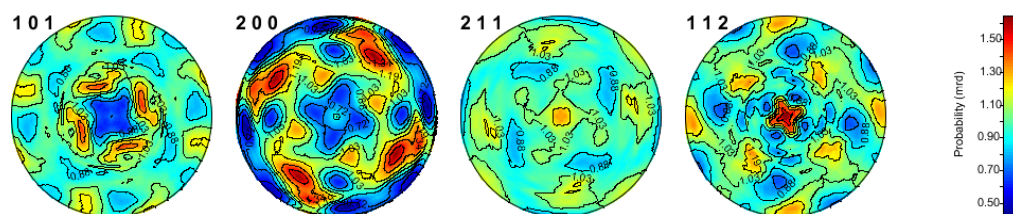


Zircon- 4-fold symmetry-10% Gaussian smooth ODF. *Normalized*

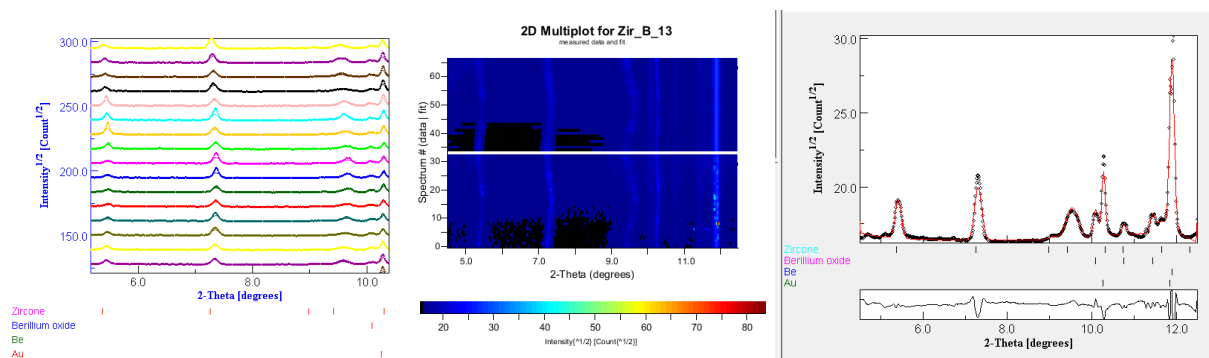
Reconstructed intensity. Pole figures intensity range: min= 0.41296281952, max= 1.65181813464

Inverse pole figures. Range: min= 0.4489717496, max= 2.2209373644





Zircon_3rd dataset_13pattern_Pressure_16.9GPa

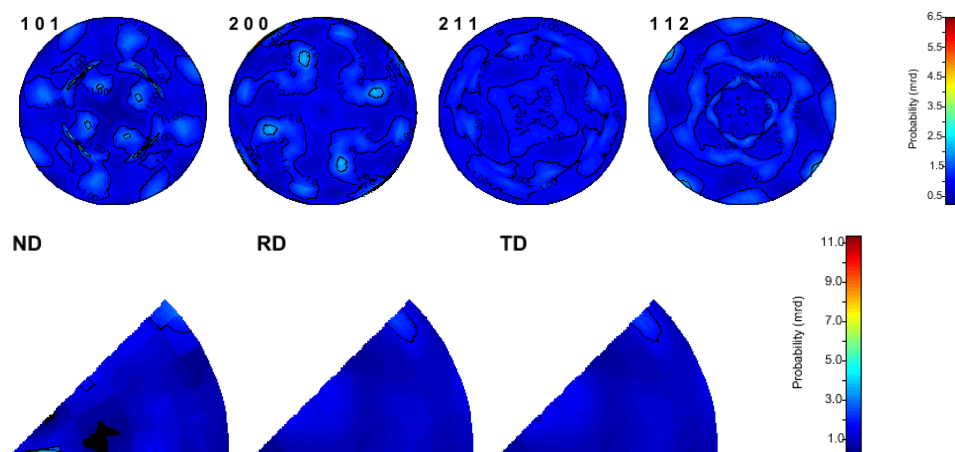


Texture index 1.834878473953 (norm)/7.69435198(not norm)

Zircon- 4-fold symmetry-10% Gaussian smooth ODF. *Not normalized*

Reconstructed intensity. Pole figures intensity range: min= 0.20582774541, max=6.5240582191

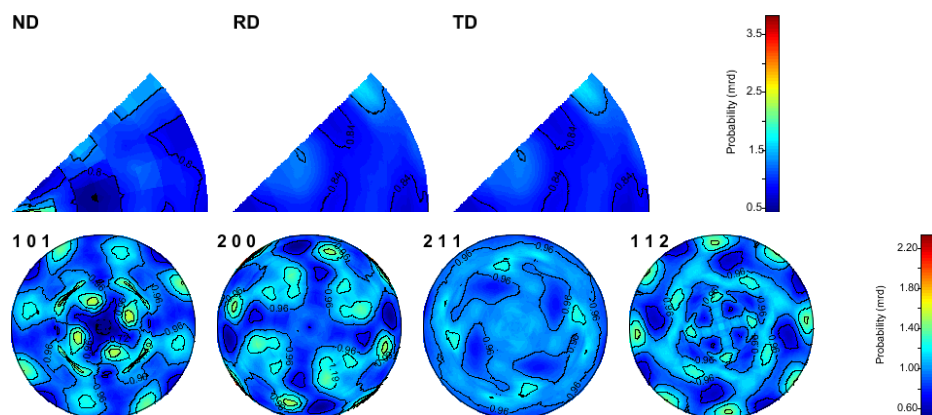
Inverse pole figures. Range: : min= 0.2417294866, max= 11.395439320



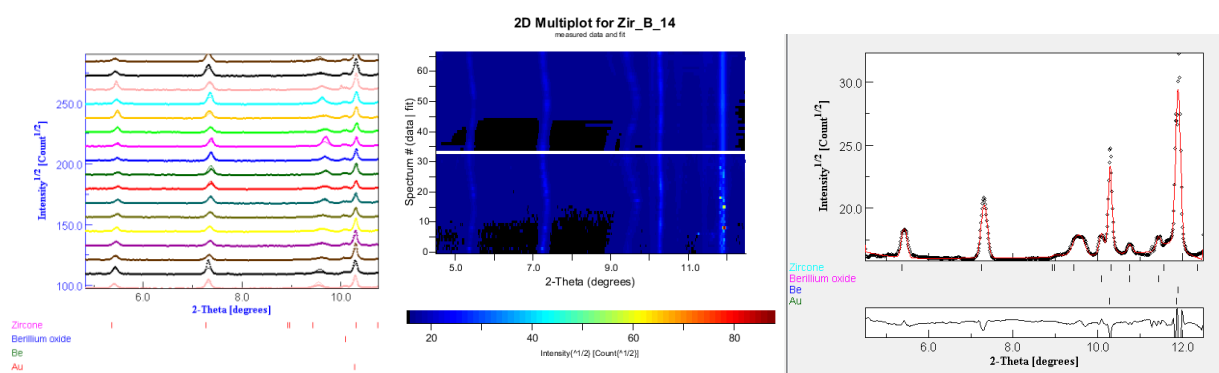
Zircon- 4-fold symmetry-10% Gaussian smooth ODF. *Normalized*

Reconstructed intensity. Pole figures intensity range: min= 0.4928540528, max= 2.3445375018

Inverse pole figures. Range: min= 0.408944766185, max= 3.8401595405



Zircon_3rd dataset_14pattern_Pressure_17.39GPa

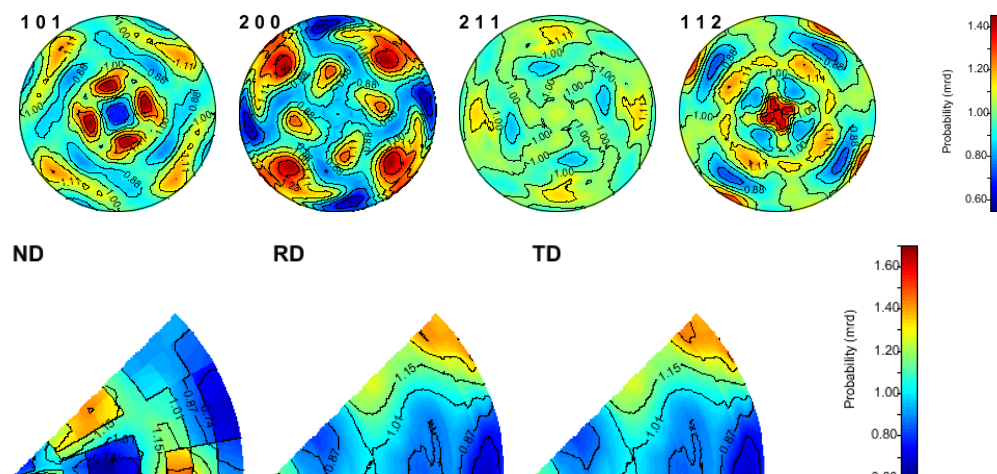


Texture index 1.30788366489 (norm)/7.0230751360011(not norm)

Zircon- 4-fold symmetry-10% Gaussian smooth ODF. *Not normalized*

Reconstructed intensity. Pole figures intensity range: min=0.54019741402, max=1.45771566202

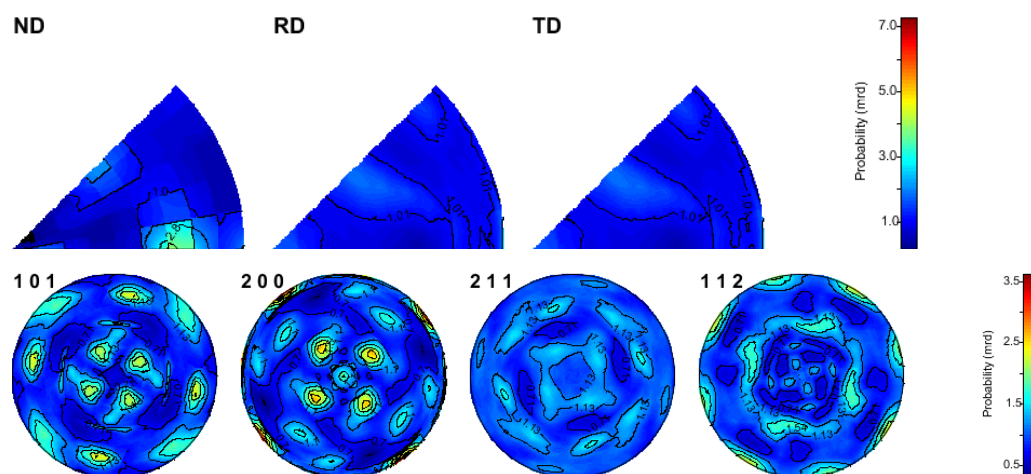
Inverse pole figures. Range: : min=0.59856738558, max= 1.70324228827



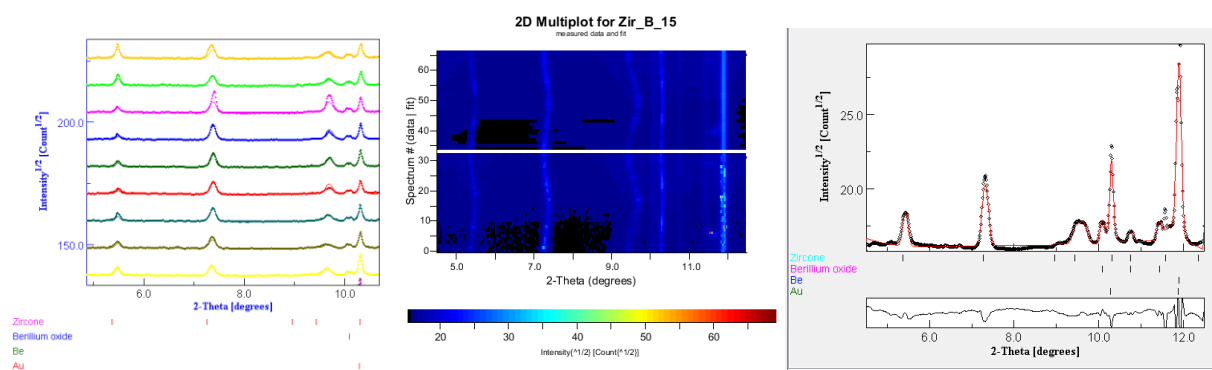
Zircon- 4-fold symmetry-10% Gaussian smooth ODF. *Normalized*

Reconstructed intensity. Pole figures intensity range: min= 0.2916409722, max= 3.6310960358

Inverse pole figures. Range: min= 0.11648655388, max= 7.30342420687



Zircon_3rd dataset_15pattern_Pressure_18.29 GPa

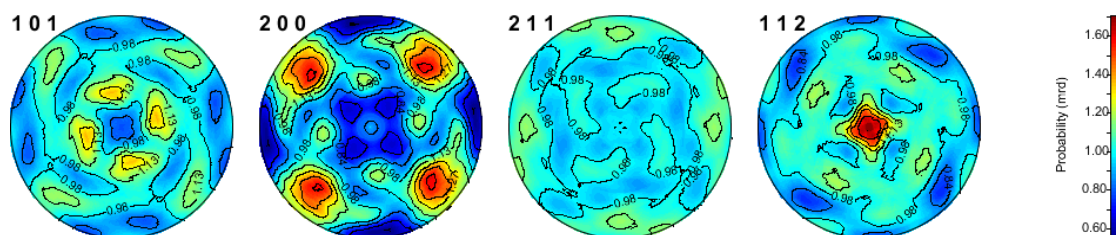


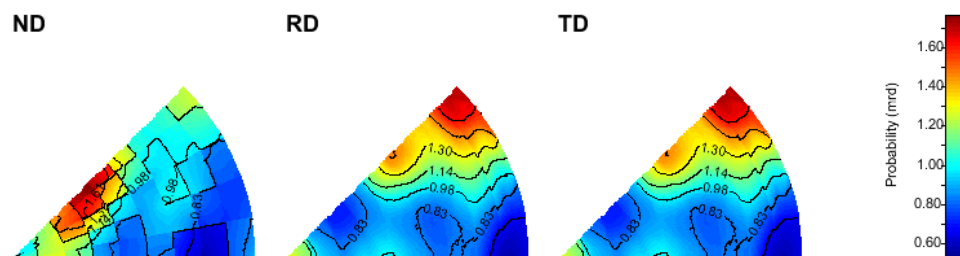
Texture index 1.31078336980 (norm)/13.42461436056(not norm)

Zircon- 4-fold symmetry-10% Gaussian smooth ODF. *normalized*

Reconstructed intensity. Pole figures intensity range: min=0.5431536388, max=1.71264700568

Inverse pole figures. Range: : min=0.5140531029041, max1.76922169819

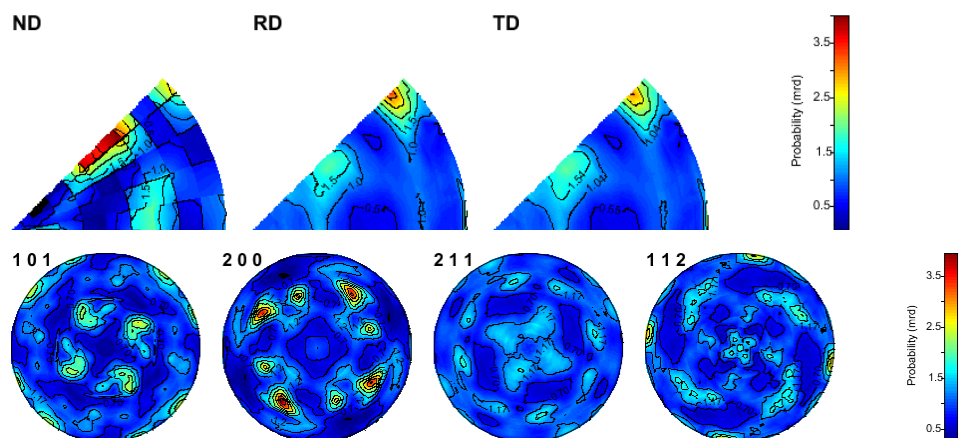




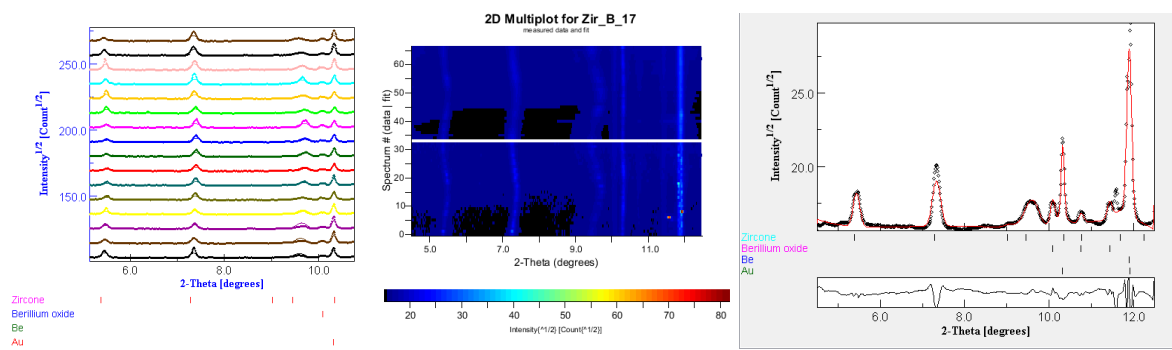
Zircon- 4-fold symmetry-10% Gaussian smooth ODF. Not *Normalized*

Reconstructed intensity. Pole figures intensity range: min= 0.236130588462, max=3.958552567597

Inverse pole figures. Range: min= 0.049476304517, max= 4.01868465211



Zircon_3rd dataset_17pattern_Pressure_20.56 GPa

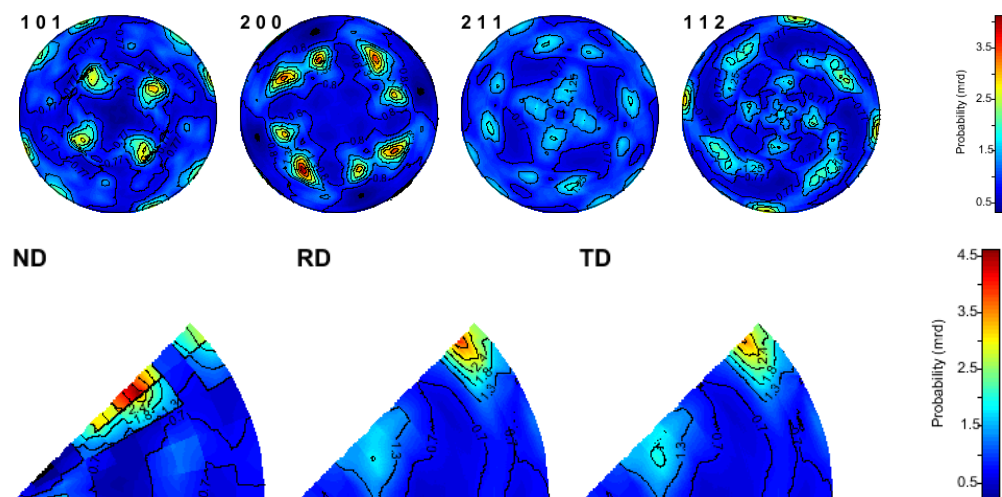


Texture index 1.204150734129 (norm)/12.6667808876(not norm)

Zircon- 4-fold symmetry-10% Gaussian smooth ODF. *Not normalized*

Reconstructed intensity. Pole figures intensity range: min= 0.289183473, max=4.1471748059

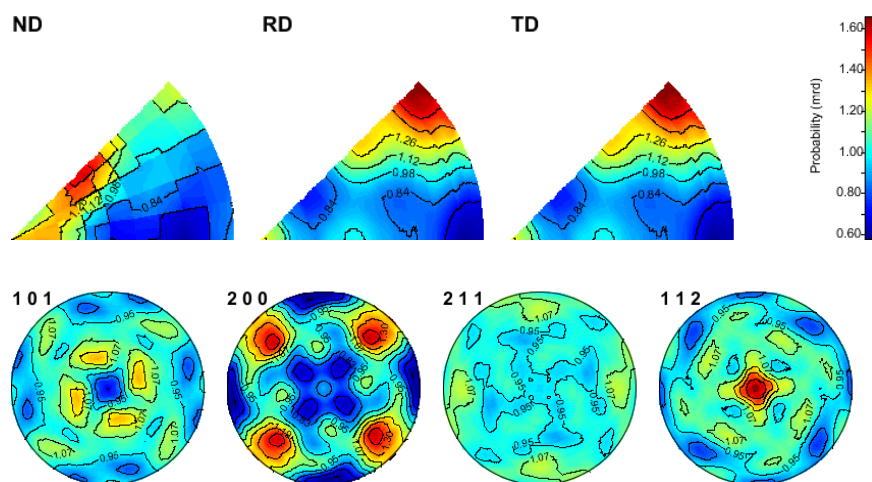
Inverse pole figures. Range: : min= 0.132207857041, max= 4.6448325523



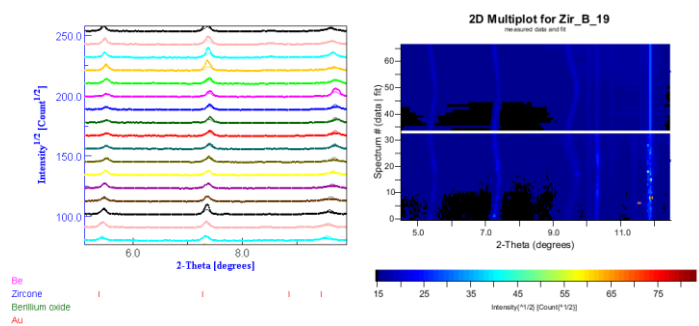
Zircon- 4-fold symmetry-10% Gaussian smooth ODF. *Normalized*

Reconstructed intensity. Pole figures intensity range: min= 0.59749022999, max= 1.53945418254

Inverse pole figures. Range: min= 0.571286834, max= 1.6655165828



Zircon_3rd dataset_19pattern_Pressure_22GPa



Texture index 24.9828919

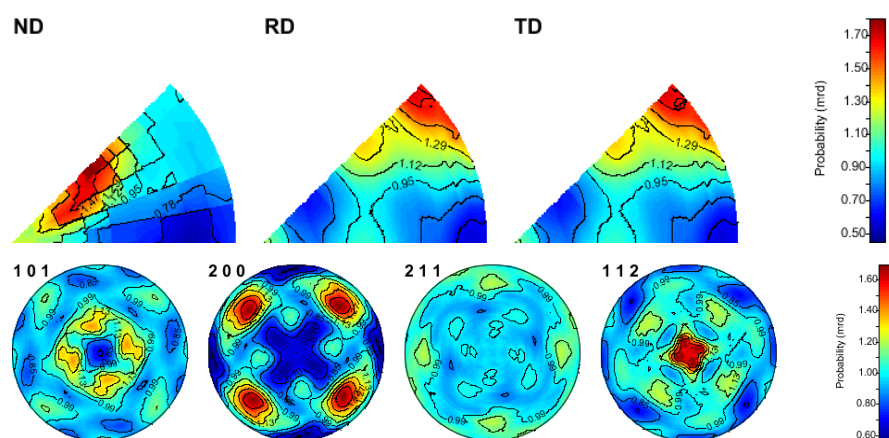
Zircon- 4-fold symmetry-10% Gaussian smooth ODF. *Normalized*

Reconstructed intensity. Pole figures intensity range:

-calculated: min=0.5623612615, max=1.701762226

Inverse pole figures. Range:

-calculated: min=0.44149882166, max= 1.8067672590



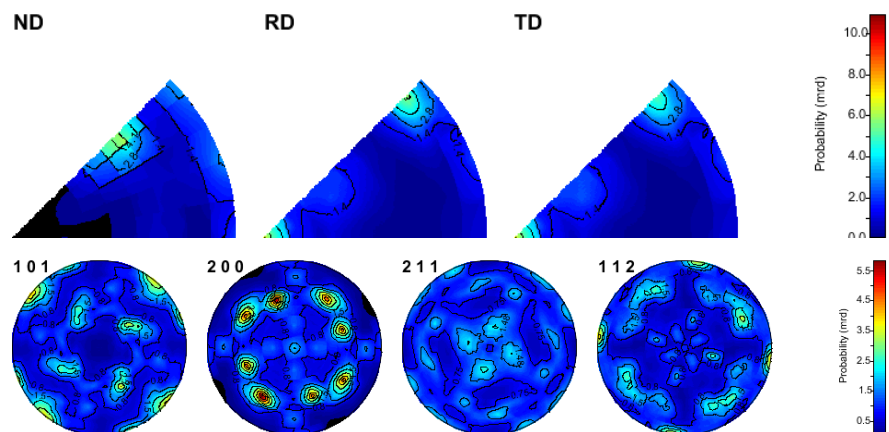
Zircon- 4-fold symmetry-10% Gaussian smooth ODF. *Not normalized.*

Reconstructed intensity. Pole figures intensity range:

-calculated: min= 0.024345701230, max= 5.86425054551

Inverse pole figures. Range:

-calculated: min= 0.003540058987, max= 11.0034514963



Appendix 3. Plots from EBSD.

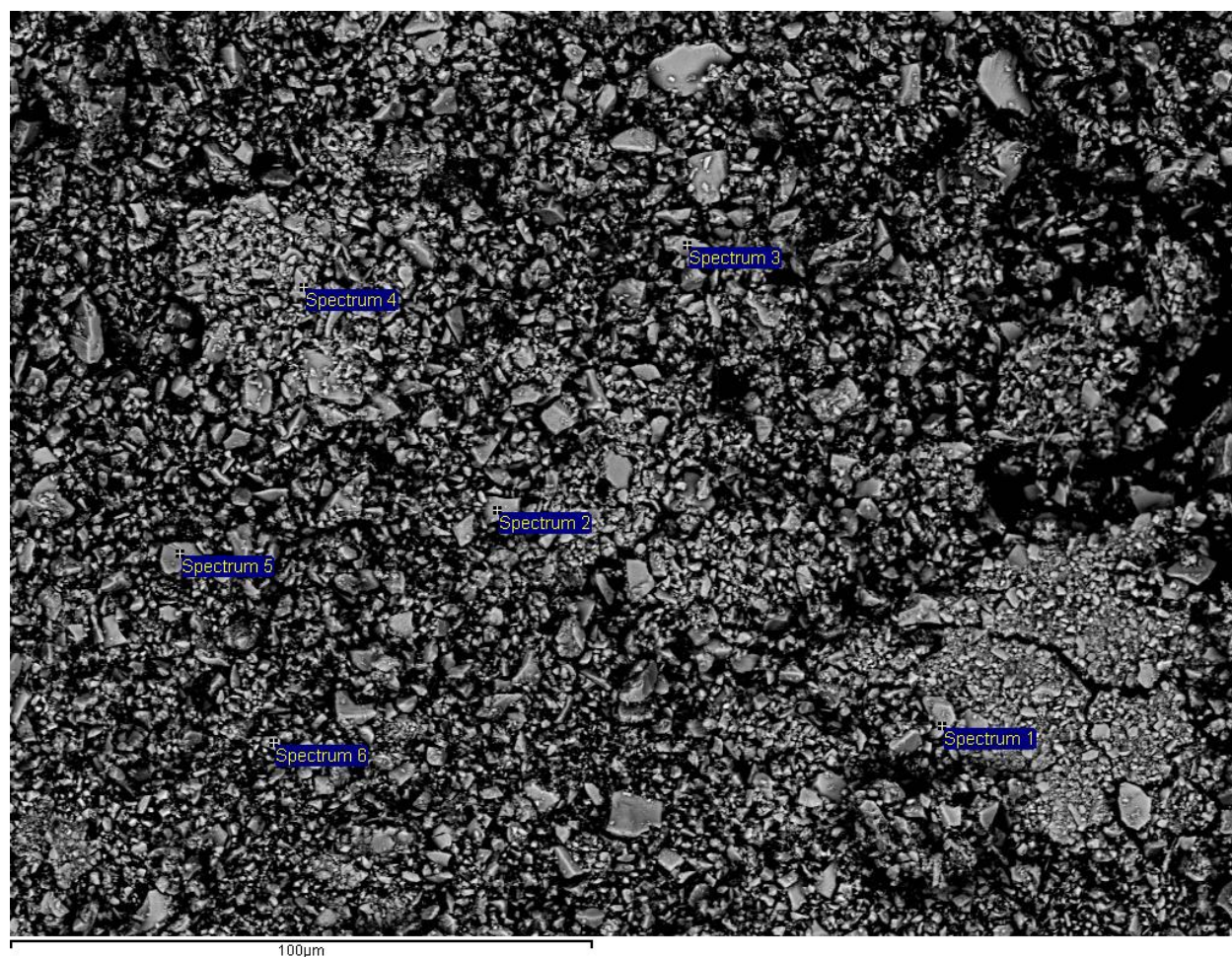
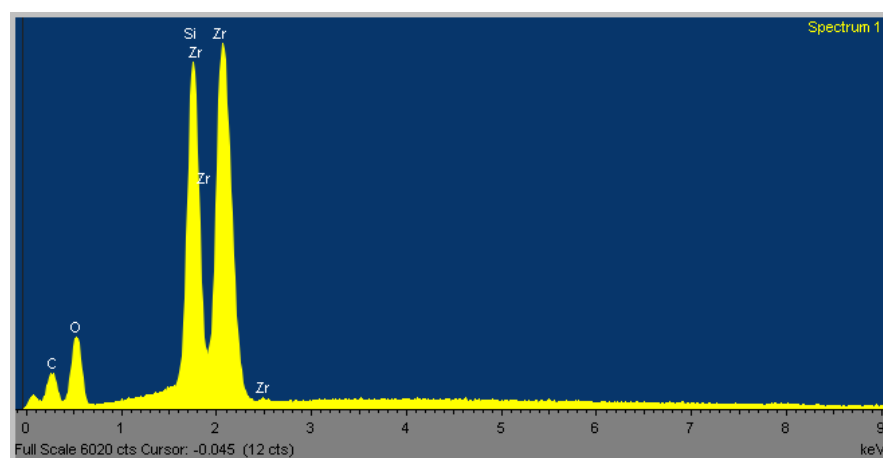
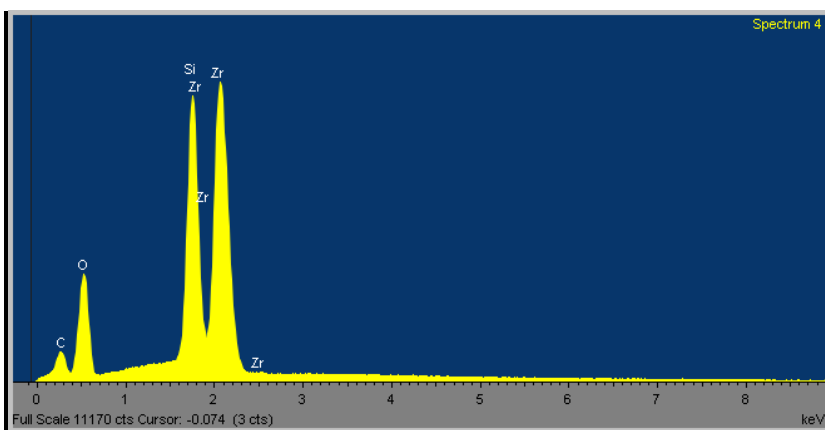
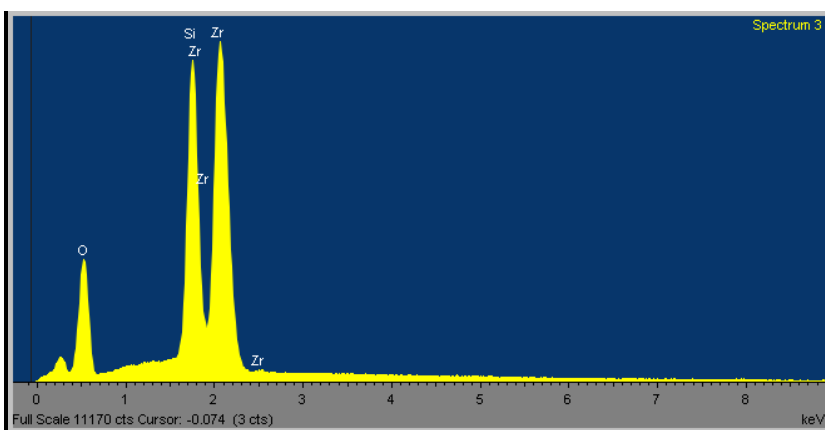
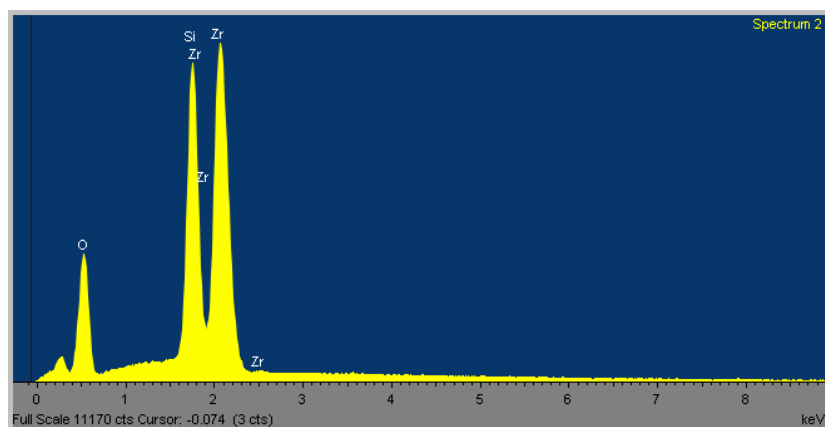


Figure A3.1. Electron image with marked collected spectra.





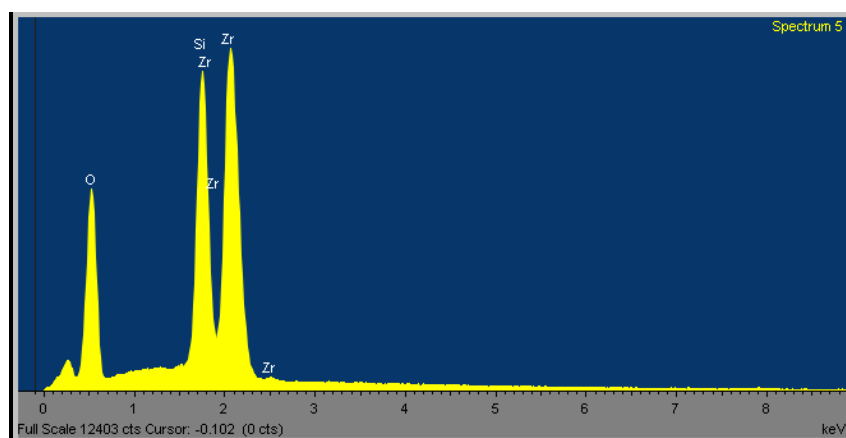


Figure A3.2 Collected spectra of zircon from powdered initial material (spectra 1-5).

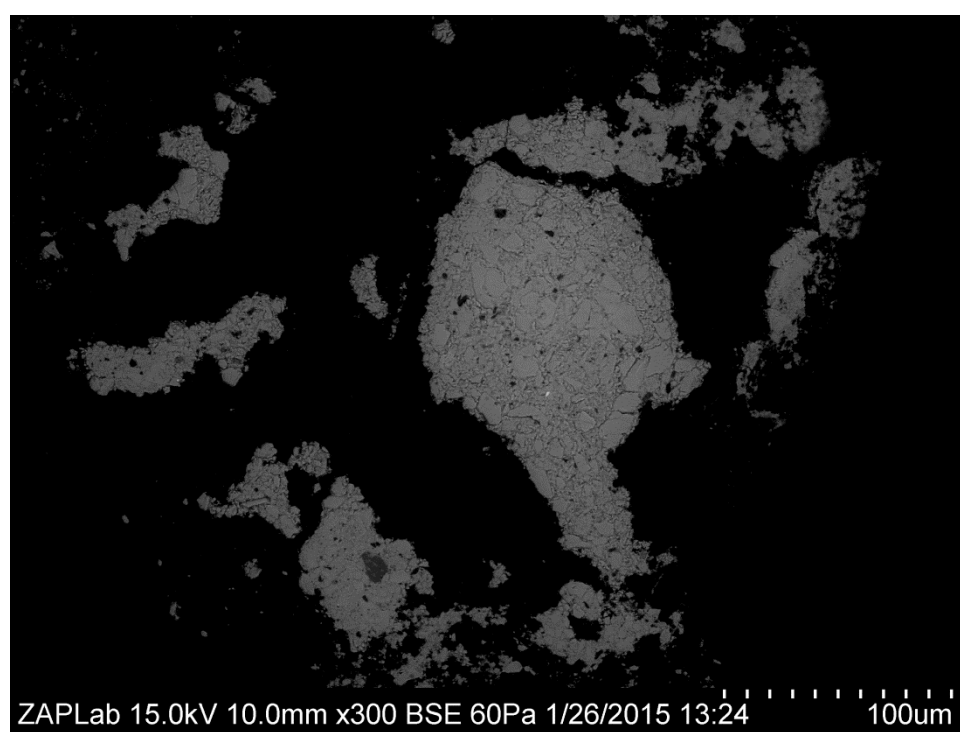


Figure A3.3 Sample 1, 500 microns. BSE image

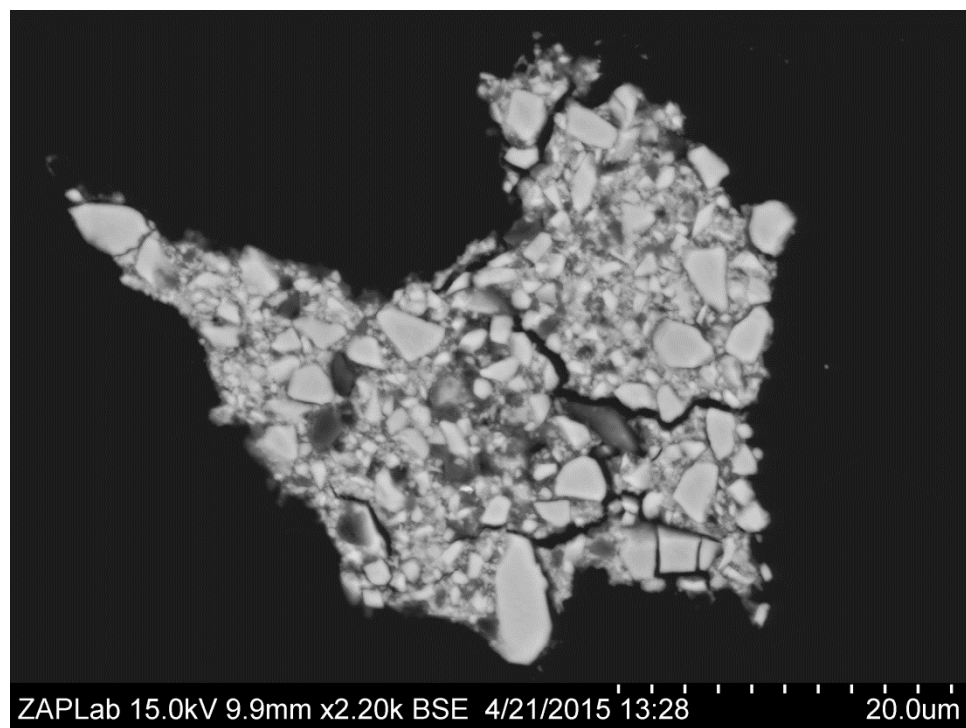


Figure A3.4 Sample 2, 300 microns. EBSD Area 4. BSE map

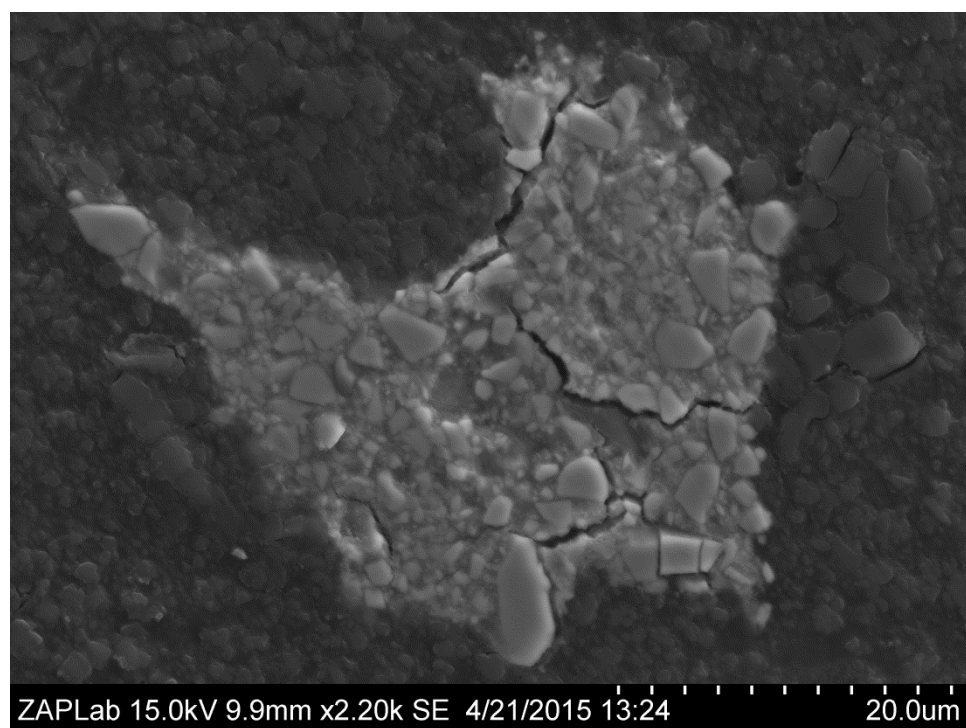


Figure A3.5 Sample 2, 300 microns. EBSD Area 4. SE map.

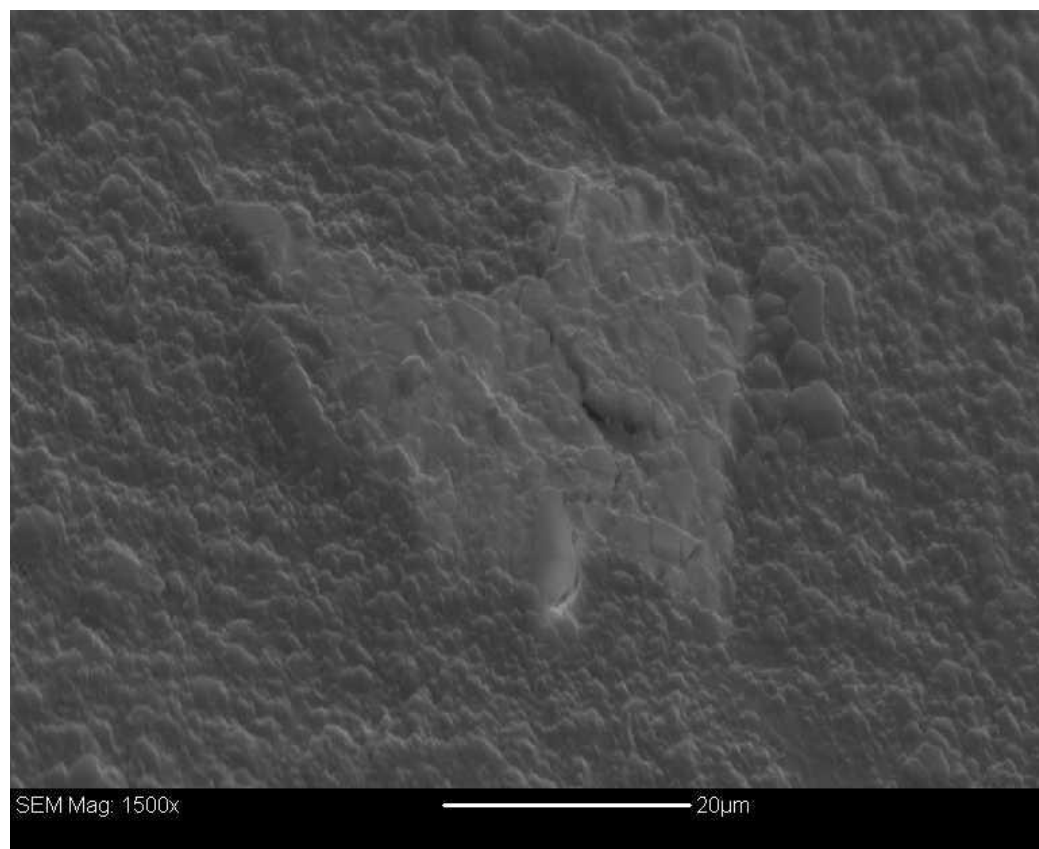


Figure A3.6 Area 4, before EBSD analysis.

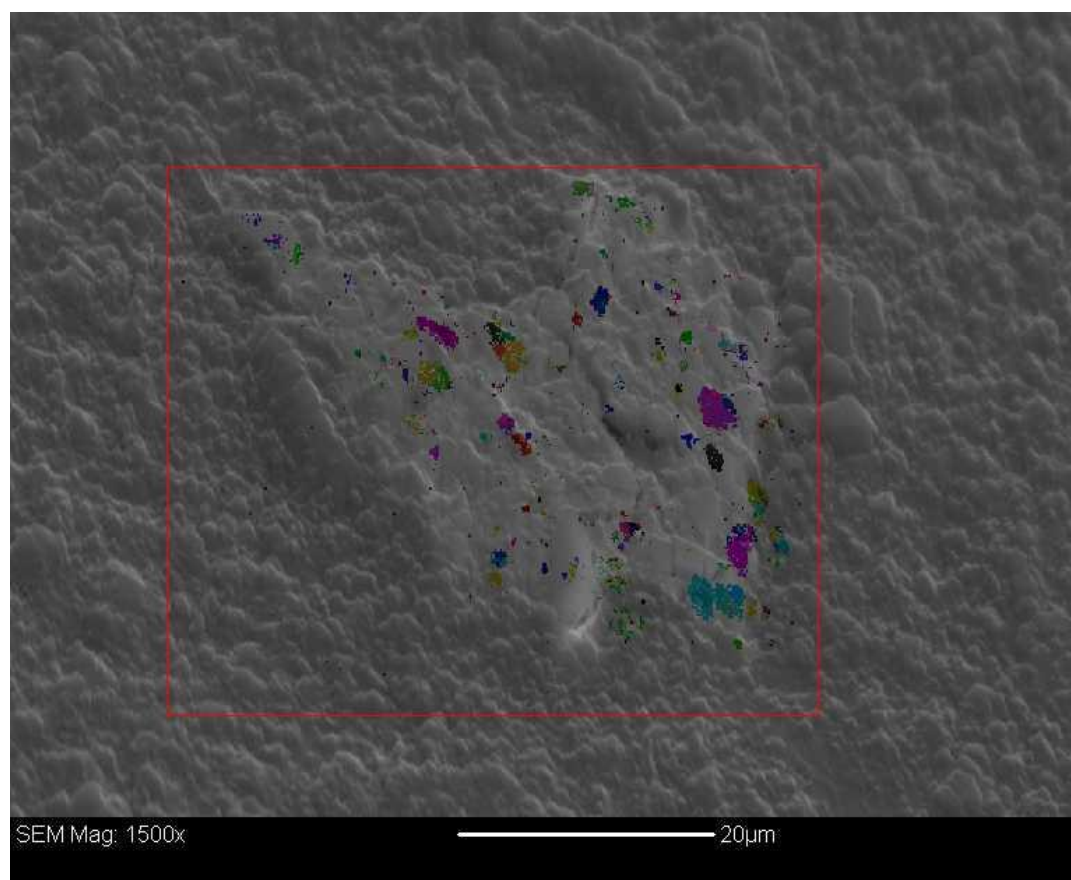


Figure A3.7 Area 4 with overlay.

CURRICULUM VITAE

Name: Ievgeniia Morozova

Post-secondary Education and Degrees: Kyiv National Taras Shevchenko University
Kyiv, Ukraine
2007-2011 B.Sc. in Geology
2011-2013 M.Sc. in Geochemistry and Mineralogy

The University of Western Ontario
London, Ontario, Canada
2013-2015 M.Sc. in Geophysics

Honours and Awards: **GRA Funding**, University of Western Ontario, London, Canada, *Sep 2013 – Aug 2015*

WGRS Scholarship, University of Western Ontario, London, Canada, *Sep 2013-Aug2015*

M. Sc. Fellowship, Kyiv National Taras Shevchenko University, Kyiv, Ukraine, *Sep 2011 - Jun 2013*

B.Sc. Fellowship, Kyiv National Taras Shevchenko University, Kyiv, Ukraine, *Sep 2007 - Jun 2011*

Related Work Experience Teaching Assistant, The University of Western Ontario
2013-2015

Publications:

- ♦ **Morozova I.**, Shieh, S.R., Moser, D., Hanchar, J.M. (2015) Deformation of Zircon Under High Pressure. *AGU-GAC-MAC-CGU Joint Assembly, Montreal, Canada*
- ♦ **Morozova I.**, Shieh, S.R., Moser, D. (2015) Strength of Zircon. *CAMBR Meeting*, Pub. Abstract/Poster
- ♦ **Morozova I.**, Shieh, S.R., Moser, D., Hanchar, J.M. (2014) Deformation Study of Zircon: A Strong Planetary Material. *Interdisciplinary Western University Showcase (poster)*, University of Western Ontario, London, ON, Canada